Second-Order Nonlinear Frequency Generation in Nanostructured Surfaces

Dissertation

zur Erlangung des akademischen Grades

doctor rerum naturalium (Dr. rer. nat.)

vorgelegt dem Rat der Physikalisch-Astronomischen Fakultät

der Friedrich-Schiller-Universität Jena

von M. Sc. Franz Johannes Friedrich Löchner

geboren am 20.03.1990 in Berlin-Köpenick

Gutachter

1. Prof. Dr. Thomas Pertsch, Friedrich-Schiller-Universität Jena
2. Prof. Dr. Thomas Zentgraf, Universität Paderborn
3. Prof. Dr. Giuseppe Leo, Université de Paris

Tag der Disputation: 26. Juli 2021

Contents

1. Introduction

Optics is a subject in physics investigating and explaining the behavior of light, but it is also a branch in technology urging for manipulation of light for many purposes which goes far back to the first greater civilizations thousands of years ago. It started with lenses and lead to a huge variety of optical elements nowadays, speeding up information technology and very recently introducing realization possibilities in the so-far theoretical quantum world.

Typical optical elements are bulky devices, which work on the premise of accumulating the phase of transmitted electro-magnetic waves in a certain way to change their propagation direction, their amplitude and their polarization. By decreasing the size of structures to a sub-wavelength scale, the phase of passing waves is changed on such a short distance that it can be interpreted as instant phase change. This is one essential change when going from optics to *nano-optics*.

A huge acknowledgement for advances in nano-optics has to be given to plasmonics. Plasmonic particles and later plasmonic nanoantennas paved the way towards nanostructures of any material with sometimes fascinating properties.

The relevant property, which is crucial for many effects and applications in nano-optics and thus for this work, is the ability to strongly enhance the local field. This can result in frequency dependent optical resonances, which can be used for spectral filters. The localization and thus concentration of field increases the light-matter interaction and can be used for example for sensing. With clever design, nano-particles and nanostructures can act as so-called nanoantennas controlling the energy transfer between a very localized spot, acting as receiver or emitter, and the radiating field[?] .

While metals, which are the essential material class for plasmonics, exhibit large inherent ohmic loss, dielectric materials such as semiconductors or oxides have wide transparent, i.e. lossless or at least low-loss, spectral windows reaching into the visible. These dielectrics used in nanostructures where able to achieve most of the effects known from plasmonics, but even feature new and very interesting properties. One of them are the multipolar characteristics of their resonances, i.e. plasmonic nanostructures are mostly governed by the electric dipole modes whereas dielectric nanostructures additionally exhibit strong higher order multipole Mie-type modes and especially the magnetic ones[? ? ?] .

Nano-particles or nano-antennas provide huge potential in light manipulation. Applications however, tend to need large-area action. Bridging this issue, the essential result are nanostructured surfaces, or so-called metasurfaces, often being periodic arrangements of nanostructures enabling arbitrary optical properties in a regime of sub-wavelength thickness over a large-area surface.

Metasurfaces have many possibilities to contribute in applications enabling beam deflection, beam focusing, generation of special beams like vortex or Bessel beams, manipulation of polarization, and - at least for special conditions - cloaking[? ? ?] .

Up to now, this motivation discussed only processes of the linear kind. However, at least since the development of lasers, it is known that the typically used linear models describing the world are rather approximations of generally nonlinear systems. These linear approximations are fine as long as the excitation is moderate. Due to their nature of photon-photon interactions, nonlinear responses are inherently weak. When, however, energetically dense laser beams come into play, at least in the realm of optics and photonics, these nonlinear responses are not only observable, but can play key roles in the outcome of these processes.

Essential processes in nonlinear optics are frequency conversions, e.g. second-harmonic generation (SHG) and third-harmonic generation (THG) as well as four-wave mixing, processes connected to the Kerr effect, e.g. self-modulation and self-focusing, as well as Brillouin scattering and spontaneous parametric down-conversion (SPDC)[?] , to name just a few. Applications range from lasers, over optical switches, modulators, and memories to photo-detectors. Frequency converters enable lasing in otherwise difficult to reach wavelength ranges such as Nd:YAG lasers[? ? ?] , they allow to generate ultra-violet light sources[? ? ?] , and they provide support in bioimaging[?] . Saturable absorbers help to generate ultrafast laser pulses[?] .

SHG as one of the lowest-order, i.e. second-order, nonlinear processes, was the first nonlinear optical process observed[?] . Its response is light emission at double the frequency or half the wavelength of the exciting electromagnetic wave, more details see Section 2.2. The process is well known for frequency doubling in laser sources as ND:YAG lasers or in optical parametric oscillators[?] . But it is also relevant for material characterizations, especially for crystal structure orientation and grain boundaries[? ? ? ? ? ? ? ?] . Another field of application is laser beam characterization[? ? ?] .

An essential drive for devices enabling second-order nonlinear processes is the possibility

to lead to quantum optical applications. A highly addressed goal there are quantum entangled photon sources. One way to achieve such entanglement is using the second-order nonlinear process of SPDC. By controlling second-order nonlinear wave-mixing processes like SHG, the somehow inverse process SPDC can be influenced by this knowledge, too.

In contrast to bulky nonlinear optical devices, exploiting nonlinear processes in nano-optics combines advantages of both worlds. Realizing frequency converters, saturable absorbers, et cetera in compact, light-weight systems enables the integration into otherwise possibly only linear optical and optoelectronic systems creating the opportunity of portable devices, for example for space applications. Thus, *nonlinear nano-optics* provides even more functionalities to an already application sparkling nano-world.

Employing resonances and thus localized field enhancement in nanoparticles and nanostructures is especially useful for nonlinear optics, since it can increase the typically low conversion efficiency of wave mixing processes like SHG. Adding the advantage of not being bound to phase-matching constraints due to the sub-wavelength sizes, the smaller interaction volume for the nonlinear processes might be outweighed. However, the damage-threshold in small and thin structures due to the high energy densities introduce a new challenge.

Especially nonlinear photonic metasurfaces satisfy the application needs as they provide new functionalities over large-areas. Accordingly, this topic experiences big efforts on investigations, including this work.

Due to the actual strength of the nonlinearity, fabrication challenges, and the spectral dispersion, the choice of nonlinear material for the nonlinear photonic metasurface plays a key role. Since third-order nonlinearity is bound to less symmetry restrictions, it is found in all materials. Correspondingly, the issue of material selection is mostly important for second-order nonlinear processes, which only crystal structures with broken inversion symmetry exhibit. Higher-order nonlinearities are investigated, but they do not play an important role in nonlinear metasurfaces yet. Essential materials for second-order nonlinearities are III-V semiconductors, e.g. (aluminum) gallium arsenid (AlGaAs, GaAs), due to their large values of second-order nonlinear susceptibility and already developed structuring technology. Perovskites like lithium niobate ($LiNbO_3$) on the other hand, often used in bulky nonlinear optical devices, lack easy and available structuring technologies although important advances have been made[? ? ? ?] . Very recently, also Zinc oxide was successfully used for nonlinear nanostructures[?] . Metals are found to have huge

second-order nonlinearities and thus are used in such nonlinear photonic metsurfaces[? ?], however their lossy nature and hardly negligible thermal heating diminish their applicability. A recently found material class providing second-order nonlinearity are transition metal dichalcogenide (TMD) mono- and other odd-numbered few-layers[? ? ?], which do play an important role in this work.

Note that next to material symmetry, also the symmetry of the exciting beam or the symmetry of the nanostructure arrangement can influence the ability to observe a second-harmonic (SH) response[? ? ?].

In terms of second-order nonlinear processes, next to plasmonics III-V semiconductor based nanostructures experienced the most advances in terms of second-order nonlinear nanostructures. GaAs and AlGaAs structures have been investigated due to their strong second-order nonlinearity, their high-refractive index and their already advanced structuring technology for (opto-) electronics. Nonlinear single nanostructure studies showed SHG[? ?], sum-frequency generation[?], and first nonlinear photonic metasurfaces were investigated observing SHG[?].

The main problem of the III-V semiconductor's second-order nonlinearity is the tensorial structure of their second-order nonlinear susceptibility, which does not allow for normal SH emission at normal excitation considering the typical (100)-cut surface.

Here, this work steps in with the respective publication connected to this thesis[?] observing SH diffraction in a GaAs metasurface similar to the one in[?] and thus for the first time actually being able to proof the SH emission out of the GaAs surface plane due to clever usage of the periodic arrangement and the multipolar Mie-type resonances. It even provided - for the first time - a hint of SH emission into the zero order diffraction which is theoretically forbidden (see Section 3.2.2), but might have occurred due to some artifact.

However, further studies showed much interest in this direction. One provided a set of many frequency mixing processes like SHG and sum frequency generation from one metasurface[?]. Another showed enhanced SHG by symmetry-broken metasurface unit-cells[?]. Very recent studies tried to overcome the vanishing zero order or normal to the surface SH emission of III-V semiconductors by changing the crystal cut and thus the crystal orientation at the surface[? ?] or by particularly combining the Mie-type resonances with diffraction in both excitation and SH[?].

Nevertheless, other second-order materials might be worth to investigate to achieve

normal SH emission with respect to the metasurface plane. Here, the recently discovered TMD monolayers come in handy.

After the discovery of graphene as a two-dimensional monolayer made of carbon, similarly the semiconducting TMD monolayers have been found by exfoliation from bulk TMDs, with much better optical usability than graphene due to their direct band gap[?] . Fascinatingly, the direct band gap offers the possibility of atomically thin light emitting diodes[? ? ? ?] . Their tight dimension increases the role of excitons in comparison with bulk semiconductors like GaAs, leading to strong exciton-governed photoluminescence (PL)[? ?] .

Next to the low-yield technique of exfoliation, these TMD monolayers can be grown by chemical vapor deposition (CVD), which enables large-area monolayers. The growth process recently found its way to be reproducibly of high-quality and homogeneity[?] which makes it a promising material for applications.

A typical goal for new materials is reliability and reproducablity of the material in terms of quality and property. Here, this thesis does play a relevant role as being one of the first applications using these high-quality CVD-grown molybdenum disulfide (MoS_2) monolayer crystals which infact prove to be very homogeneous and comparable in their properties as can be seen in the later reports of experiments in Chapters 6 and 7.

TMD monolayers can be transferred from their growth substrate on almost any target by different methods[? ? ? ?] . Accordingly, high expectations on special properties are put on hetero-structures of TMD monolayers, i.e. a combination of different TMD monolayers mostly realized by stacking found already in early reviews[? ?] .

However, in respect to nonlinear optics, the remarkable property of TMD monolayers is a second-order nonlinearity, which turns off for even-numbered fewlayers and turns on for odd-numbered fewlayers like the monolayer itself[?] . Its second-order nonlinear susceptibility offers strong components with respect to the ultrathin interaction volume of less than 1 nm thickness, containing elements which do enable SH emission normal to their two-dimensional plane (see Section 3.1.2).

SHG from MoS_2 monolayers was observed first[? ?] , followed by monolayers of tungsten disulfide (WS_2)[?] , tungsten diselenide (WSe_2)[? ?] and molybdenum diselenide ($MoSe_2$)[?] . Many studies on the nonlinear properties of these TMD monolayers followed including THG[? ? ? ?] , high-harmonic generation[?] , four-wave mixing[? ?] , and saturable absorption[? ?] .

Interestingly, it is possible to excite a WS_2 monolayer, and thus in general a TMD monolayer, with a vortex beam and observe a vortex beam in the SHG[?] .

Heterostructures also have been investigated in terms of nonlinear optics, showing SHG dependence on the relative orientation of stacked bilayers[?] , sum frequency generation[?] and saturable absorption[?] , to name just a few.

However competitive this scientific race was and still is, two gaps which were still unsatisfactorily well investigated could be filled by this work and its respective publications in order to develop second-order nonlinear metasurfaces some steps further.

While by transfer the monolayer itself already adds a new functionality, whether PL or second-order nonlinearity, to any surface, to manipulate this feature by structuring the monolayer itself is not a wide-fetched idea although a tough challenge. The issue on locally removing parts of the monolayer by lithographic means did show some success[? ?] , however the etching process can create serious problems for the remainders of the TMD layers. The direct writing by focused ion beam (FIB) milling proved to be a better choice as it was used in few layers of MoS_2[? ?] .

This work together with the concurrent work of Dasgupta *et al* for the first time showed successful patterning of MoS_2 and WS_2 monolayers, respectively, by FIB milling[? ?] . While this work showed detailed analysis on SH diffraction from periodic one-dimensional gratings written into the monolayer, both works were able to observe SH vortex beams by linearly polarized Gaussian beam excitation in fork-like grating structures. Accordingly, nonlinear beam shaping is possible by structuring these ultrathin materials.

However appealing and successful the patterning approach seems, the SH signal is rather weak due to the ultrathin interaction volume, which is even reduced by the structuring process. To enhance the SHG, resonant field enhancement would be key. Unfortunately, these monolayers cannot confine light like other nanostructures due to the ultrathin interaction volume. The solution here is to hybridize the monolayers with otherwise not nonlinear photonic structures. This approach exploits the local field enhancement of the photonic structure adding the nonlinearity by the TMD monolayer.

Respective hybrid systems proved very successful for exciton and PL investigations[? ? ? ? ? ? ? ? ?] . For SHG, investigated systems did show high enhancement when the TMD monolayers were put on grooves written into metal thin films by FIB techniques[? ?] . However, these platforms are not easily scalable, since the fabrication technique is not a fast technology for large area structuring. Another platform are cavities with Bragg mirrors where the TMD monolayer is inserted. Strong SH enhancement was observed in the case of actively

controlled phase matching[?] , which is a technologically rather complicated scenario and thus typically limited to small areas. Some moderate enhancement resulted from TMD monolayers connected to dielectric waveguides[?] and to single SiO_2 microspheres[?] . Very recently it was shown that guiding surface waves from a periodically stacked thin-film structure can lead to very efficient SHG and sum-frequency generation[?] .

A very promising platform is using Si metasurfaces with its highly developed structuring technologies and the resonance design has already been proven to be very sophisticated[? ? ?] . In this work's approach, which has been published by this work's author and collaborators[?] , spectrally narrow resonances, i.e. strong field enhancement, were achieved by asymmetric double bar unit cells, which have already proven to be useful in other systems[? ?] . Covering these Si metasurfaces by CVD-grown MoS_2 monolayers not only shows the highest SH enhancement so far in a large-area and scalable hybrid system, in this work it also reveals important guidelines on how the field distribution of the linear resonance has to be to efficiently generate SH.

In contrast to this work, a very similar system with an asymmetric Si double bar covered by exfoliated WS_2 monolayers[?] lacks scalability due to the use of exfoliation and it does neither fairly compare its SH enhancement nor properly investigate its whereabouts.

To wrap up this introduction, three important studies in the field of SHG from nonlinear nanostructured surfaces have been conducted in this work. All three add impact to the development of second-order nonlinear metasurfaces.

First, an intrinsically nonlinear photonic metasurface made from the established second-order nonlinear material GaAs was investigated. SH diffraction was observed including the proof for SH emission out of the metasurface plane. Since the SH emission normal to the metasurface plane at normal excitation is rather difficult to achieve, a different approach had to be taken.

In the second study, newly available second-order nonlinear TMD monolayers were investigated to realize functionalized nonlinear metasurfaces. For the first time (simultaneously with[?]) TMD monolayer were patterned with high resolution by FIB milling and SH diffraction was observed and analyzed. It was possible to generate nonlinear holograms, in particular SH vortex beams.

Third, to enhance the SH emission from TMD monolayers and thus to improve the practicability of using this material for second-order nonlinear metasurfaces, a hybrid system consisting of a multi-resonant Si metasurface covered by MoS_2 monolayers was

investigated, observing not only SH enhancement, but additionally finding guidelines to make best use of resonances with field enhancement overlapping with suspended parts of the monolayer.

Introducing some major basic physical ideas which play an important role in this work, Chapter 2 describes *optical resonances* in nanostructures such as Mie-type resonances, it explains shortly the *nonlinear process* of SHG in terms of the second-order nonlinear susceptibility, and it familiarizes with *diffraction* in periodically arranged structures including the combination with SHG leading to SH diffraction.

Chapter 3 presents the two second-order nonlinear materials used in this work, namely the recently discovered two-dimensional MoS_2 *monolayer* and the highly investigated and developed III-V semiconductor *GaAs*.

The ability to measure SHG with its challenges and constraints requires a special setup. The here developed and used self-built *SH microscope* is described in Chapter 4 including an often forgotten issue of *polarization ellipticity* and the observation of the angular emission spectrum via *back-focal plane imaging*.

Starting the last three chapters about the investigated nonlinear nanostructured surfaces, Chapter 5 deals with the *GaAs metasurface* observing SH diffraction, discussing the SH emission out of the surface plane.

Moving away from the III-V semiconductor toward the newly found two-dimensional MoS_2 monolayers, SH diffraction including the generation of SH vortex beams excited by a linearly polarized FH Gaussian beam from *patterned* MoS_2 *monolayers* is described in Chapter 6.

Finally, Chapter 7 features a hybridized nonlinear metasurface coupling a multi-resonant Silicon metasurface without seond-order nonlinearity to a second-order nonlinear MoS_2 monolayer to find important guidelines for the successful use of such hybrid systems, exemplarily searching for SH enhancement.

A short outlook after a conclusion of the experiments is terminating this work in the last Chapter 8.

2. Basic concepts

2.1. Resonances in structured media

2.1.1. Electromagnetic fields and media

To describe light interacting with structured surfaces of matter, a physical-mathematical foundation is required. The description will be short, but nevertheless comprehensive to support the explanations and interpretations of the data reported in the later chapters. In the first section, the material polarization as the main quantity to describe light-matter interaction will be introduced, then Mie-type resonances in dielectric nanostructures are discussed, to be followed by the collective effects in ensembles of nanostructures. The second section provides insights into the second-order nonlinear process called second-harmonic generation which is the main optical process reported in this thesis. How light is diffracted in periodic arrangements of structures is dealt with in the final third section, including the lesser known term second-harmonic diffraction.

For all these topics, light is best described by the model of electromagnetic waves. Nevertheless, across this thesis, the particle model will also be used to specify and understand processes connected to specific material properties. Especially phenomena like absorption, excitation and recombination are found to be intuitively easier understood by the interaction of particles like photons for light as well as electrons and holes for the here mainly used semiconducting materials.

The dynamics of light described by electromagnetic waves is governed by Maxwell's equations.

The interaction of light with a material depends on how the electromagnetic wave forces the shell electrons of the material's atoms to move and build up dipoles. In a material, way too many of these atoms and electrons build a system which cannot be dealt with individually, but can be described to act as a whole. This simplifies the description in the wave formulation since only averaged properties which can be associated with mathematical terms can be used. Correspondingly the so-called macroscopic Maxwell's equations are formed[?] .

The important quantity in the macroscopic Maxwell's Equations describing the collection of dipoles set in the material by the initial electromagnetic field $\vec{E}$ is the dielectric polarization, or as it is referred to in this work: the material polarization $\vec{P}$. It can

be seen as an oscillation of the charges in the medium. It has to be distinguished with the polarization property of the electric field itself, which is its vectorial direction of the oscillation.

The material polarization acts as a source for a new electromagnetic field due to the movement of the material's charges. The initial and the induced electric fields interfere and thus the medium is changing the overall electric field. The same is true for the magnetic field and the so-called magnetization $\vec{M}$, although most materials have only a very small interaction in the magnetic regime. Thus, in this work, we are concentrating on the electric field to describe the investigated light-matter interactions.

Generally, the material polarization $\vec{P}$ can be expressed as a series of material polarizations of different orders (n), meaning an increasing dependence on the electric field $\vec{E}$ to the power of n, as described in *Nonlinear Optics* by Boyd[?] ,

$$\vec{P} = \vec{P}^{(1)} + \vec{P}^{(2)} + \vec{P}^{(3)} + ... \ . \tag{2.1}$$

While the first series element $\vec{P}^{(1)}$ describes the linear relation between the material polarization and the electric field, the other elements describe the so-called nonlinear polarization $\vec{P}^{NL} = \vec{P}^{(2)} + \vec{P}^{(3)} + ... \ .$ The latter are typically small enough to be negligible, but at strong fields they can become relevant. This will be described in more detail in the Section 2.2 about nonlinear optics.

Many optical processes can be approximated by the well known linear relation

$$\vec{P}^{(1)}(\omega) = \epsilon_0 \hat{\chi}^{(1)}(\omega)\vec{E}(\omega) \ , \tag{2.2}$$

where ϵ_0 is the vacuum permittivity and ω is the frequency at which the electric field and the linear material polarization oscillate. The material property included here is the so-called susceptibility $\hat{\chi}^{(1)}$, a first-rank tensor. The crystal structure of the material with its symmetries reflects on the tensorial structure of $\hat{\chi}^{(1)}$. Often the material property $\hat{\epsilon}_r^{(1)}$ as the relative permittivity is used to describe a medium, which correlates with the susceptibility as $\hat{\epsilon}_r^{(1)} = \hat{\chi}^{(1)} + \mathbb{1}$, where $\mathbb{1}$ is the unity matrix.

Note that Eq. 2.2 holds true in the frequency domain. A quantity $f(\vec{r}, t)$ in the time domain is transformed to its respective quantity $f(\vec{r}, \omega)$ in the frequency domain and vice versa via forward and backward Fourier transform

$$\begin{aligned} f(\vec{r}, \omega) &= \frac{1}{\sqrt{2\pi}} \int_{-\infty}^{\infty} f(\vec{r}, t) e^{-i\omega t} dt \\ f(\vec{r}, t) &= \frac{1}{\sqrt{2\pi}} \int_{-\infty}^{\infty} f(\vec{r}, \omega) e^{i\omega t} d\omega \ . \end{aligned} \tag{2.3}$$

Via this transformation also Maxwell's equations and associated equations and relations

can be transformed between both domains giving the opportunity to describe several aspects of electromagnetism from different perspectives. Detailed information can be found in the book *Classical Electrodynamics* by Jackson[?] .

A possible solution to Maxwell's equations in homogeneous media is the plane wave which mathematically can be described by

$$\vec{E}(\vec{r},t) = \vec{E}_0 \exp(i\vec{k}\vec{r} - \omega t) \ , \tag{2.4}$$

where $\vec{k}$ is the wave vector describing the propagation direction and ω the frequency of the oscillation. With $\vec{E}_0$ three important properties of the plane wave oscillation are introduced: the amplitude by the absolute value $|\vec{E}_0|$, the initial phase, and the direction due to the vector which is the polarization of the field itself. In the case of linear optics, the sum of plane waves, also called the superposition, is also a solution of Maxwell's equations.

For further reference, the so-called TE- and TM-polarization are defined for a plane wave, or a linearly polarized superposition of plane waves, hitting a plane interface. The plane of incidence is spanned over the wave vector $\vec{k}$ of the plane wave and the normal vector on the interface plane. Both TE- and TM-polarization are orthogonal to each other and perpendicular to the wave vector $\vec{k}$. TE-polarization stands for transverse-electric and associates to the direction perpendicular to the plane of incidence, also called s-polarization, while TM stands for transverse magnetic and associates with the direction in the plane of incidence, also called p-polarization.

Plane waves carry a phase ϕ, which is the argument of the exponential function $i\vec{k}\vec{r} - \omega t = i\phi$ in Equation 2.4. ϕ is varying over time t and space $\vec{r}$. Its value is the critical condition for interference of light and thus relevant for the next subsections discussing confinement of light, it has an effect on second-harmonic generation over long distances or in large volumes as described in Section 2.2, and it is important for diffraction as dealt with in Section 2.3.

2.1.2. Optical resonances in nanostructures

A resonance occurs when a system is excited by a frequency ω and its response shows an amplitude maximum of the oscillation with respect to frequencies around ω[?] . In optical systems, the excitation is an electromagnetic field at frequency ω. The reason for the stronger response usually comes from light confinement due to geometrical boundaries of a medium creating a cavity.

A simple and well-known example is the Fabry-Pérot resonator describing two plane,

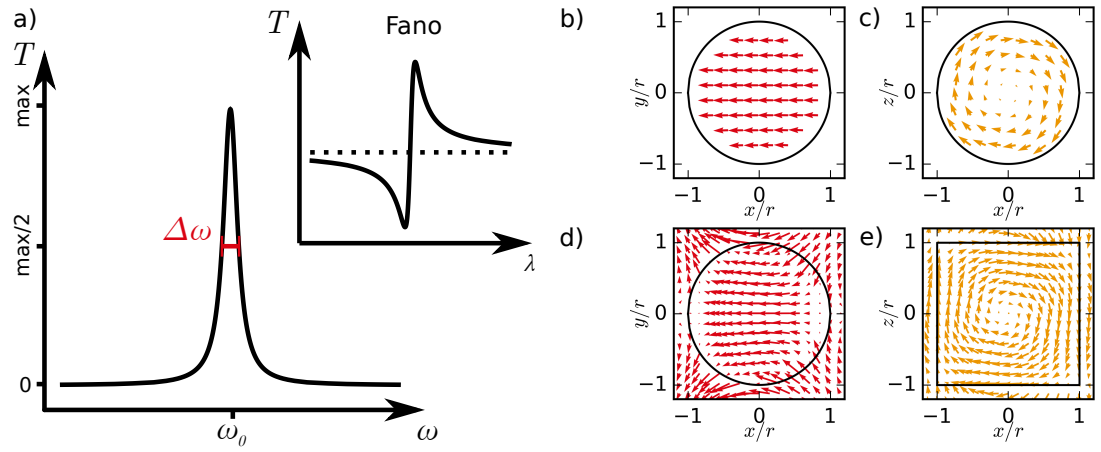

Figure 2.1.: a) Sketch of a resonance in a transmission (T) spectrum depicting the central wavelength ω_0 and the full width at half maximum $\Delta\omega$. The inset shows the asymmetric lineshape of a Fano resonance. (b) and (c) show the vector plots of the analytically calculated internal electric fields of the electric dipole and the magnetic dipole in a sphere, respectively. (d) and (e) show the vector plots of the numerically simulated electric fields of a disc with radius $r = 160$ nm, 320 nm height and relative permittivity of $\epsilon_r = 10.24$ surrounded by air at $\lambda = 950$ nm (d), where it is mainly dominated by the Mie-type electric dipole, and at $\lambda = 1200$ nm (e), where it is mainly dominated by the Mie-type magnetic dipole, respectively. The numerical simulations are performed with the finite element solver from JCMwave[?] .

parallel and reflecting interfaces, e.g. a glass slide, excited by plane waves. When the phase collected on the optical path between the interfaces and from the reflection matches, light can accumulate inside the resonator due to constructive interference, exhibiting a field enhancement. For these frequencies, which fulfill the phase matching, a stronger transmission occurs[?] .

In Fig. 2.1(a), a spectrum, i.e. the frequency dependence of a physical quantity, of a system with resonantly enhanced transmission is shown. The resonance is the peak around the central frequency ω_0. A resonance typically has a certain broadness which can be described by the full width at half maximum (FWHM), shown in the figure as $\Delta\omega$. Depending on the optical process in the resonator and the investigated quantity, a resonance can be a peak or a dip in the spectrum.

To characterize a resonance, the quality factor or short Q-factor of an optical resonance is introduced. It is defined as the energy trapped or stored in the system per loss in the system due to absorption and energy leaving the system by radiation. This definition can be paraphrased by many different concepts. In a cavity, the Q-factor describes how many round-trips - in average - the light travels between the mirrors until it can leave the system or until it is absorbed.

In a spectral analysis of resonances, the Q-factor can be easily determined by the

following equation:

$$Q = \frac{\omega_0}{\Delta\omega} \approx \frac{\lambda_0}{\Delta\lambda} \,, \tag{2.5}$$

where ω_0 and λ_0 are the central frequency and wavelength of the resonance, while $\Delta\omega$ and $\Delta\lambda$ describe the respective FWHM of the resonance. Accordingly, a higher Q-factor is equivalent to a more narrow resonance peak/valley.

The higher the Q-factor, the more light, i.e. energy, is trapped or stored in the system, which means the field enhancement is larger. Depending on the system, this field enhancement can be further localized at a special position inside the resonator.

Nanostructures working as antennas or resonators manipulate the forward and backward scattering of light[?] . Their typically two- or three-dimensional cavity geometry introduces more degrees of confinement conditions than the earlier mentioned one-dimensional Fabry-Pérot resonator. Special field distributions can be supported due to particular modes which increase the usability in applications. One of these applications is biosensing[? ?] where for example spontaneous emission rates of single molecules might increase due to nanoantennas.

Here, nanostructures of dielectric materials are discussed which provide many possibilities to manipulate the light[? ?] . An essential tool to characterize the optical behavior of dielectric nanostructures is Mie theory. In this section, it is aimed for a short description and interpretation of the solutions, leaving the mathematical description to books like *Absorption and Scattering of Light by Small Particles* by Bohren and Huffman[?] .

Gustav Mie developed a theory on electromagnetic scattering on spheres[?] . There is an exact analytical solution when the spherical particle is excited by a plane wave. The essential features of the solution are vector spherical harmonics, specifically magnetic harmonics $\vec{M}^{o}_{emn}$ and electric harmonics $\vec{N}^{o}_{emn}$. They consist of associated Legendre polynomials and spherical Bessel functions. Then, the incident plane wave as well as the scattered and internal field of the sphere can be expanded into series of these vector spherical harmonics. The respective coefficients describe how much of each harmonic takes part for the investigated sphere radius at the incident plane wave frequency.

Electric dipoles are represented by the harmonic $\vec{N}^{o}_{em1}$, while magnetic dipoles correspond to $\vec{M}^{o}_{em1}$. Respective electric and magnetic quadrupoles are connected to $\vec{N}^{o}_{em2}$ and $\vec{M}^{o}_{em2}$. Octopols and higher orders come with increasing index n. The small index m relates to the orientation depending on the propagation direction and polarization of the incident field, having the possibility to take numbers from 0 to n. The indices e and

o stand for *even* and *odd*.

The analytically calculated internal electric fields corresponding to the different harmonics in the sphere are shown in Figs. 2.1(b) and (c) for the electric and magnetic dipole, respectively. The plots show vectors representing the direction of (E_x, E_y) and (E_x, E_z), respectively. This highlights the dipole behavior of the electric field for the electric dipole and the circling electric field for the magnetic dipole.

At large distances from the sphere, the radiation pattern is governed by that of the angular part of vector spherical harmonics[?] , i.e. dipole radiation, quadrupole radiation and so forth. The excitation of a sphere typically does not lead to an electromagnetic field solely determined by one single spherical harmonic, but to a mix of harmonics with different weighing. The respective radiation pattern might be dominated by one harmonic, e.g. the dipole, the combination however can lead to special radiation cases[?] .

Especially, the work of Kerker *et al.*[?] on a vanishing backward scattering by interference of the electric and magnetic dipole modes, influenced investigations on different combinations of multipoles to manipulate the radiation direction of nanostructures[? ? ? ? ? ? ? ? ? ?] . For example, it is possible to achieve unidirectional radiation perpendicular to the propagation direction of the exciting wave by the interference of in-plane electric dipole and electric quadrupole together with an out-of plane magnetic dipole[?] .

Usually, nanostructures fabricated in a top-down method like lithography sit on their substrate and thus have no spheric shape. They rather are discs, bars, rods, prisms et cetera. Finding the eigenstates of these geometries is usually not analytically possible as in spheres. However, the similarity of the actual eigenstates - found by numerical simulations - to the harmonics from Mie modes established the so-called multipole analysis in which the field distribution in such structures is described as a series of Mie modes. Resonant states of the light field in these structures are often called Mie-type resonances.

The numerically simulated electric fields in a disc of radius $r = 160$ nm, height $h = 320$ nm and relative permittivity $\epsilon_r = 10.24$ surrounded by air excited by a plane wave, are shown in Figs. 2.1(d) and (e) for the wavelengths 950 nm and 1200 nm, respectively. The plots show vectors representing the direction of (E_x, E_y) and (E_x, E_z), respectively. Fig. (d) shows a field dominated by the electric dipole, while in Fig. (e) the magnetic dipole dominates, as is easily comparable to Figs. (b) and (c) with the analytical analogs in a sphere. The numerical simulations were performed via the finite element method solver from JCMwave[? ?] .

Mie-type resonances become very prominent in high-index low-loss dielectric structures

like Si or GaAs discs. An example for the latter is reported in Chapter 5. The expansion of the field distribution into Mie modes helps explaining radiation characteristics which relate on the propagation properties of the actual Mie modes.

Mie-type resonances are typically confining light inside the higher index material and have a broad spectral response. Thus they do not provide a strong field enhancement which corresponds to a low Q-factor. In ensembles, however, dielectric nanostructures can possess sharp resonances providing strong local field enhancement. Respective collective effects will be discussed in the next subsection.

2.1.3. Collective effects in metasurfaces

With respect to applications, the impact of single nanostructures is rather limited due to the very small interaction volume or area. Ensembles of nanostructures can overcome this issue and even provide new features. Already a dimer, i.e. two nanostructures in close vicinity, made from dielectric materials can provide a strong field confinement in the gap[? ? ? ?] . The essential feature of these ensembles is the influence additional nanostructures have on the field induced in one nanostructure during optical excitation. New energetically preferable modes can develope and be excited, leading to new resonances.

A special case of such ensembles, are large area arrays of nanostructures that typically are periodic arrangements, creating a nanostructured surface. Any surface consisting of structures of sub-wavelength dimensions and being localized between two media, for example air and the substrate material, abruptly alters the optical properties at this interface. These surfaces are called metasurfaces[?] . If designed properly, they can have different functionalities like large area field enhancement, phase delay, directional scattering, and spectral filter abilities. The investigations on such metasurfaces increased when the technology for nanostructuring, mainly lithographic methods, became faster, more precise and especially more available.

In periodic arrays, whether one- or two-dimensional, the scattering can be enhanced by two collective effects, Rayleigh anomalies and optically guided modes[?] .

Around 1900, Rayleigh first explained parts of Woods findings on the so-called Rayleigh anomalies[? ? ?] , why they are sometimes also called (Rayleigh-) Wood anomalies. They originally describe abruptly appearing features in the spectra of metallic gratings leading to the discovery of surface plasmon polaritons. In the last two decades periodic arrangements, i.e. gratings, of dielectric structures are strongly entering the optical research community, where similar effects could be found[? ? ?] .

The effect stems from grazing diffraction orders, i.e. when the propagation angle of the diffraction order just transits from the plane of the grating toward propagation away from the grating. From a Fano-type coupling effect combining the narrow states of Rayleigh anomalies and the broad resonances from the nanostructures, so-called surface lattice resonances (SLR) emerge[?] . They are especially dependent on the period of the grating.

The other collective effect arises from Rayleigh anomalies coupling to optically guided modes as in a waveguide close to the periodic array, i.e. a grating. The latter can introduce loss into the guided mode, which becomes a leaky mode, also called quasi-guided mode (QGM), i.e. it has still a long enough decay length to be considered propagating. However, depending on the period and the resonances of the grating, the QGM can, if the structures are well designed, create strong radiative resonances. Such effects were investigated for example in systems of a thin guiding dielectric layer close to plasmonic nanostructures[? ? ?] .

The difference of the two regimes is the condition, that QGM needs a high-refractive index waveguide close to the nanostructure array while the SLR needs a homogeneous dielectric[?] .

The coupling of the Rayleigh anomalies to resonances, whether Mie-type resonances or to QGMs is connected to a coupling scheme described by Fano[? ? ?] . Fano-type resonances appear by coupling a sharp resonant feature with a broad background resonance to receive a high-Q, asymmetric line shape in the spectrum as shown in the inset in Fig. 2.1. A project using a Fano-type resonance is presented in Chapter 7. The high field enhancement resulting from this resonance is used as excitation for second-harmonic generation in an adjacent nonlinear medium. How this nonlinear process works in general is described in the next section.

2.2. Nonlinear optical processes

2.2.1. General remarks

The main physical process dealt with in this thesis is second-harmonic generation (SHG), which is a nonlinear process. Thus in this section, nonlinear optics is introduced and described. Hereby the focus is set on the second-order nonlinearity of materials which enables SHG. The formalism and explanation mainly bases on the book *Nonlinear Optics* by Robert Boyd[?] .

Physics describes systems and processes by mathematical models to understand and then predict their behaviors. Many processes can be well described by simple linear models, some need more complicated or even nonlinear models. Nonlinear means, that the dependence of one quantity on another one is not linear, but nonlinear for example by the power of two or three.

In optics, linear and nonlinear effects are distinguished by the dependence on the electromagnetic field. Many optical processes like reflection, transmission, interference and photoluminescence are well described by models of linear dependence on the initial field. Some processes, however, cannot uphold these simple models. Their important quantities depend nonlinearly on the electromagnetic field.

Considering the material polarization of Eq. 2.1, the first term $\vec{P}^{(1)}$ depends linearly on the electric field $\vec{E}$, while the other terms depend on products of the electric field. This sum of polarizations can be seen as a series expansion, where the nonlinear terms are correction terms to the first, linear term. The influence of the higher-order terms is typically small due to small coefficients accompanying them, as in a Taylor series.

However, due to the invention of lasers which provide strong and coherent light beams, the products of the electric fields become very large and thus the influence of the nonlinear polarization terms cannot be neglected anymore.

Examples for nonlinear processes are frequency conversions and mixing processes like second- and third-harmonic generation, sum-frequency generation, four-wave mixing and optical rectification. Another group of nonlinear processes is connected to the Kerr effect like self-phase modulation and self-focusing. Other examples are stimulated Brillouin scattering, Raman amplification, multi-photon absorption and spontaneous parametric down-conversion? ? ? .

Frequency conversion, where electromagnetic fields of one or more frequencies are converted to fields of another frequency, is interesting for applications. One example are light sources, because the newly generated frequency is otherwise not available or underlies technical difficulties. Another example are detection schemes, where reasonably sensitive detectors of one frequency are not available, but for the converted one.

In this work, we deal with SHG, a nonlinear parametric process, i.e. the quantum state of the material stays unchanged. The important quantity, which describes this process is the second-order nonlinear material polarization including the associated second-order nonlinear susceptibility, which will be explained in the next subsection.

2.2.2. Second-order nonlinear susceptibility

As in linear optics, electromagnetic fields in nonlinear optics are governed by Maxwell's equations. The essential quantity to include the nonlinearity is the material polarization $\vec{P}$, in particular its nonlinear terms $\vec{P}^{(n)}$, with $n > 1$. In Maxwell's equations, these nonlinear terms represent sources for electric fields of different frequencies than they are generated by, which is a result of being proportional to products of the initial electric fields. The crucial coefficients accompanying these products are the nonlinear susceptibilities $\hat{\chi}^{(n)}$, tensors of rank $n+1$.

Since this work is focusing on SHG, this subsection is concentrating on the second-order nonlinear susceptibility $\hat{\chi}^{(2)}$ which governs the second-order nonlinear polarization as

$$\vec{P}^{(2)}(\omega_3) = \epsilon_0 \hat{\chi}^{(2)}(\omega_3; \omega_2, \omega_1) : \vec{E}_2(\omega_2)\vec{E}_1(\omega_1) \ . \tag{2.6}$$

The vectorial product, here denoted by the colon : between the third-rank tensor $\hat{\chi}^{(2)}$ and the vectorial fields $\vec{E}_1$ and $\vec{E}_2$, is best described by looking at the j-th component of the nonlinear polarization $P_j^{(2)}$:

$$P_j^{(2)}(\omega_3) = 2\epsilon_0 \sum_{j,k,l} \chi_{jkl}^{(2)}(\omega_3; \omega_2, \omega_1) E_{2,k}(\omega_2) E_{1,l}(\omega_1) \ , \tag{2.7}$$

where $E_{2,k}$ and $E_{1,l}$ are the k-th component of the second and the l-th component of the first initial field, respectively. As visible from these equations combined with the proportionality of $\vec{E}(\omega_3) \sim \vec{P}^{(2)}(\omega_3)$, the general second-order nonlinear process is a three-wave mixing.

The essential processes in the classical sense are sum frequency generation (SFG), where two fields of lower frequency (ω_1 and ω_2) generate a field of higher frequency $\omega_3 = \omega_2 + \omega_1$, and difference frequency generation (DFG), where a higher frequency field and a lower frequency field ($\omega_2 > \omega_1$) generate a field with a frequency that is the difference of the higher and lower initial frequencies ($\omega_3 = \omega_2 - \omega_1$).

How the newly generated electric field looks like depends on the vanishing and non-vanishing components of the second-order nonlinear susceptibility $\hat{\chi}^{(2)}$ which follow the symmetries of the crystal structure of the material. The strength and dispersion of the non-vanishing values depend on the actual distances and electronic behaviors of the crystal's atoms.

The most important property for a material to have non-vanishing components in the

second-order nonlinear susceptibility $\hat{\chi}^{(2)}$ is the breaking of the inversion symmetry, which means a non-centrosymmetric material.

In non-centrosymmetric materials, mirror and rotation symmetries can lead to vanishing components, to equal components or opposing components, where one component is equal to the negative of another component. For example, the second-order nonlinear material MoS_2 monolayer, which takes part in the experiments reported in the Chapters 6 and 7, is only two-dimensional (mirror symmetry with respect to the 2D-plane), it has a hexagonal crystal structure with a 120° rotational symmetry and a mirror symmetry in one plane perpendicular to the 2D-plane. In the right orientation, this leads to only four non-zero components of the 27 components in the $3 \times 3 \times 3$-matrix and one of these four has the negative value of each of the other three equal components. A derivation for the $\hat{\chi}^{(2)}$-components of MoS_2 monolayer is found in the appendix. The results can be seen in section 3.1, where the material is described in detail.

2.2.3. Second-harmonic generation

Second-harmonic generation (SHG) belongs to the nonlinear frequency conversion processes and was first observed shortly after the development of the first lasers[?] . In applications it is useful for example in Nd:YAG lasers where the original 1064 nm transition is frequency doubled, and provides a coherent light source at half the wavelength, 532 nm[?] . Nowadays, the process is successfully implemented in micro- and nanostructures, providing a new functionality in metasurfaces[?] . In this context, it is necessary to understand the origin and properties of the process. To simplify the description, we do not consider surface second-harmonic generation in this section, although it might be interesting to study in nano-structures where the surface-to-volume-ratio is increased with respect to bulk crystals or thin films[? ?] .

SHG is a special case of SFG, where the two lower energy fields have the same frequency ω, which means it is the same field, and thus generates a new field of double this frequency $\omega_{\mathrm{SH}} = 2\omega$. The initial field is called fundamental harmonic (FH) while the newly generated is called second harmonic (SH). Since the experiments described in the following chapters use the wavelength λ rather than the frequency for the spectral dependence of the process, it should be noted that the SH is at half the FH wavelength.

The process of SHG is governed by the nonlinear material polarization

$$P_j^{(2)}(2\omega) = \epsilon_0 \sum_{j,k,l} \chi_{j,k,l}^{(2)}(2\omega;\omega,\omega) E_k(\omega) E_l(\omega) \ . \tag{2.8}$$

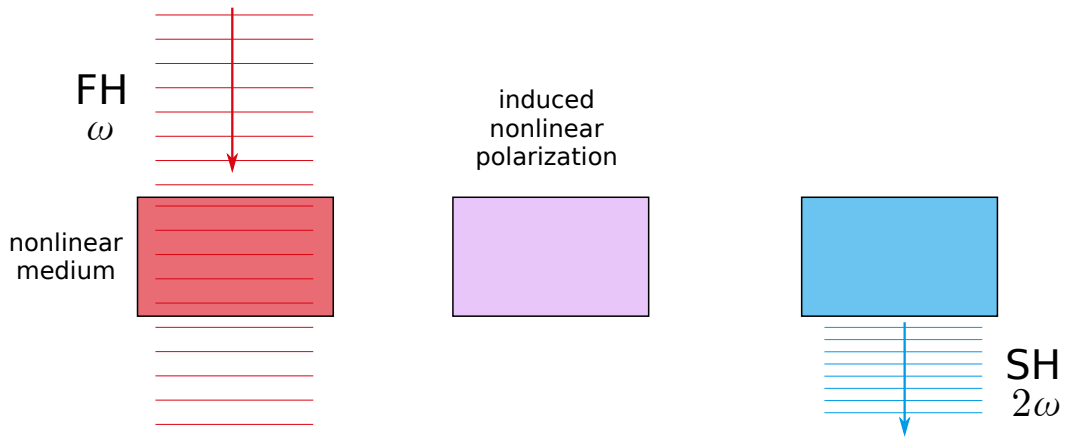

Figure 2.2.: Second-harmonic generation scheme.

In comparison with the general second-order nonlinear polarization from Eq. 2.7, the nonlinear polarization for the SHG is taking into account that not two but only one initial field $\vec{E}(\omega)$ is participating in the process, which removes the factor 2 in front of the sum as a kind of degeneracy factor.

In Maxwell's equations, the nonlinear polarization $\vec{P}^{(2)}(2\omega)$ acts as a source to generate a SH electric field

$$\vec{E}(2\omega) = \frac{1}{\epsilon_0}\vec{P}^{(2)}(2\omega) \ . \tag{2.9}$$

However, Maxwell's equations including this nonlinear polarization lead to coupled differential wave equations of the two fields, namely FH and SH field. Both fields influence each other. When light of SH is generated, the FH field is depleted. This is the so-called depletion of the pump. It is observable in bulk nonlinear crystal operations with high conversion efficiencies.

In the systems investigated in this work, this depletion does not play a role. The low conversion efficiencies result in a negligible change of the FH field. This simplifies the description of the SHG since the FH field can be taken as constant. This approximation is called the undepleted pump approximation. It reduces the SHG process to three steps depicted in Fig. 2.2: The FH field excites the nonlinear material and induces a second-order nonlinear polarization $\vec{P}^{(2)}(2\omega)$. This nonlinear polarization acts as a source for the SH electric field $\vec{E}(2\omega)$, which then radiates.

This three-step scheme is used in all SH simulations used in this work, where first the linear scattering of the FH with the nanostructures is calculated, then the field existent in the nonlinear material is used to compute the induced nonlinear polarization according to Eq. 2.8 and then use this as a source for the SH field which is again scattered by the

structures of the system.

An important issue for many SHG systems is the so-called phase matching. When the FH wave propagates through the nonlinear material volume, it generates SH fields at all places with its own phase differing in time and space during this propagation. The generated SH fields take over the FH's phase at this moment in this location. During their own propagation through the material they collect their own phase which typically differs from the FH phase due to material dispersion with respect to the difference of FH and SH wavelength. If these accumulated phases from one point to another do not match with the FH phase, the SH fields will interfere destructively.

Accordingly, just increasing the volume of a medium or the length of a waveguide made from the nonlinear material does not automatically enhance the SH output. To realize phase matching, the FH and SH wavelengths have to be chosen with respect to the material dispersion. A limiting and often impossible task.

So-called quasi-phase-matching can overcome this issue and leads to an increase of conversion efficiency over distance. For this, poling of the crystal orientation is used. The $\hat{\chi}^{(2)}$ is periodically inverted in space and - by proper design - counteracts the destructive interference of the generated SH in unpoled materials.

SHG in sub-wavelength structures, as they are used in the experiments reported in this work, does not need phase-matching. The oscillation of constructive and destructive interference only happens at interaction path lengths of more than a wavelength since the phase can counteract over these distances. In sub-wavelength structures the interaction length is too short to feel the phase difference between FH and SH field. This advantage helps a lot in reducing the design efforts of these structures. Nevertheless, many other constraints appear for the design process as described in the following chapters of this work.

2.3. Diffraction gratings

2.3.1. Periodic multiple slit arrangement

Radiation control is one of the aims using nanostructured surfaces. One essential effect for this purpose is diffraction of incoming or of generated light. With sub-wavelength structures, it is possible to control the light propagation in a few or even just one direction, while bulk diffractive optical elements typically produce multiple diffraction orders[?] . In

our work, diffraction of the generated second-harmonic can provide observability of the SH signal (see Chapter 5) and a realization of computer generated holograms (see Chapter 6).

A propagating wave, whether it is light or for example a liquid, will be diffracted when being confronted with an obstacle.

A typical textbook obstacle is the single slit in a barrier which otherwise blocks the incoming plane wave completely, e.g. in *Optics* by Hecht[?] . The light that is transmitted through the slit will be diffracted. The reason is Huygen's principle: every point of the wavefront which comes through the slit is a new point source.

In the case of a slit with transmission function $t(x)$ and an illuminating plane wave propagating in z-direction, the intensity pattern on a screen in the far field reproduces the shape of the Fourier transform of the slit. This actually only holds true in the paraxial Fraunhofer approximation, which not only assumes far field but also small angles in x-direction. That means the intensity pattern reproduces the Fourier transform only in a certain surrounding of the center.

If another slit is put close, the transmitted light through both slits interferes. Considering the same shape of the second slit, the radiation pattern is still influenced by the same Fourier transform, which is now an envelope around the interference maxima.

The next step is the generalization towards a one-dimensional finite multiple slit experiment. Here, an arrangement of a finite number N of equidistant slits of the same shape is chosen. This periodic but finite arrangement of sources as which the slits act, can be denoted as a sum of N transmission windows $t(x)$ all shifted by the distance d in x-direction,

$$t_N(x) = \sum_{n=0}^{N} t(x + nd) \ . \tag{2.10}$$

The according Fourier transform of one slit is $T(k_x)$. The Fourier transform of the summed up slits relates as

$$T_N(k_x) \sim T(k_x) \ \frac{\sin^2(Nk_x d/2)}{\sin^2(k_x d/2)} \ . \tag{2.11}$$

Then the intensity pattern $I_N(x)$ at a screen at the position $z = z_1$ far away from the slits results in

$$I_N(x) = |t_N(x)|^2 \sim \left| T_N(k_x = k_0 \frac{x}{z_1}) \right|^2 \sim T(k_x = k_0 \frac{x}{z_1}) \ \frac{\sin^2(Nk_0 xd/2z_1)}{\sin^2(k_0 xd/2z_1)} \ . \tag{2.12}$$

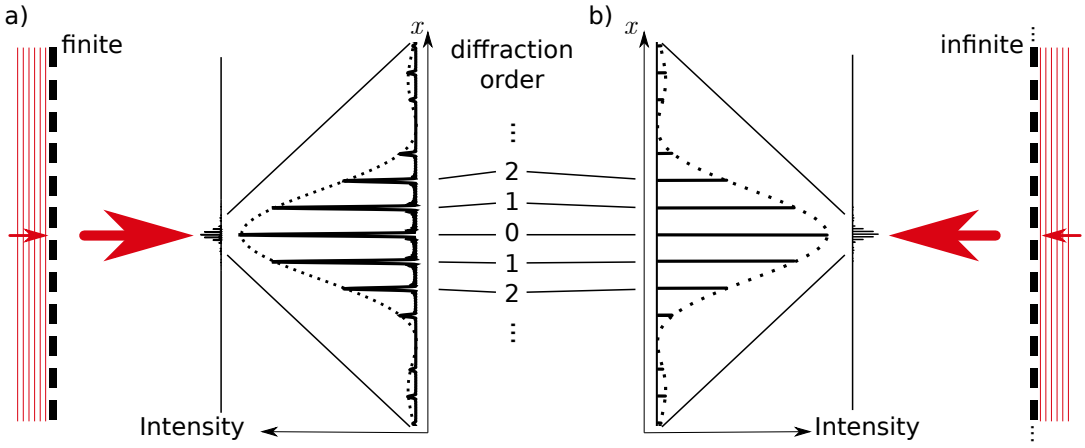

Figure 2.3.: a) Periodically arranged multiple slits. b) Infinite periodic arrangement.

The visualization of this pattern is shown in Fig. 2.3(a) for a multiple-slit arrangement using a simple aperture in one dimension as a slit. The Fourier transform of this slit is a sinc-function and is depicted here as the dashed envelope. The pattern provides areas of high intensity separated from each other by areas of suppressed intensity. The high intensity areas can be called diffraction orders, starting with the central zero diffraction order, followed by the first, second, and higher orders which go in both positive and negative x-direction.

An infinitely periodic system of slits or sources is often referred to as a grating. Its infiniteness, at least in theory, leads to the simple results of diffraction orders as discrete states (delta distributions) for which reflection or transmission is allowed and the areas in between, where the light propagation is suppressed to 0 by destructive interference.

The mathematical description differs from the (multiple) slit formula above. Due to the infinite periodicity of the transmission function $t_\infty(x) = t_\infty(x + d)$, it is possible to describe it as a Fourier series, which leads to a sum of delta distributions in the far field spectrum.

Similar to the maxima of the spectrum resulting from a finite multiple slit arrangement, the delta distributions are located at x_n satisfying $\frac{2\pi n}{d} = k_0 \frac{x_n}{z_1}$, being the positions of the n-th diffraction order on the screen. A visualization of this intensity pattern is shown in Fig. 2.3(b) showing the sinc-function as the Fourier transform of the slit's transmission function representing the envelope around the discrete diffraction order maxima.

Fig. 2.3 already visualizes the difference between the theoretical infiniteness and the typically experimental finiteness of periodic arrangements: the more slits are used, the sharper the diffraction orders are in the spectrum. However, the envelope of the spectrum

as the Fourier transform of the single slit itself stays intact.

As mentioned before, the approach with the Fourier transform only holds true for the far field, i.e. large z_1, and small angles in x-direction, i.e. small numbers of diffraction orders n. The positions of higher diffraction orders deviates. However, for small angles, the propagation angle α_n of the n-th diffraction order can be approximated by

$$n\frac{\lambda}{d} = \frac{x_n}{z_1} = \tan(\alpha_n) \approx \sin\alpha_n \ . \tag{2.13}$$

The relation for the propagation angle α_n of the n-th diffraction order can be also found in a simpler geometrical picture, without the small angle approximation and even including an angle of incidence α_i, as for example described in[?] ,

$$n\frac{\lambda}{d} = \sin(\alpha_n) - \sin(\alpha_i) \ . \tag{2.14}$$

From Eq. 2.14, the Rayleigh anomaly, mentioned before in Section 2.1.3, can be explained conceptually (for further reading find[?]). In a grating with a fixed period and assuming a fixed incident angle, the propagation angle α_n of the n-th diffraction order depends on the wavelength λ of the incident plane wave. If the term $n\frac{\lambda}{d} + \sin(\alpha_i)$ goes to 1, α_n becomes 90° and therefore propagates tangential along the grating. Even higher values lead to non-propagating diffraction orders. At this 'passing-off'[?] for the n-th propagating diffraction order, Rayleigh's anomalies appear.

Of course, the shown diffraction formulas can be generalized for two-dimensional periodic gratings or even periodicity in more directions in one plane. This is crucial for usually two-dimensional periodic metasurfaces and especially hologram designs. Here, the metasurface unit cells, also called meta-atoms, form the envelope of the angular spectrum with their individual radiation pattern, convoluted by the periodicity with maxima at the diffraction orders.

In the experiment, depending on the number of periods existent and excited, the observed radiation patterns are closer to the multiple slit experiment or an infinitely periodic grating. The position of the diffraction orders, however, is the same in both cases. In the experiments reported in this work, the angular radiation pattern is not observed as a farfield pattern, but directly as the angular spectrum, i.e. the Fourier transform. The mechanism here is back-focal plane imaging described in Section 4. Another difference is, that not the diffracted light of the initial exciting field is observed, but of the generated SH field, the so-called SH diffraction, which is shortly described in the next subsection.

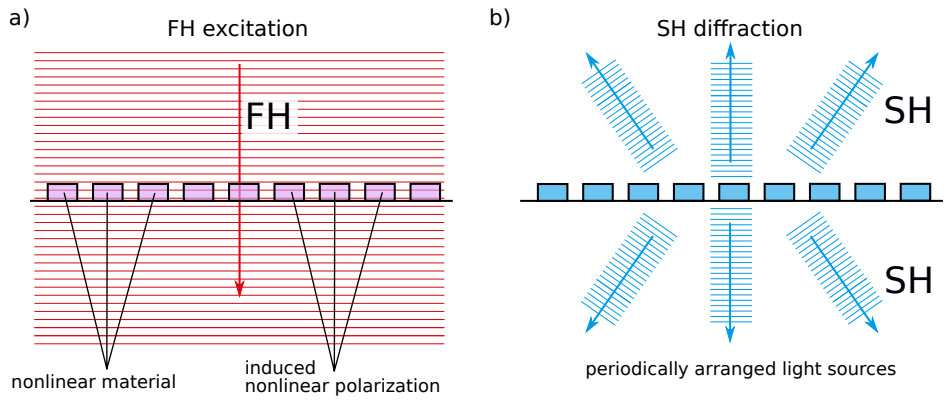

Figure 2.4.: Scheme of SH diffraction.

2.3.2. Second-harmonic diffraction

The term 'second-harmonic diffraction' might not be prominent in the literature, since it is not found in books describing fundamentals of optics, but it is used in several publications[? ? ? ? ? ? ? ?] , to name just a few. It describes the combination of the nonlinear process of SHG and the diffraction of just this generated SH light. Each of the last three chapters of this work, which deal with the experimental results, contains SH diffraction measurements whether playing a major role or being a side tool for experimental proof.

SH diffraction appears when structures, which are either made from second-order nonlinear materials or adjacent to such, create SH sources whose propagating fields interfere with each other. The diffraction itself has nothing to do with the nonlinear process of SHG and it is still a linear process itself. In 'regular' diffraction an electromagnetic field is propagating towards structures and then is influenced by their appearance leading to destructive and constructive interference. In SH diffraction, the initial incoming light, i.e. the FH field, is exciting the nonlinear material which generates the SH light that then is diffracted. The interference of the SH light results from the spatial arrangement of sources at the SH wavelength. The FH field, however, might add different phases to the generation of the SH light, if the excitation happens under an oblique angle with respect to the structures.

Due to its periodic arrangement in the experiments reported in this work, these multiple sources interfere with each other leading to propagating diffraction orders at the SH wavelength. The process of SH diffraction is exemplarily shown in scheme of Fig. 2.4, where a FH field excites a periodic arrangement of nonlinear structures which induces a nonlinear polarization which generates a SH field which then propagates in different angles while the propagation in other angles is suppressed. Due to the small sub-wavelength structures with its field confinement even back propagation can be a result of the SH

diffraction.

The important characteristic of the SHG which enables this SH diffraction is the coherence which arises from the combination of its parametric nature and the use of a coherent light source as the FH, e.g. a laser. The amplitudes of the different SH fields generated in an ensemble of structures add up or subtract from each other depending on their relative phases. The appearance of diffraction orders from periodically arranged structures needs a stable phase relation over the initial light field which excites the ensemble. This stable phase relation is available in the case of a plane wave excitation of a periodic slit experiment. In the experiments reported in this work, the different SH fields from the different metasurface unit cells have a fixed phase relation to each other due to the coherent FH laser source and thus a coherent SH field is generated which can exhibit SH diffraction.

Since functionalizing surfaces is a path for future applications, diffraction from structured surfaces which are able to produce efficient nonlinear frequency conversion processes is a great opportunity to control and manipulate light in and from such surfaces. In the experiments reported in Chapter 5 and Chapter 6, SH diffraction plays an important role.

3. Second-order nonlinear materials

3.1. Two-dimensional MoS_2 monolayers

3.1.1. General properties

Two-dimensional (2D) materials are crystalline mono-atomic or mono-molecular layers and got their name due to their ultrathin thickness. Their dimensionality and their particular crystal structures lead to special electronic and optical properties[? ? ? ? ? ? ?], which can be manipulated by strain, external fields and doping[? ? ? ? ? ? ? ?]. Due to their flat topology, 2D materials can be coupled to other materials or structures providing improved or even new properties or application options[? ? ? ? ? ? ?]. It is also possible to stack these 2D layers creating heterostructures[? ? ?].

This dissertation intends to show possibilities to use the second-order optical nonlinearity of 2D materials in structured surfaces. Thus, this section is kept short, presenting major properties connected to optics, especially the second-order nonlinear response. Additionally, the growth, transfer and patterning mechanism used for the investigated samples are described.

Since the discovery of the 2D material graphene[?], transition metal dichalcogenides (TMDs) have sparked a huge interest of researchers in optics and electronics. This group of semiconducting materials is described by the chemical formula MX_2 with M standing for a group VI metal like molybdenum (Mo) or tungsten (W) and X standing for chalcogenes like sulfur (S), selen (Se) or tellurium (Te). The bulk TMD is only seldomly used in the optical community due to its indirect band gap.

The crystal structure of TMDs is based on mono-molecular, van der Waals-bound layers. It is possible to thin down the material by exfoliation to a stack of very few layers and eventually to the limit of a single molecular layer of $\sim$0.7 nm thickness, the so-called monolayer. While a bilayer still possesses an indirect band gap, the band structure of a monolayer drastically changes. The lowest energy transition becomes direct at the K-point[?]. Recently the chemical vapor deposition (CVD) growth of TMD single crystals can be accurately controlled to achieve high quality monolayers of large areas[?]. In this work, only CVD grown monolayers are used for the experimental investigations.

In contrast to usual bulk semiconductors, TMD monolayers exhibit excitons with strong binding energies. Excitons are hydrogen-like states formed by an electron and a hole due

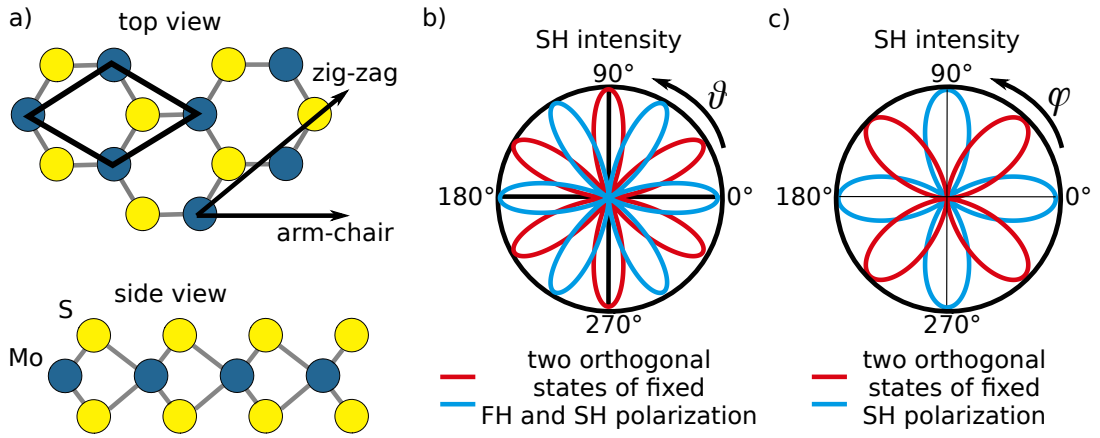

Figure 3.1.: a) Crystal structure of MoS_2 monolayer shown from top and from the side in armchair direction. b) SH intensity dependent on the rotation angle θ of the crystal orientation at fixed linear FH and SH polarization. c) SH intensity dependent on the rotation angle ϕ of the linear FH polarization at fixed crystal orientation and linear SH polarization.

to Coulomb interaction. Resulting from high electron mobility and thus high quasiparticle effective mass in the TMD monolayers, the dielectric screening is low and thus the binding energy of the excitons is large[?] . This effects especially the absorption and photoluminescense of the material. Additionally, trions, i.e. bound states of two electrons and one hole or one electron and two holes, have been observed for TMD monolayers[?] .

TMD monolayers have a hexagonal crystal structure. As exemplarily depicted in Fig. 3.1 for a molybdenum disulfide (MoS_2) monolayer, the unit cell consists of two different kinds of atoms. While the molybdenum atom is single, the sulfur atom visible from the top view is actually two atoms, just deplaced in the direction normal to the 2D plane as visible from the side view. The crystal symmetry belongs to the D_{3h} space group. It is non-centrosymmetric, i.e. it has no inversion center. From the top view, the mirror plane through the arm-chair direction is clearly visible. Another mirror plane is the 2D-plane itself, seen in the side view.

From the break of the inversion symmetry, two interesting properties follow: second-order nonlinearity and spin-valley coupling. The former will be dealt with in the next subsection. The latter is connected to the so-called valleys of semiconductors, which describe minima in the electronic band structure. Due to the lack of inversion symmetry, the valleys at the K-points of different sign ($K^{\pm}$) in the hexagonal Brillouin-zone are not equivalent[?] . These valleys can couple with the split spin states, which are degenerate due to the heavy atoms and their outer-shell d-orbital electrons which exhibit a strong spin-orbit coupling. The resulting possibility to address specific electronic states (valley $\pm$ and spin up-down) by different initial optical excitations[?] is called valleytronics.

MoS_2 monolayers have been heavily investigated due to their large availability, as bulk crystals for exfoliation or as precursors in the form of molybdenum trioxide (MoO_3) for growth processes, in contrast to its tungsten relatives or molybdenum diselenid. Photoluminescence of MoS_2 monolayers shows three important transitions in the visible light range. The first two transitions around 680 and 650 nm, called A- and B-exciton, are connected to excitons describing the direct band gap at the K-point split by the before mentioned spin-orbit coupling. The third transition around 420 nm, often called C-exciton, is actually governed by band nesting[?] , i.e. a region of constant energy spacing between conduction and valence band in the Brillouin zone.

The C-transition provides the strongest second-order nonlinear response for MoS_2 monolayers[? ?] . Further information on the nonlinear response follows in the next subsection.

3.1.2. Second-order nonlinear response

TMD mono- and few-layer crystals with an odd number of layers exhibit a second-order nonlinear response due to their non-centrosymmetric crystal structure[? ? ? ? ? ?] . The top view onto the crystal structure of a monolayer, as seen in Fig. 3.1(a), shows a broken inversion symmetry. This is especially visible in the unit cell framed by the black rhombus around 4 Mo-atoms: the enclosed S-atom is not centered which would be necessary for inversion symmetry, but it is displaced from the center.

The inversion symmetry is reestablished when another layer is naturally grown on top and adds up the unit cell. Another additional layer again creates the asymmetry. This change of symmetry holds only until the thickness of the few-layer system stays small enough. Therefore the second-order nonlinear response decreases with increasing, but still odd number of naturally grown layers while the bulk shows none[?] .

Due to the crystal structure symmetries, the second-order nonlinear susceptibility tensor $\hat{\chi}^{(2)}$ in the orientation of the armchair direction being parallel to the x-direction, has only four non-vanishing elements which additionally have the same absolute value and differ only in the sign:

$$\chi_0^{(2)} := \chi_{xxx}^{(2)} = -\chi_{xyy}^{(2)} = -\chi_{yxy}^{(2)} = -\chi_{yyx}^{(2)} \ . \tag{3.1}$$

A derivation for this $\hat{\chi}^{(2)}$ can be found in the appendix.

The simple structure of the $\hat{\chi}^{(2)}$-tensor stems from the planar structure, where the interaction of the atoms with the electric field only happens again in the plane. From equation 2.8 in Section 2.2, it can be deduced that only x- and y-polarized FH electric

fields contribute to the second-order nonlinear polarization $\vec{P}^{(2)}$ as

$$\begin{aligned} P_x^{(2)} &= \epsilon_0 (E_x^2 - E_y^2) \ , \\ P_y^{(2)} &= -2\epsilon_0 E_x E_y \ . \end{aligned} \tag{3.2}$$

Rotating the flake around the axis normal to the 2D material plane (z) with an angle θ, the $\hat{\chi}^{(2)}$-tensor changes:

$$\hat{\chi}^{(2)} = \begin{pmatrix} \begin{pmatrix} \cos(3\theta) & \sin(3\theta) \\ \sin(3\theta) & -\cos(3\theta) \end{pmatrix} \\ \\ \begin{pmatrix} \sin(3\theta) & -\cos(3\theta) \\ -\cos(3\theta) & -\sin(3\theta) \end{pmatrix} \end{pmatrix} \chi_0^{(2)} \ , \tag{3.3}$$

where the $3 \times 3 \times 3$-tensor is already reduced to a $2 \times 2 \times 2$-tensor due to the vanishing z-components.

The second-order nonlinear polarization for second-harmonic generation then reads:

$$\begin{aligned} P_x^{(2)} &= \epsilon_0 \chi_0^{(2)} \left[\cos(3\theta) \left(E_x^2 - E_y^2 \right) + 2 \sin(3\theta) E_x E_y \right] \ , \\ P_y^{(2)} &= \epsilon_0 \chi_0^{(2)} \left[\sin(3\theta) \left(E_x^2 - E_y^2 \right) - 2 \cos(3\theta) E_x E_y \right] \ . \end{aligned} \tag{3.4}$$

Using this nonlinear polarization, we can derive the FH polarization dependence and the flake orientation dependence of the SH signal. With $E_x^{SH} \sim P_x^{(2)}$ and $E_y^{SH} \sim P_y^{(2)}$, the SH intensity at a fixed linear polarization is usually obtained for two regimes with two different outcomes.

A six-fold symmetry, as depicted in the polar plot in Fig. 3.1(b), can be found for a fixed FH polarization and a fixed SH polarization while the flake is rotated around the optical axis. Without loss of generality, we chose FH polarization x and SH polarization x, while we rotate the flake by angle θ following Equation 3.4. The result has a six-fold symmetry with its six maxima over 360° described by

$$\begin{aligned} I_x^{SH} &= |E_x^{SH}|^2 \sim |P_x^{(2)}|^2 \\ &\sim |\chi_0^{(2)} \left[\cos(3\theta) \left(E_x^2 \right) \right]|^2 \\ &\sim \cos^2(3\theta) \ . \end{aligned} \tag{3.5}$$

This behavior was presented in the first SHG investigations on MoS_2 monolayers[? ?] .

A four-fold symmetry, as depicted in the polar plot of Fig. 3.1(c), can be obtained when the SH polarization and the flake orientation are fixed, but the FH polarization is rotated by an angle ϕ. Again, without loss of generality, we chose the SH polarization in x-direction and the flake orientation with armchair-direction parallel to the x-direction.

The FH polarization is then modelled as $E_x = E_0 \cos(\phi)$ and $E_y = E_0 \sin(\phi)$. Following Equation 3.2, a dependence is found which has four maxima over 360° as

$$\begin{aligned} I_x^{SH} &= |E_x^{SH}|^2 \sim |P_x^{(2)}|^2 \\ &\sim |\chi_0^{(2)} \left(E_x^2 - E_y^2\right)|^2 \\ &\sim |E_0^2(\cos^2(\phi) - \sin(\phi)^2)|^2 \\ &\sim \cos^2(2\phi) \ . \end{aligned} \tag{3.6}$$

This behavior is observed in the measurements reported in this thesis, since the setup does not allow for the rotation of the sample, the FH polarization however is rotatable (see Section 4.1).

In contrast to the linearly polarized SH intensity, the overall SH intensity $I^{SH} = |E_x^{SH}|^2 + |E_y^{SH}|^2$ is not dependent on the FH polarization or crystal orientation rotation. For the derivation, the nonlinear polarization from Equation 3.4 is used with the crystal rotation angle θ and the rotating FH polarization modelled as $E_x = E_0 \cos(\phi)$ and $E_y = E_0 \sin(\phi)$:

$$\begin{aligned} I^{SH} &= |E_x^{SH}|^2 + |E_y^{SH}|^2 \sim |P_x^{(2)}|^2 + |P_y^{(2)}|^2 \\ &\sim |\chi_0^{(2)} \left[\cos(3\theta)\left(E_x^2 - E_y^2\right) + 2\sin(3\theta)E_xE_y\right]|^2 \\ &\quad + |\chi_0^{(2)} \left[\sin(3\theta)\left(E_x^2 - E_y^2\right) - 2\cos(3\theta)E_xE_y\right]|^2 \\ &\sim \cos^2(3\theta) + \sin^2(3\theta) \\ &\sim 1 \ . \end{aligned} \tag{3.7}$$

The value of $\chi_0^{(2)}$ is dependent on the FH/SH wavelength, i.e. it is spectrally dispersive. While the polarization and rotation dependence is the same for all TMD monolayers, the spectral dispersion of $\chi_0^{(2)}$ is material dependent and eventually even dependent on the surrounding, similar to the linear susceptibility of TMDs. Reported values for $\chi_0^{(2)}$ differed in the first publications due to different units and conventions. At the C-transition of MoS_2 monolayers, $\chi_0^{(2)} \approx 130$ pm/V is reported to be a reasonable value[??] .

An overview on the dispersion of the second-order nonlinear susceptibility is given by Weismann *et al.*[?] , showing the spectral dispersion of the SH response, for three of the four major TMD monolayers MoS_2, $MoSe_2$, WS_2 and WSe_2. It appears, that the SH response is larger around the absorption peaks, i.e. the A- and B-excitons as well as the C-transition. This behavior similar to photoluminescence enhancement is due to excitonic

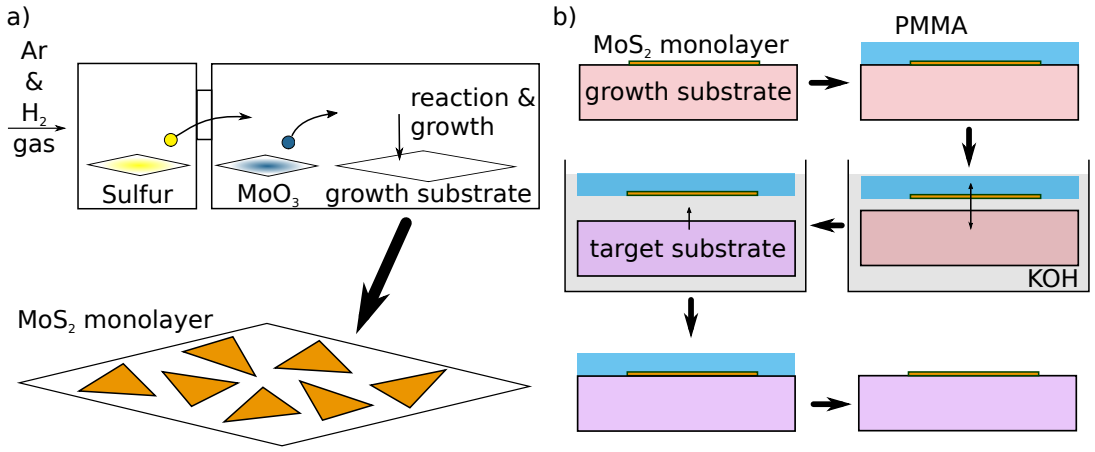

Figure 3.2.: a) Scheme for growth of MoS_2 monolayers by chemical vapor deposition. b) Scheme for PMMA assisted wet transfer method.

resonances[?] .

In MoS_2 monolayers, the excitonic resonance at the C-transition provides a far stronger SH response than the A- and B-excitons. The experiments reported in the later chapters use the C-transition around 420 nm using a tunable laser emitting around double this wavelength for the FH excitation (see Section 4.1).

3.1.3. Growth and transfer

For the convenient use in applications, large area TMD monolayers have to be available and either be grown or transfered on the target surface or structures. For the projects reported here, MoS_2 monolayers were CVD grown by the group of Andrey Turchanin, Institute of Physical Chemistry, Abbe Center of Photonics at the Friedrich Schiller University Jena. The responsible scientist for the growth was Antony George. This subsection is briefly introducing the growth protocol they developed[?] .

While exfoliation of TMDs via adhesive tape from bulk crystals usually leads to a low yield of small area monolayer crystals in a conglomeration of few-layer crystals, the quality of crystalinity is very good. It is possible to transfer these crystals with high positioning accuracy via a stamp of poly(methyl methacrylate) (PMMA) and polydimethylsiloxane (PDMS)[? ? ? ?] .

CVD however, can result in large areas of monolayer crystals in a bottom-up process. In principle, the MoS_2 crystals grow layer by layer from precursors of MoO_3 and S_2 from the gas phase. The optimization of temperature, pressure, gas flow and precursor density is the key to grow high quality large area monolayer crystals.

The growth process is conducted in a two zone split tube furnace, to control the in-

dividually needed temperatures of the precursors. A sketch is shown in Fig. 3.2(a). In the first zone, S_2 powder is heated. In the second one, MoO_3 powder is heated and the growth substrate is positioned. An argon and hydrogen gas flow is controlling the mixing of the materials to initialize the reaction to form MoS_2 and the growth on the substrate. By choosing the right temperature and pressure conditions, triangular shaped MoS_2 monolayers are formed.

For hybrid structures, where MoS_2 monolayer crystals are atop nanostructures, a wet transfer method is used to move the MoS_2 monolayer crystals from the growth substrate onto a different substrate containing the target structures. Up to now, this procedure does not allow for precise positioning of the monolayer crystals, but statistically due to many large area monolayer crystals a successful transfer of monolayers on top of the target structures can be realized. A dry transfer with high positioning accuracy of single monolayer crystals via a stamp[? ? ? ?] as successfully used with exfoliated crystals was not available for the projects described in this work using CVD-grown MoS_2 monolayers.

The wet transfer follows a protocol using a thin film of PMMA as an intermediate substrate[? ? ?] as visualized in Fig. 3.2(b). First the monolayers on their growth substrate are covered by the thin film of PMMA. Further, the whole construct is flooded by a weak potassium hydroxide (KOH) solution, resulting in the PMMA together with the monolayers being detached from the growth substrate and thus swimming in the liquid with the monolayer crystals facing toward the bottom of the liquid reservoir. The target substrate can be inserted into the reservoir, submerging under the swimming monolayer-PMMA-system. Finally the target substrate can be lifted up out of the reservoir being covered by the monolayer-PMMA-system. Via a microscope, this can be controlled slightly to push areas of high density of monolayer crystals toward the target structures or areas of interest on the target sample. The monolayer-PMMA-system is fixed onto the target sample by drying. The PMMA then is lifted off by acetone and liquid carbon dioxide as a supercritical fluid in a critical point dryer.

3.1.4. Patterning via focused ion beam milling

To fabricate very small structures into plane materials of a certain thickness, several techniques have been developed, like electron beam lithography. For ultrathin materials like TMD monolayers, lithography methods were investigated[? ?], but also challenging, as needed etchant fluids can destroy the monolayers.

A more precise method to remove parts of the TMD monoalyers to create structures

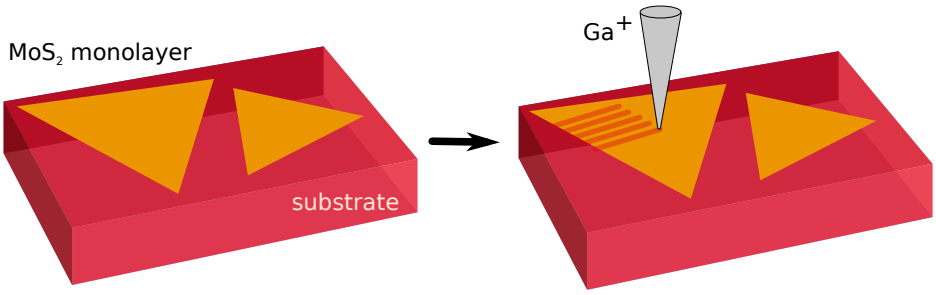

Figure 3.3.: Fabrication scheme: FIB milling of MoS_2 monolayers.

is focused ion beam (FIB) milling. FIB machines are used for many applications such as material deposition, metrology and direct-write processing, where milling and ion implantation are included[? ? ?] . The principle of the technique is based on electronically accellerated ions which are focused onto a sample. Depending on the focus conditions, the density and velocity of the particles, and thus on the energy and momentum which is interacting with the target atoms rather than the whole material, the particles are penetrating deeper or more shallow into the surface. Thereby, the ions are pushing other particles away or even knocking them out of the substrate. Implantation of ions can lead to doping effects and crystal lattice amorphization. The removal of parts of material is called FIB milling and can be used to structure materials, and under certain conditions even ultrathin materials like TMD monolayers[? ? ? ? ?] .

In contrast to the lithography which can rapidly structure large areas, FIB techniques usually work on a point-by-point process, where the FIB is moved step by step along paths where material has to be manipulated. This can provide high precision due to tight focusing, but it does need long times to structure large areas or complicated and deep patterns.

In this work, FIB milling is used to produce gratings and even more complicated computer generated holograms into MoS_2 monolayer flakes[?] , as described in Chapter 6. A sketch of the fabrication scheme is shown in Fig. 3.3. Due to the very thin thickness, material is easily removed or at least altered by energetic particles hitting the material. This problem is noticed also in scanning electron microscopy (SEM) to investigate TMD monolayers, where energetic electrons destroys the ultrathin material. Accordingly SEM cannot be used to investigate 2D materials.

To deal with these circumstances, in this work Ga-ions are accelerated to an energy of 30 keV at a reduced ion current of 1.1 pA for a very small excitation spot. Higher currents lead to bigger excitation spots and thus to a lower resolution for the wanted patterns, although with lower currents less material can be removed. High energies help to focus the

ion beam. However, higher energies result in deeper penetrations into the substrate and stronger lateral scattering and removal of atoms inside the substrate. Scattered particles, also secondary kicked-out particles from the substrate, can reach the surface again and destroy areas which are not intended to be manipulated by the initial FIB.

The conditions used here, ensure a low enough dose to only remove material in the wanted area. It is rather beneficial to use a lower dose while performing the path several times to provide the quality of the pattern than to destroy areas which should stay intact. Here[?] , the path was repeated 20 times, resulting in an overall dose of ~ 11 ions/nm^2.

Despite the used small doses, Ga-ions penetrate and thus alter the substrate below the MoS_2 monolayer since its thickness is less than 1 nm. The Ga-ion implantation leads to an amorphization of the Si substrate and thus results in a volume increase which is observed in atomic force microscope (AFM) measurements of MoS_2 monolayer grating patterns (see Chapter 6). Another issue can be debris of removed material which might appear on areas of interest and might even form bigger clusters.

MoS_2 monolayers and other 2D materials have exhibited a huge interest alongside this dissertation and are still under investigation, nowadays more application driven than 5 or 10 years ago. In this work, CVD-grown MoS_2 monolayers are investigated with respect to their second-order nonlinear response. The two directions reported in later chapters are SH diffraction on patterned MoS_2 monolayers in Chapter 6 and SHG from a hybridized metasurface resulting from a MoS_2 monolayer covering a resonant silicon (Si) metasurface in Chapter 7.

3.2. GaAs

3.2.1. General properties

In addition to the Si-based semiconductor technology, gallium arsenid (GaAs) and its relatives aluminum arsenid and indium arsenid as well as their mixtures provide light-emitting application possibilities, which are not possible with Si. In this work, the particular property of second-order nonlinearity stands in the focus, used in a disk metasurface (see Chapter 5). The properties, especially the second-order nonlinear response are described in this section followed by a small description on the nanostructuring as it was performed for the sample used in this work's experiments.

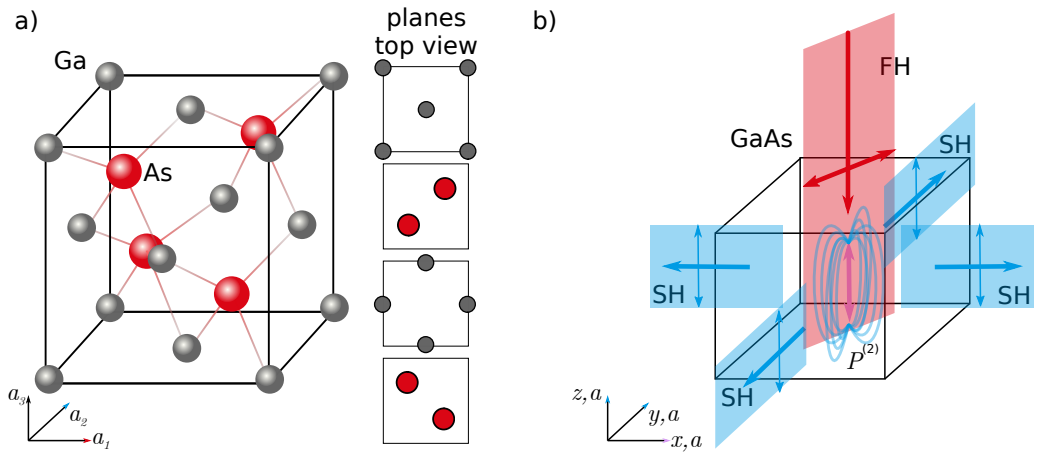

Figure 3.4.: (a) GaAs crystal structure, zinc blende with two different atoms. Two equivalent crystal axes, here denoted a_1 and a_2 and a third axis c. (b) SHG scheme, with a $x+y$-polarized FH inducing a z-polarized nonlinear polarization resulting in SH propagating in x- and y-directions, but not in z.

GaAs is a III-V semiconductor, composed from the group-III element gallium (Ga) and the group-V element arsenic (As), with a cubic crystal structure of the space group F$\bar{4}3m$, which is an isotype of the zinc blende structure. The structure is visualized in Fig. 3.4(a). This structure has 3 equivalent crystal axes, which here are denoted a_1, a_2, and a_3.

In contrast to group-IV semiconductors like Si and germanium, GaAs has a direct band gap. It is spectrally situated around 870 nm at room temperature. All shorter wavelengths exhibit strong absorption. Accordingly, resonant structures made from GaAs as reported in Chapter 5 provide useful resonant structures only at wavelengths above 870 nm.

In bulk GaAs, excitons do not have the impact as they have in 2D materials due to the smaller binding energies. In heterostructures with other III-V-semiconductors, especially quantum wells, excitons become more relevant again due to the stronger confinements[?] .

Due to its noncentrosymmetric crystal structure (see Fig. 3.4(a)), GaAs shows a second-order nonlinear response, which is described in detail in the next subsection. Its nonlinear properties are used in resonant nanostructures, but also in quantum well and quantum dot structures.

3.2.2. Second-order nonlinear response

In contrast to Si, GaAs has not only a direct band gap, but also exhibits a second-order nonlinear response when excited. Due to the zinc blende crystal structure with two different atoms as shown in Fig. 3.4(a), the inversion symmetry of the bulk material is broken. Considering the three equal crystal axes parallel to the x-, y- and z-axes of a cartesian coordinate system, the second-order nonlinear susceptibility tensor $\hat{\chi}^{(2)}$ elements

read as follows:

$$\chi_0^{(2)} := \chi_{xyz}^{(2)} = \chi_{yzx}^{(2)} = \chi_{zxy}^{(2)} = \chi_{zyx}^{(2)} = \chi_{yxz}^{(2)} = \chi_{xzy}^{(2)} \ . \tag{3.8}$$

All tensor elements vanish, except for the six equally valued components where the three indices have to be all different. A reported value with the SH around 400 nm is $\chi_0^{(2)} = 750$ pm/V[? ?] .

The resulting second-order nonlinear polarization for SHG following equation 2.8 contains all three components $P_x^{(2)}$, $P_y^{(2)}$, and $P_z^{(2)}$ as

$$\begin{aligned} P_x^{(2)} &= \chi_0^{(2)}\, 2\, E_y E_z \ , \\ P_y^{(2)} &= \chi_0^{(2)}\, 2\, E_x E_z \ , \\ P_z^{(2)} &= \chi_0^{(2)}\, 2\, E_x E_y \ . \end{aligned} \tag{3.9}$$

This implicates that an FH excitation polarized in direction of only one crystal axis does not generate any SH signal. Mixed FH polarizations composed of two crystal axis directions create SH signals polarized in the direction of the third axis. This phenomenon is visualized in Fig. 3.4(b), showing the FH polarized in $x+y$-direction while the resulting SH is polarized in z-direction and therefore propagating in the plane perpendicular to z. Accordingly, the propagation direction changes with respect to the FH. As a result, typical SHG schemes of FH and SH propagating on the same optical axis, do not work efficiently.

To still exploit the significant second-order nonlinearity, the radiation direction has to be manipulated. Observation in normal direction to the surface is still a challenge, corresponding schemes use oblique incidence of the FH[? ?] or respectively cut crystal surface orientations[?] , or complicated vectorial fields in resonant nanostructures as are presented in this work (see Chapter 5).

3.2.3. Growth and fabrication of nanostructures

Since GaAs is an artificial material, it has to be grown by chemical means. Large wafers are cut from crystals grown out of liquefied Ga and As. Other processes are (metal-organic) chemical vapor deposition and molecular beam epitaxy. The sample used in the experiment reported in Chapter 5 was fabricated by the group of Igal Brener at Sandia National Laboratories Albuquerque, USA. The description of the fabrication follows the publications[? ? ?] .

For the sample described in this work (see Chapter 5), molecular beam epitaxy is used to fabricate the GaAs bulk substrate. In this process, Ga and As_4 are heated into gaseous phase and condense on the target while reacting to GaAs. By careful dosing of both

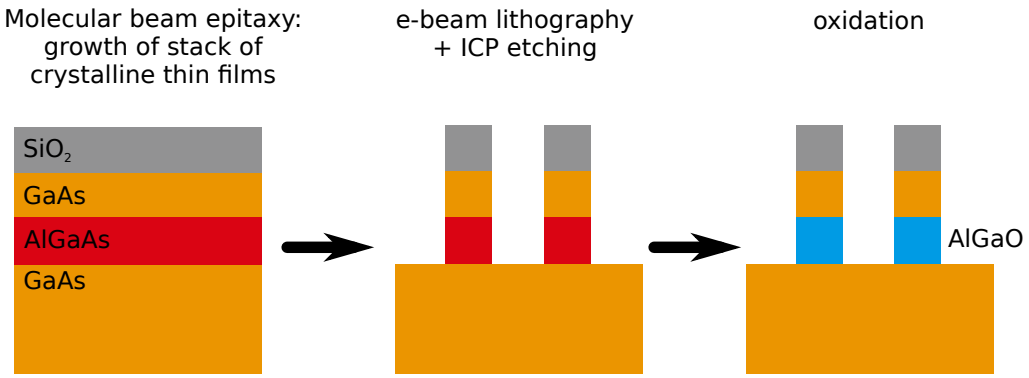

Figure 3.5.: Fabrication scheme.

materials, the growth in a single crystalline thin film can be accomplished. To create micro- and nanostructures out of GaAs thin films, lithography and etching processes are used. To realize small structures in sub-micrometer range, electron beam lithography is the method of choice. SiO_2 patterns are fabricated on top of the GaAs via e-beam lithography and then etched into the thin film via inductively coupled plasma (ICP), leaving GaAs structures on top of a GaAs substrate. The direct contact between nanostructure and substrate from the same material might weaken the light confinement in the structures since the interface between substrate and resonator material is not providing a clear material property change.

To realize clear and strong resonances, an additional layer is included (see Fig. 3.5). By growing an AlGaAs thin film on top of the GaAs substrate followed by an additional GaAs thin film, stacks of GaAs layers separated by AlGaAs can be produced[?] . After the etching process of structures, the AlGaAs then can be oxidized, independent from the GaAs. The oxidation changes the refractive index of the layer drastically from 3.6 to 1.6 and provides a perfect optically isolating layer between the GaAs structures and the substrate. Thus, strong confinement in the isolated GaAs resonators can be achieved.

GaAs is established for certain applications in the semiconductor applications ranging from electronics to optics. The work reported in Chapter 5 is part of several studies during this work's duration, shedding light on the use of GaAs and similar III-V semiconductors for nonlinear photonic nanostructures and metasurfaces[? ? ? ? ?] .

4. Second-harmonic microscopy setup

4.1. Second-harmonic imaging

4.1.1. Principle of measuring second-harmonic generation

With laser sources which can excite materials with a highly intense energy density, it is possible to realize nonlinear optical measurements. Nevertheless, many constraints and challenges accompany these experiments. Second-harmonic (SH) imaging in particular is often used for material characterizations such as identifying the crystal orientation[? ?] and edge states[? ?] in 2D materials, domain boundaries in nonlinear crystals[? ? ? ? ?] and poling quality of $LiNbO_3$[? ?], to name a few. Using nanostructures and especially metasurfaces from materials with second-order nonlinearity enables the integration of additional functionalities. Corresponding setups for applications need more and more complicated schemes. Nevertheless, SH imaging is still a valuable tool to characterize areas of interest, to analyze radiation directions and to understand the polarization dependencies of the process. All three activities are performed with the setup described in this chapter resulting in experiments reported in the next three chapters.

In this work, a self-built SH microscope setup in the reflection regime is used. The respective challenges are explained in this subsection, while the detailed realization of the setup is described in the following subsection. Two explicit solutions for special demands on the experimental results are dealt with in two additional sections, tackling the retardation compensation in Section 4.2 and the back-focal plane imaging in Section 4.3.

In principle, SH imaging of nanostructured surfaces is performed in a microscope. The sample is excited at the FH via a focused laser source and the generated SH is collected and detected. This scheme can be conducted in two general regimes: in transmission and in reflection. The essential question is whether the sample, especially the substrate below the nanostructures, is transparent for the FH and/or SH. For example, the GaAs substrate of the sample investigated in Chapter 5 could not transmit the FH or SH due to an unpolished back-surface.

In transmission, the FH is focused onto the sample and hits the nanostructures either

through the substrate or directly on the structured surface. For the latter, the SH has first to propagate through the substrate to be collected by a microscope objective, while the former can be collected directly from its source. Here the question of the influence of the substrate is important. The advantage of the transmission regime is the independence of the excitation by the FH and the collection/detection of the SH.

In the reflection regime, the microscope objective focusing the FH excitation is the same as the one collecting the generated SH. Both optical paths of FH and SH have to be joined by a beam splitter (BS) and/or separated again before the detector. The separation typically is a filter blocking the FH, but BSs like dichroic mirrors are similarly possible[?] .

To excite a single nanostructure or scan over a sample creating a SH map of high resolution, a tight focus is needed which comes with a high numerical aperture of the respective microscope objective. This is beneficial considering collecting as much SH signal as possible or for analyzing propagation directions. The disadvantage of a tightly focusing microscope objective is a small working distance and most detrimental a large chromatic aberration. Accordingly, the focal point at FH wavelength will be displaced with respect to the focal point at the SH wavelength.

Next to these essential requirements, additional features to control the FH power and polarization and to analyze the SH signal on polarization and radiation direction can be implemented. Especially optical elements being located in the shared beam path of SH and FH have certain constraints.

According to all these issues, several measures and compromises have to be taken into account to measure the SH in a way that relates to the actual SHG in the sample. The next subsection describes the setup realization and the advantages and disadvantages.

4.1.2. Realization of the second-harmonic microscope

The SH meaurements reported in the later chapters of this work are conducted in a self-built SH microscope using the reflection regime. The setup scheme is visualized in Fig. 4.1.

The FH is emitted by a wavelength tunable, pulsed laser ($\sim$100 fs, 80 MHz, MaiTai HP - SpectraPhysics). The central wavelength of the pulses can be tuned from 700 nm to 1040 nm with a power of maximally 3 W around 800 nm. The laser power arriving at the setup is controlled via the combination of a half-wave plate (HWP) and a linear

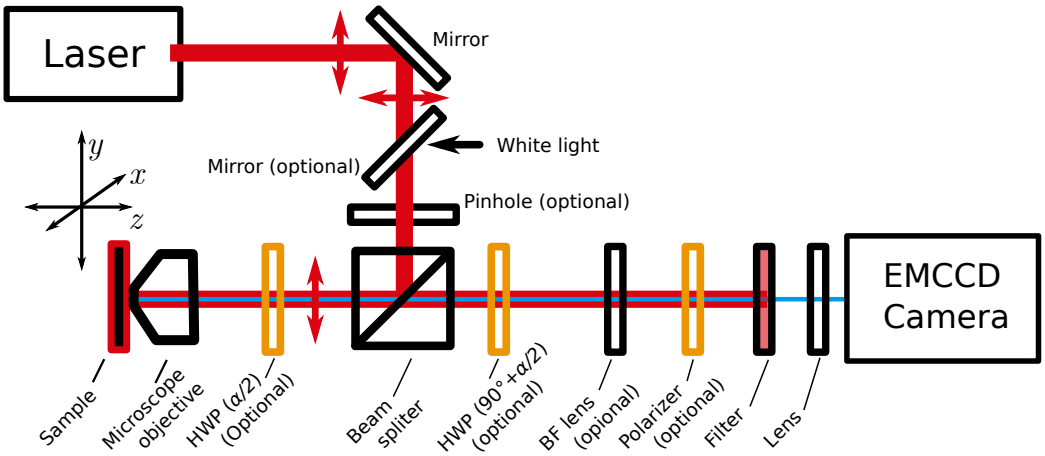

Figure 4.1.: Scheme of the SH microscope. The FH laser light and the generated SH light are depicted by the red and the blue lines, respectively.

polarizer. By rotating the HWP the part of the initial laser beam that is allowed to transmit through the linear polarizer can be chosen and thus controls the power. Another advantage is the clean linear polarization state of the FH with a high extinction ratio ($\sim$1:10000). It is chosen to be one of the two orthogonal polarization states TE parallel and TM perpendicular to the optical table.

The FH laser beam is routed to the sample via the reflected portion of a non-polarizing BS (BS025 - Thorlabs). This particular BS with its 90:10 ratio on transmission:reflection in the wavelength range of 400-700 nm is chosen to limit the loss of SH by transmission toward the detector. To be able to correctly characterize the polarization state of the SH the BS has to be non-polarizing. In the FH range however, this BS exhibits a ratio of around 65:35 at 820 nm and changes moderately varying the wavelength. Additionally, it is different for the two orthogonal polarization states TE and TM.

A HWP is used to change the linear polarization direction of the FH. This feature is useful to analyze the behavior of the SH depending on different FH excitation polarizations. There are two possible positions for this HWP. One is before the BS to avoid the retardation of the SH having to pass this optical element. The other position is after the BS directly in front of the focusing microscope objective. The latter is used for the measurements reported in this work. The reason is the reflection in the BS which adds different phases to TE and TM polarized light resulting in an elliptical polarization state when penetrated by a superposition of both (see Section 4.2.1).

The choice of placing the HWP, which is an arbitrary retarder for light in the SH wavelength range, directly in front of the microscope objective leads to a retardation of the collected SH propagating through it. This change of the SH polarization state has to

be compensated to characterize the actual polarization state from the generated SH. The needed procedure is described in the next Section 4.2.

The split portion of the FH laser beam reflected by the BS and altered by the polarization-controlling HWP is focused on the sample via a strongly focusing microscope objective (100x, Zeiss) with a high numerical aperture (NA). In the earlier experiments the NA was 0.75. This microscope objective was later replaced by an even higher NA-objective (again 100x, Zeiss) with NA=0.85. The high NA is mainly chosen to collect as much SH as possible, but it also leads to a stronger focus of the FH with higher angles and smaller focal spot. The smaller spot can be used for highly resolved SH intensity maps of the structured surfaces by scanning over the sample. But since the near field response of nanostructures and metasurfaces is often sensitive to oblique incidence excitation, the higher angle fractions might cause unwanted effects.

Since the focal lengths of the microscope objective for the FH and the SH are different, the aligned distance to the sample is chosen to use a compromise between a small excitation spot and a high collection efficiency for the SH. Since SH signals are usually small, the main goal is a strong SH by an as small as possible FH focus. When imaging the SH is important, a sample position close to the SH focal spot is necessary to have less blur in the SH image. This corresponds to a slightly bigger excitation spot. The smallest possible FH excitation spot in this setup has a FWHM diameter of 0.50 ± 0.05 μm at the wavelength of 820 nm. But typically the smallest used diameters corresponds to a FWHM diameter of 0.8 μm to 1.0 μm depending on the aim for higher SH signal or sharper SH image.

To increase the excitation spot of the FH on the sample, e.g. to excite a larger area of a metasurface for collective effects in periodic arrangements, a pinhole is placed in the FH laser beam path before the BS. It reduces the beam diameter. The smaller beam underfills the aperture of the microscope objective and thus exhibits a lower effective NA which results in a less focused spot on the sample. This can be necessary to excite several structures in periodic systems, but also to excite with a more planar wave since the focusing angle is reduced.

The FH signal reflected from the sample and collected from the microscope objective as well as the FH signal reflected from the BS surfaces and guided toward the camera are blocked via two shortpass filters (FESH500 and FESH550 - Thorlabs). Since the conversion efficiency of the SHG is typically very low and strong excitation as well as long

exposure times are necessary to detect the SH signal, the FH has to be blocked with two filters each damping 5 orders of magnitude. The accompanied damping of the SH in the order of 5% is inevitable but acceptable to secure that the measured intensity is resulting from the wanted SH.

The collected SH light is transmitted through the BS and other optional optical elements as well as the filters and finally detected by an electron-multiplying charge coupled device (EMCCD) camera (Andor). The SH light is focused on the camera sensor via an achromatic lens to view the FH and the SH if necessary, without changing the lens position. The sensor has 1000×1000 pixels. The quantum efficiency is 60% at 400 nm and increasing with higher wavelength. Lower wavelengths show notably less response on the sensor. With this, third harmonic signals from the sample are already blocked/damped by the camera itself.

The sample is mounted on a stable and precise 3-axis linear stage referring to the optical axis and the two orthogonal axes parallel and perpendicular to the optical table of the setup. The stage (VP-25XL, Newport) is motorized and controlled via the computer (using XPS-D controller - Newport). Automatic scans can be realized to measure SH intensity maps. Additionally, the sample is mounted on a tilt stage to ensure normal incidence of the FH. Any tilt or wedge of the sample itself or during the mounting can be compensated to assure the optical axis of the FH beam to be perpendicular to the plane of the nanostructures/meatsurface/2D material.

An additional feature of our setup is the back-focal plane imaging via an optional lens in the detection path. It provides the angular distribution of the generated SH by imaging the back-focal plane of the microscope objective onto the EMCCD camera, delivering the Fourier transform of the spatial distribution. The idea and realization are described in the Section 4.3.

To allow sample alignment an additional white light source can be included into the setup by a flipping mirror. A halogen lamp is used and introduced into the setup in front of the BS. Its reflection from the sample detected by the EMCCD camera helps to find the areas of interest.

The EMCCD camera and the 3-axis stage of the sample are connected via a self-programmed LabView-interface enabling automatic measurements. Additionally, rotation stages for HWPs, other retarders or polarizers can be included. Measurement schemes like intensity maps or polarization scans are possible and presented in the reported projects in the following chapters of this work.

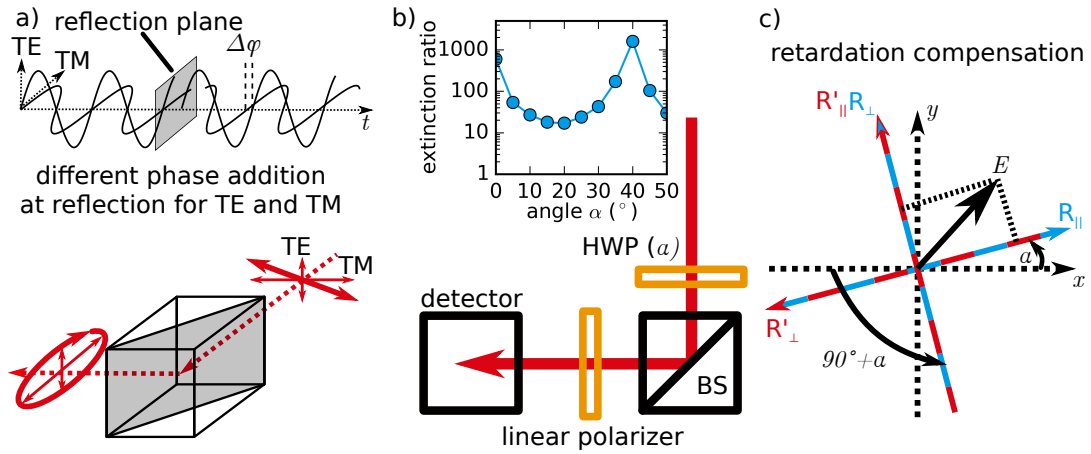

Figure 4.2.: a) Sketch of how linearly polarized light reflected in a BS can become elliptically polarized due to different phase addition for TE- and TM-polarized components. b) Extinction ratio plotted in logarithmic scale versus the HWP rotation angle. Added is a sketch of the measurement arrangement consisting of the HWP, the BS and the linear polarizer. c) Sketch of retardation compensation: retardance η added on the slow axis $\perp$ of retarder R compensated by retarder R' whose slow $\perp$-axis is rotated by 90°.

4.2. Retardation compensation in polarization sensitive measurements

4.2.1. Ellipticity due to reflection

In nonlinear nano-optics, the polarization of the excitation and of the resulting signal is of importance since the nonlinear response depends on the nonlinear susceptibilities which are multi-dimensional tensors coupling the vector components, i.e. the polarization, of the generated light to those of the exciting light. Usually, a rather complicated mix generates the different harmonics as described in the previous chapter.

For this work's purposes, typically linearly polarized light is used as FH excitation of nanostructures and 2D materials. To control the direction of this linear polarization, a HWP is used. By rotating the optical axis of the HWP to an angle α with respect to the incoming polarization direction, the polarization direction is changed by $2\,\alpha$.

This procedure is widely used in many microscope setups, but in the reflection regime it creates problems. Reflection regime setups use a BS to combine the excitation path with the detection path. Usual mirrors, whether plasmonic or dielectric, add different phases to the two orthogonal polarizations TE and TM. Therefore, every excitation of light which consists of a superposition of these two linear polarization states before the reflection becomes elliptical afterwards. Accordingly it loses its linear polarization. As depicted in Fig. 4.2(a), both components, TE and TM, oscillate in phase to be combined

to a linear polarization. The reflection adds different phases to both oscillations, ϕ_{TE} and ϕ_{TM}. Accordingly, a phase difference of $\Delta\phi = \phi_{\mathrm{TE}} - \phi_{\mathrm{TM}}$ appears in their oscillation resulting in an elliptical polarization.

This ellipticity can be measured. When sending linearly polarized light through a linear polarizer and detecting the transmitted signal, a maximum and a minimum intensity can be observed while rotating the polarizer. The ratio between the maximum and the minimum is called extinction ratio. For linearly polarized light the theoretical extinction ratio is infinite, but due to experimental imperfections, the real value is finite but high. In this work's setup, it was possible to measure values higher than 1000. Probably, the value is higher, but the noise and error of the detector could not be eliminated enough. Elliptically polarized light shows much lower extinction ratio values, depending on the degree of ellipticity. The limiting value is 1, where the state of circularly polarized light is reached.

In Fig. 4.2(b), the characterization of reflected light from the BS is shown. The HWP before the BS transforms the linearly polarized TE state into a still linearly polarized superposition of TE and TM. The BS reflects the light which is analyzed by a rotatable linear polarizer. Finally the transmitted light is detected. The plotted data represents the extinction ratio in logarithmic scale depending on the angle α as the angle between the fast axis of the HWP and the TE polarization direction. As can be seen in the plot, the extinction ratio drops to almost 10 over the range from 0 to 45°. Without the BS, the extinction ratio constantly stays over 1000 for the same range of angles. Thus the BS introduces ellipticity for incoming light of a superposition of TE and TM.

To overcome this ellipticity problem, the position of the polarization-changing HWP is changed from before the BS to a location between BS and sample. The incoming light hits the BS with one of the two orthogonal polarizations TE or TM which does not change after the BS reflection. Just afterwards, the polarization state is transformed by the HWP into any other linear polarization which eventually hits the sample.

The resulting disadvantage in the reflection regime is that the SH has to go through the same HWP and collects a retardation which changes its polarization state. Fortunately, the additional retardance can be experimentally compensated. Numerical compensation requires the knowledge about the retardance of the SH by the HWP. Usually the HWP is only characterized in the range of being a HWP, which is typically chosen to be around the FH wavelength to control its polarization. For the experimental compensation the actual retardance is not necessary to know.

The compensation can be done with another HWP which has to be identical to the first HWP. The phase change then can be introduced with the different sign by using it at the angle $\alpha + 90°$ with respect to the initially incoming FH polarization and α the corresponding angle for the first HWP. Fig. 4.2(c) illustrates an electric field E in the x, y-coordinate system. The first retarder R has its fast axis ($\|$) rotated by α with respect to the x-axis. The component of E on the slow axis ($\perp$) of retarder R (at $90° + \alpha$) exhibits the retardance η. To compensate for this retardance, a second retarder R' is positioned with the fast axis at $90° + \alpha$ with respect to the x-axis. The retardance η is then set on the up to now not yet retarded component which results in a neutralization of both retardances, since both components of E exhibit the same.

The analytical proof of this retardance is shown in the following subsection.

4.2.2. Arbitrary retarder

For this theoretical proof, Jones formalism is used with E_{0x} and E_{0y} as the incident electric fields in x- and y-polarization, and z being the propagation direction. Then any propagation through any medium/geometry can be described via an ABCD-matrix as follows:

$$\begin{pmatrix} E_x \\ E_y \end{pmatrix} = \begin{pmatrix} A & B \\ C & D \end{pmatrix} \begin{pmatrix} E_{0x} \\ E_{0y} \end{pmatrix} \ . \tag{4.1}$$

The arbitrary phase retarder in this formalism has the following appearance:

$$\begin{pmatrix} e^{i\eta/2}\cos^2(\alpha) + e^{-i\eta/2}\sin^2(\alpha) & (e^{i\eta/2} - e^{-i\eta/2})e^{-i\phi}cos(\alpha)\sin(\alpha) \\ (e^{i\eta/2} - e^{-i\eta/2})e^{i\phi}cos(\alpha)\sin(\alpha) & e^{i\eta/2}\sin^2(\alpha) + e^{-i\eta/2}\cos^2(\alpha) \end{pmatrix} \ , \tag{4.2}$$

where η is the retardance, α is the angle to the fast axis from the x-axis, and ϕ is the circularity. $\phi = 0$ for linear retarders, $\phi = \pm\pi/2$ for circular retarders. All other values between $\pm\pi/2$ are associated with elliptical retarders.

Considering a system of two arbitrary but equal retarders with the two different angles α and α' corresponding to the angle between the fast axis and the x-axis, two similar matrices are obtained, which here are called $M = \left(\begin{smallmatrix} A & B \\ C & D \end{smallmatrix}\right)$ and $M' = \left(\begin{smallmatrix} A' & B' \\ C' & D' \end{smallmatrix}\right)$.

The coupled system of both results in the final matrix $M_{\text{final}} = \left(\begin{smallmatrix} a & b \\ c & d \end{smallmatrix}\right) = \left(\begin{smallmatrix} AA'+BC' & AB'+BD' \\ CA'+DC' & CB'+DD' \end{smallmatrix}\right)$.

To realize compensation, the matrix M_{final} has to be a unity matrix of shape $\left(\begin{smallmatrix} 1 & 0 \\ 0 & 1 \end{smallmatrix}\right)$. Accordingly, the solution for α' depending on α has to fulfill $a = 1$, $b = 0$, $c = 0$ and $d = 1$.

The detailed calculations are spared here, but can be found in the appendix. To realize $b = 0$ and $c = 0$, it follows:

$$\begin{aligned} 0 &= (\cos^2(\alpha)\cos(\alpha')\sin(\alpha') + \cos(\alpha)\sin(\alpha)\sin^2(\alpha')) \ , \\ 0 &= (\sin^2(\alpha)\cos(\alpha')\sin(\alpha') + \cos(\alpha)\sin(\alpha)\cos^2(\alpha')) \ . \end{aligned} \tag{4.3}$$

Since these equations have to hold for any α, the solution can only be made by chosing α' such that $\alpha' = \alpha \pm 90°$. With this solution, also $a = AD - BC = d$. So, the final matrix is $M_{\text{final}} = a \cdot \left(\begin{smallmatrix} 1 & 0 \\ 0 & 1 \end{smallmatrix}\right)$, where a actually is 1.

Of course, actual retarders do have a certain amount of loss. But this only effects the overall transmission value $a = d < 1$, not the polarization state. A potentially larger influence is the BS which sits between the two HWPs in the here described setup.

The before made solution considers the transmission of the BS, which the SH light has to transmit in the setup arrangement, as perfect. Unfortunately, even non-polarizing BSs have slightly different transmission coefficients for the two orthogonal linear polarization states TE and TM. In the following derivation, the transmission of the BS in x is considered to be 1 and in y 1-ϵ.

Considering a system of two arbitrary but equal retarders with different angles of α and α' corresponding to the angle between the fast axis and the x-axis as in the ideal case before. Additionally, the BS has to be included with its matrix $M_{\text{BS}} = \left(\begin{smallmatrix} 1 & 0 \\ 0 & 1-\epsilon \end{smallmatrix}\right)$. The coupled system of retarder 1, then BS and retarder 2 results in the final matrix

$$M_{\text{final}} = \begin{pmatrix} a & b \\ c & d \end{pmatrix} = \begin{pmatrix} AA' + (1-\epsilon)BC' & AB' + (1-\epsilon)BD' \\ CA' + (1-\epsilon)DC' & CB' + (1-\epsilon)DD' \end{pmatrix} \ . \tag{4.4}$$

After lengthy calculation, which can be found in the appendix, using the solution from the ideal case $\alpha' = \alpha \pm 90°$, the transmission values a and d result in

$$\begin{aligned} a &= 1 + \epsilon \ \sin^2(\eta/2)\sin^2(2\alpha) \ , \\ d &= 1 - \epsilon \left(1 - \sin^2(\eta/2)\sin^2(2\alpha)\right) \ . \end{aligned} \tag{4.5}$$

These results show that the original transmission of the BS of 1 and 1-ϵ is slightly changed depending on the retardance η and the angle α, but just by maximally the value of ϵ.

The additional terms for the off-diagonal elements b and c are non-vanishing due to the

inclusion of ϵ:

$$\begin{aligned} b &= -\epsilon \ (e^{i\eta/2} - e^{-i\eta/2}) \cos(\alpha) \sin(\alpha) (e^{i\eta/2} \sin^2(\alpha') + e^{-i\eta/2} \cos^2(\alpha')) \\ &= -\epsilon \ \left(\left[e^{i\eta} - 1 \right] \cos^3(\alpha) \sin(\alpha) + \left[1 - e^{-i\eta} \right] \sin^3(\alpha) \cos(\alpha) \right) \ , \\ c &= -\epsilon \ (e^{i\eta/2} - e^{-i\eta/2}) \cos(\alpha') \sin(\alpha') (e^{i\eta/2} \sin^2(\alpha) + e^{-i\eta/2} \cos^2(\alpha)) \\ &= -\epsilon \ \left(\left[e^{i\eta} - 1 \right] \sin^3(\alpha) \cos(\alpha) + \left[1 - e^{-i\eta} \right] \cos^3(\alpha) \sin(\alpha) \right) \ . \end{aligned} \tag{4.6}$$

Both values b and c are complex and have an absolute value in the range of ϵ.
In the setup used for this work, the used BS BS025 from Thorlabs has an $\epsilon < 0.03$ in the investigated SH wavelength range from 400 to 500 nm. This maximal value around 0.03 is reached only at the edge of the non-polarizing range of this BS at 400 nm. Which concludes an error of the transmitted polarization state through the HWP-BS-HWP arrangement as less or equal to 3%.

4.3. Back-focal plane imaging

4.3.1. Projecting the angular spectrum

In nano optics, not only the spatial information about where light is generated is interesting, but also in which direction the light is radiated. Especially in the case of sub-wavelength structures, spatial information is not possible to be resolved and thus the angular spectrum of the emitted light becomes more attractive. A suitable method that can be implemented into a free space microscope as used for this work's experiments is back-focal plane imaging, which - as the name says - is projecting the back-focal plane of the collecting microscope with an additional lens onto a detecting plane, here onto the EMCCD camera.

Considering a simple lens with the focal length f, the spatial distribution of light in one focal plane is transformed into a field distribution in the other, so-called back-focal plane (BFP), which is a spatial representation of the angular distribution in the first focal plane. This arrangement is usually called a 2-f-setup and can be seen as an experimental Fourier transform of the spatial distribution into an angular distribution and vice versa.

In a microscope setup, the microscope objective itself works as the lens and provides the angularly resolved distribution as a spatial distribution in its BFP. Although it is typically constructed of different lenses, it still works as an experimental Fourier transform.

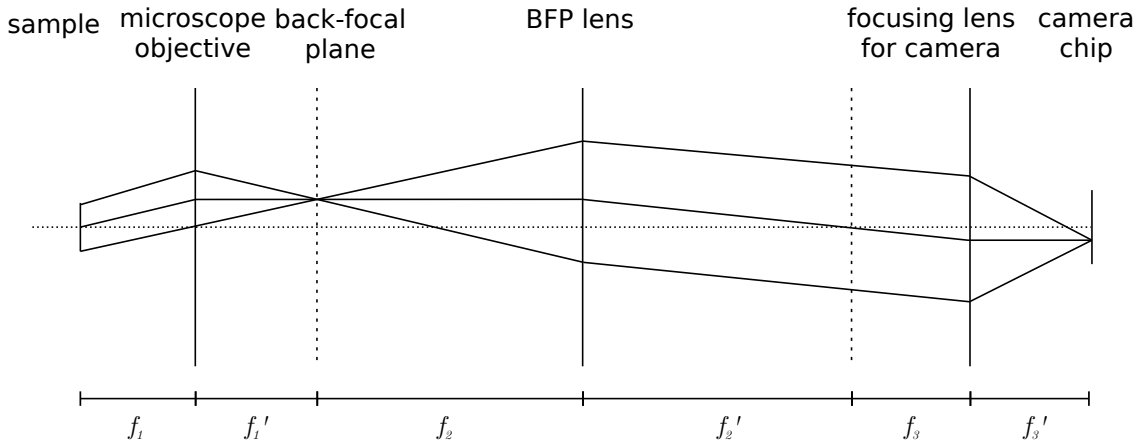

Figure 4.3.: Scheme of BFP imaging in a microscope.

However, instead of retransforming it toward the detection plane to observe the spatial distribution again, an additional lens to project the BFP of the objective onto the detection plane is used. The distance between the microscope objective and the additional lens as well as to the detector is crucial.

Fig. 4.3 shows the optical path from sample to camera sensor for three rays with the same emission direction. The first lens represents the microscope objective, which typically is an ensemble of lenses but can be described effectively by one lens, here with the focal length f_1 and the back-focal length f_1'. In the BFP, all three rays meet in one point. This BFP is projected on the camera chip by placing the BFP lens and the camera-focus lens in the optical path such that the distance between two consecutive lenses is the addition of their focal lengths.

4.3.2. Integration into the second-harmonic microscope setup

In the setup described here, the additional, optional lens to project the BFP onto the EMCCD camera is placed between the BS and the lens to focus the image onto the camera sensor. The lens is hereby called BFP lens. Using the microscope objective, the BFP lens and the focusing lens in front of the camera, a 6-f-setup is realized, meaning to place each lens so as to fit the distance in between as long as the addition of the two neighboring focal lengths. Like this, a system of three optical Fourier transforms is implemented in which the second one is a back transform.

It is necessary to choose a long focal length for the BFP lens to provide space for optical elements like the BS, HWPs, filters or analyzing polarizers. Typically, the BFP of the microscope objective is found close to the housing of the objective, sometimes even within.

In this work's setup, a large diameter lens with a 20 cm focal length was chosen as the BFP lens to fit the BS and two rotation stages with the HWPs for the FH polarization dependence and retardation compensation in between.

The alignment procedure includes two major steps. First, the distance between focusing lens and BFP lens has to be found. Then this two-lens-system has to be shifted with respect to the microscope objective to find the BFP projection. Since manufacturer values are usually bound to a wavelength which is not used in the actual setup, this procedure has to be performed experimentally and can be tedious.

BFP imaging of the SH signal generated in metasurfaces is used in the next three chapters reporting on experiments dealing with SH diffraction on an intrinsic nonlinear metasurface made from GaAs in Chapter 5, SH diffraction including a nonlinear hologram creating vortex beams from a patterned MoS_2 monolayer in Chapter 6 and SHG in a hybrid system build of a linear Si metasurface covered by the nonlinear MoS_2 monolayer in Chapter 7.

5. Second-harmonic diffraction from a GaAs metasurface

5.1. Resonances at the fundamental harmonic

The realization of nonlinear metasurfaces especially for second-order nonlinear processes is still a challenge. On the way to applications like on-chip integration, large area surface functionality and entangled photon sources, the field is still facing issues like low conversion efficiency in wave mixing processes, scalable platforms for easy-integratable fabrication and avoiding damage threshold problems as in heat-sensitive plasmonic materials. Using dielectric materials showed success on the latter, still the choice among dielectric nonlinear materials and schemes is large.

In this work, three different systems are investigated taking different opportunities. The first system, investigated in this chapter, consists of a metasurface made from a well-known material with intrinsic, but still difficult to use second-order nonlinear susceptibility. In the next chapter, a second system is discussed structuring a recently found 2D material with intrinsic second-order nonlinearity, which replaces the user-unfriendly $\hat{\chi}^{(2)}$, but lacks conversion efficiency due to its ultrathin interaction volume. In Chapter 7, a hybrid system is introduced using the 2D material as the second-order nonlinear material supported by a scalable linear metasurface which allows for designing resonant field enhancement to boost the SHG.

Gallium arsenide (GaAs) as a material with an intrinsic and strong second-order nonlinear susceptibility is a promising candidate to realize a nonlinear photonic metasurface. The structuring of GaAs is relatively advanced considering its usage in (opto-) electronics. The group around Igal Brener from Sandia National Laboratories, USA, already realized a GaAs metasurface observing SHG[?] . They also designed and fabricated the sample investigated in this chapter.

Structuring GaAs thin films has two purposes. On one hand, the structures are supposed to support Mie-type resonances to enhance and create special FH fields, which will be discussed in the first section of this chapter. On the other hand, the periodic arrange-

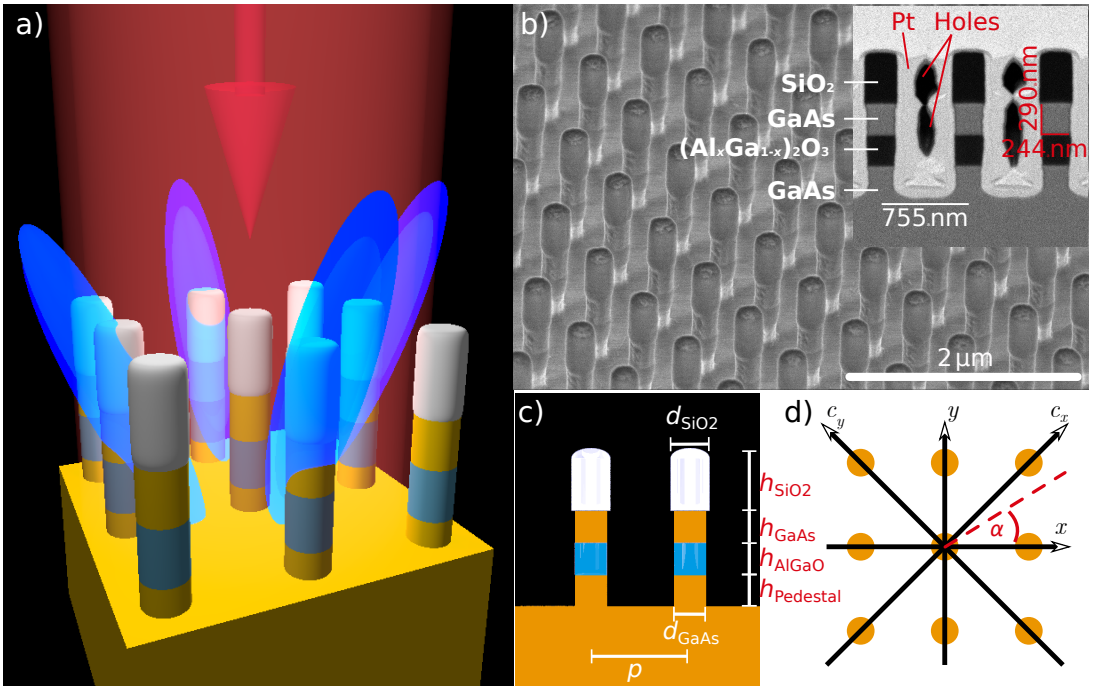

Figure 5.1.: a) 3D sketch of SHG in the GaAs metasurface. b) SEM image of sample under oblique incidence. Inset showing FIB cut to show the pillar composition. c) 2D sketch side view. d) 2D sketch top view showing crystal axes.

ment leads to diffraction of the generated SH which is supposed to enable SH emission out of the surface plane. The latter is depicted in Fig. 5.1(a). The SH response including the SH diffraction are described and further discussed in the next section.

The experiment presented in this chapter has been published by the author of this thesis and collaborators[?] . The experiment and the result analysis including numerics were performed by the author. Experimental assistance was provided by Anna Fedotova (Nano & Quantum Optics group at the Institute of Applied Physics from the Friedrich Schiller University, Jena).

As explained in Section 2.2, nonlinear materials typically have low nonlinear susceptibility values. This results in low conversion efficiencies for nonlinear frequency generation processes. To use nonlinear frequency conversions in applications, the conversion efficiency has to be increased. This could be realized by expanding the interaction length or volume as it is done in waveguides. However, this might not fit into compact systems and more relevant, it requires difficult phase-matching engineering.

Another way is to increase the initial excitation field. Instead of pumping with more and more power, which would not be desirable in terms of energy consumption, other

ways of increasing the output have to be found. The advantage of nanostructures on this behalf is the creation of field enhancement based on resonances in the frequency ranges of participating fields. In second-harmonic generation (SHG), as it is dealt with in this work, resonances at the fundamental harmonic (FH) and at the second harmonic (SH) wavelength come into consideration.

A resonance of the nanostructures at the SH wavelength can enhance the SH output. The essential requirement, which is typically difficult to achieve, is a strong overlap between the FH induced second-order nonlinear polarization and the field distribution of the resonant mode at the SH wavelength. If this overlap is large, the resonant mode can be excited by the nonlinear polarization at the SH wavelength and due to the resonance itself, i.e. a longer lifetime of the light inside the confinement, it can build up a larger SH field. Typically, such a resonance is designed to couple to the far field, which leads to an enhanced SH response in comparison to the case without the resonance at the SH wavelength. However, the SH response depends only linearly on the field enhancement of such a resonance.

In contrast, a resonance at the FH wavelength provides a nonlinear boost in nonlinear frequency generation processes, due to the multiple participation of the FH field in the generation of the nonlinear polarization. In SHG the FH field engages two times in the product of the nonlinear polarization and thus in the electric field at the SH frequency. If the FH resonance triples the strength of the FH field, the SH field is in principle increased by a factor of 9.

To realize resonances at both FH and SH wavelength is of course desirable. However, the design of simultaneously matching FH and SH resonances is very difficult in most systems and even impossible in some cases. Accordingly, it is practicably favorable to focus on a resonance at the FH, as it is done here.

The investigated sample, a metasurface consisting of a two-dimensional periodic rectangular grid of GaAs disks optically isolated from the GaAs substrate by an AlGaO layer, is fabricated following the scheme presented in Section 3.2.3. A scanning-electron microscopy (SEM) image of the sample is shown in Fig. 5.1(b). The inset represents a FIB cut performed by Michael Steinert (Nano & Quantum Optics, Institute of Applied Physics, Friedrich Schiller University Jena) through the disks revealing the different layers in each pillar. Additionally to the GaAs disks and the optically isolating oxide, a SiO_2 cap and a GaAs pedestal appear due to over-etching. The measured sizes as depicted in the sketch of Fig. 5.1(c) are $d_{\mathrm{GaAs}} = d_{\mathrm{AlGaO}} = d_{\mathrm{pedestal}} = 244\,\mathrm{nm}$, $h_{\mathrm{GaAs}} = h_{\mathrm{pedestal}} = 290\,\mathrm{nm}$,

$h_{\mathrm{AlGaO}} = 280$ nm, $d_{\mathrm{SiO2}} = 296$ nm, and $h_{\mathrm{SiO2}} = 470$ nm. The period in both directions is measured to be $p = 755$ nm. The backside of the GaAs substrate was not polished, thus all measurements are done in reflection.

An essential property is the cut of the GaAs substrate, representing the crystal structure orientation of the substrate and all on-top grown thin films, including the GaAs disks. The cut was the typical (100)-direction, i.e. one of the crystal axes is perpendicular to the surface, the other two are in the surface plane. The orientation of the metasurface grid, however, is rotated by 45° to the crystal axes as sketched in Fig. 5.1(d). The reason for the rotation is the second-order nonlinear susceptibility tensor $\hat{\chi}^{(2)}$ as described in Eq. 3.8. The resulting nonlinear polarization following Eq. 3.9 goes to zero if the exciting FH field is linearly polarized in the direction of only one crystal axis. To avoid this situation, but exploit the periodicity along the rectangular grid axes, this grid was chosen to be rotated. The second-order nonlinear susceptibility rotates to

$$\hat{\chi}^{(2)} = \chi_0^{(2)} \left(\begin{pmatrix} 0 & 0 & -1 \\ 0 & 0 & 0 \\ -1 & 0 & 0 \end{pmatrix}, \begin{pmatrix} 0 & 0 & 0 \\ 0 & 0 & 1 \\ 0 & 1 & 0 \end{pmatrix}, \begin{pmatrix} -1 & 0 & 0 \\ 0 & 1 & 0 \\ 0 & 0 & 0 \end{pmatrix} \right) . \tag{5.1}$$

The resulting second-order nonlinear polarization reads as

$$\begin{aligned} P_x^{(2)} &\sim -2\chi_0^{(2)} E_z E_x \ , \\ P_y^{(2)} &\sim \ \ 2\chi_0^{(2)} E_z E_y \ , \\ P_z^{(2)} &\sim \chi_0^{(2)} (E_y^2 - E_x^2) \ . \end{aligned} \tag{5.2}$$

With this, an only x- or only y-polarized field can induce at least a z-component of the nonlinear polarization and thus generate a z-polarized SH field.

The design of the resonances had to follow the constraints of the setup and the material. The resonances were chosen to be in the near infrared above the band gap which is situated around 870 nm to avoid absorption at the FH. The other limit is the tunability of the pump laser which ends at 1040 nm emission wavelength.

The measured reflection spectra of the sample shown in Fig. 5.2(a) were obtained by using a Fourier transform infrared spectrometer (Bruker VERTEX 80v) combined with an infrared microscope (Hyperion 2000) differentiating the two polarizations $\alpha = 0°$ parallel

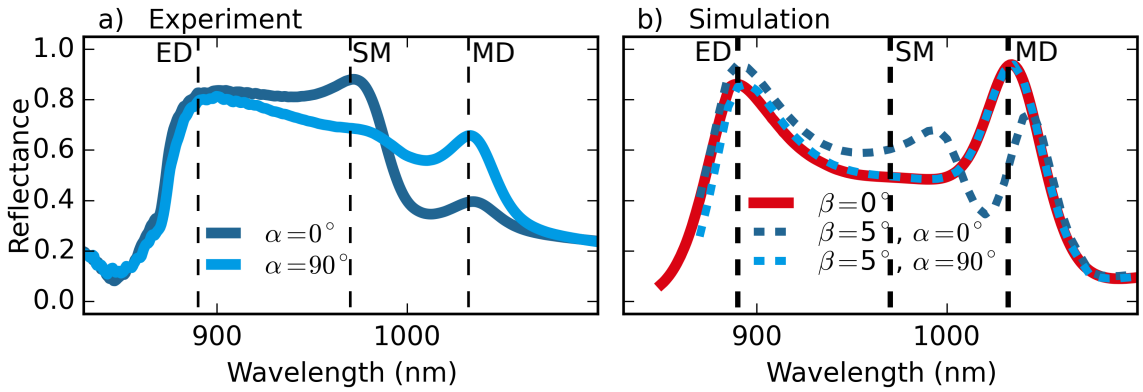

Figure 5.2.: (a) Measured linear reflectance. (b) Numerically simulated linear reflectance.

to the x-axis and $\alpha = 90°$ parallel to the y-axis with respect to α, x and y as shown in Fig. 5.1(d). Although the design was made for a symmetric metasurface, the reflection spectra of the two polarizations differ. This anisotropy might arise from slight asymmetry in the fabricated structure. Nevertheless, both spectra contain three resonances, which are hereby called ED for electric dipole at around 890 nm, MD for magnetic dipole at around 1030 nm and SM for 'symmetry-forbidden mode' at around 970 nm.

All numerical simulations throughout this thesis are performed by the author using the time-harmonic finite-element method solver from JCMwave[? ?] . Linear simulations use a monochromatic plane wave illumination, while nonlinear simulations use the field confined in the nonlinear material as calculated in the linear simulation at the FH wavelength. It is used to calculate the nonlinear polarization which then acts as the light source for the SH, which is possible to do in the undepleted pump approximation.

Modeling the metasurface, a unit cell of the stacked disks is considered with periodic boundary conditions. The geometrical parameters are taken as described above. As the material properties, literature values are used for the GaAs[?] and non-dispersive constant values of the refractive index as 1.60 for the oxide AlGaO[?] and 1.45 for the SiO_2 are chosen.

Fig. 5.2(b) shows the simulated spectra. Since the model consists of a symmetric unit cell, both x- and y polarization are identical. The spectrum confirms the ED and MD resonances from the experimental results. The SM resonance however does not appear. By shifting the angle of incidence β in x-direction by 5° with respect to normal incidence, the spectral dependence differs for the two polarizations revealing a third resonance. This approach emulates the experimental excitation with a finite NA. This third mode is symmetry-forbidden by excitation under normal-incidence and thus referred to as "symmetry-forbidden mode" (SM). Similar modes were previously reported in plas-

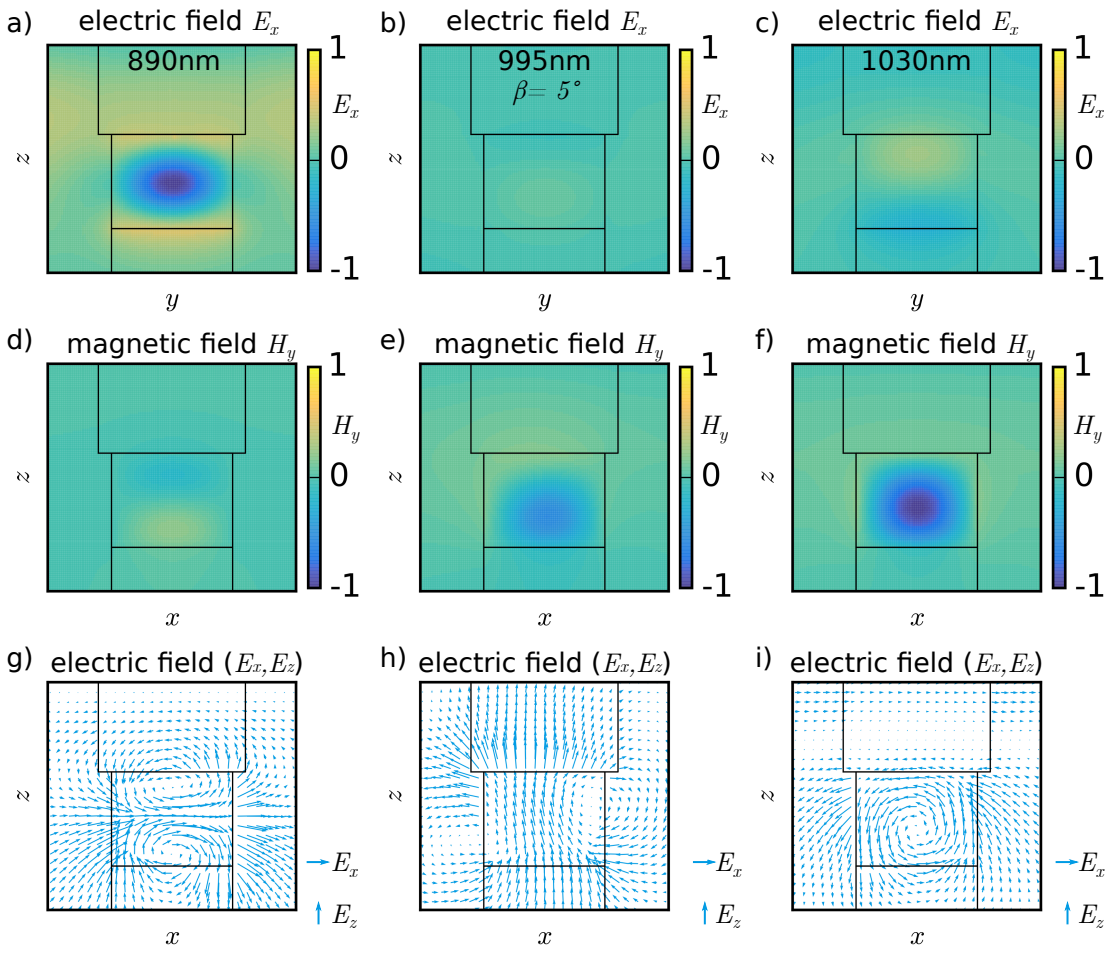

Figure 5.3.: Numerically simulated field distributions at the ED (a,d,g), SM (b,e,h) and MD (c,f,i) resonance, showing the x-component of the electric field (a-c), the y-component of the magnetic field (d-f), and the vector field consisting of the x- and z-component of the electric field (g-i).

monic[?] and dielectric structures[?] .

The respective simulated near-field distributions are presented in Figs. 5.3(a—i) showing only the cross section through the center of the isolated GaAs disk, which contains the strongest field. Fig. 5.3(a) provides the x-component of the electric field excited by an x-polarized plane wave at 890 nm and normalized to its maximum. It shows a strong spot in the center of the disk, which is characteristic for an electric dipole mode. The x-components of the two other resonances shown in Figs. 5.3(b,c) normalized to the maximum at the ED resonance, do not show significant values.

In contrast, Figs. 5.3(d-f) show the y-component of the magnetic field for the three resonances, this time normalized to the maximum value for the MD resonance. Fig. 5.3(f) shows a strong spot in the center of the disk for the magnetic field at 1030 nm, which confirms the dominating magnetic dipole mode. At the SM resonance in Fig. 5.3(e), a weaker spot is simulated while at the ED resonance in Fig. 5.3(d) an even weaker field

appears. For comparison, the vectorial plots in Figs. 5.3(g-i), representing the electric field components E_x and E_z in the x, z-plane through the center of the disk, confirm the different electric field distributions for the ED (Fig. 5.3(g)) and MD (Fig. 5.3(i)) resonance, where the latter shows a circling electric field which represents the magnetic dipole mode, and the former matches with the typical electric dipole distribution. The SM resonance shows a more complicated field distribution in Fig. 5.3(g) revealing its non-typical Mie-type mode. It might have contributions of different multipolar orders or even being connected to guided modes due to the tilted excitation.

These resonances in the wavelength range of the FH already separate this GaAs metasurface from an unstructured GaAs thin film. While the ED resonance shows a higher local field enhancement by plane wave illumination, the other two resonances provide electric fields with non-zero z-component which is interesting for the SHG considering the second-order nonlinear susceptibility tensor $\hat{\chi}^{(2)}$. While electric fields polarized only in x-and y-direction produce a nonlinear polarization in z-direction, a combination of electric fields containing z-components can also create SH light polarized in x- or y-direction, which is necessary for out-of plane radiation, but especially for radiation normal to the metasurface plane.

Note that additional spectra of linear-optical measurements and linear numerical simulations around the SH wavelengths were investigated, not shown here. The high absorption of GaAs in this spectral domain, however, does not support the formation of clear resonances.

Up to this point, the linear behavior of this GaAs metasurface is characterized. Three resonances at different wavelengths with different field distributions are found. Each of them leads to field enhancement inside the GaAs disks which is supposed to increase the induced nonlinear polarization which - in the best case - results in enhanced SHG. The next section deals with the observation of the SH and the respective diffraction.

5.2. Second-harmonic diffraction

The process of SHG in nanostructures and thus in a metasurface is not only dependent on the before mentioned exciting FH fields, but also on the second-oder nonlinear susceptibility described in Section 2.2 and the radiation properties of the locally generated

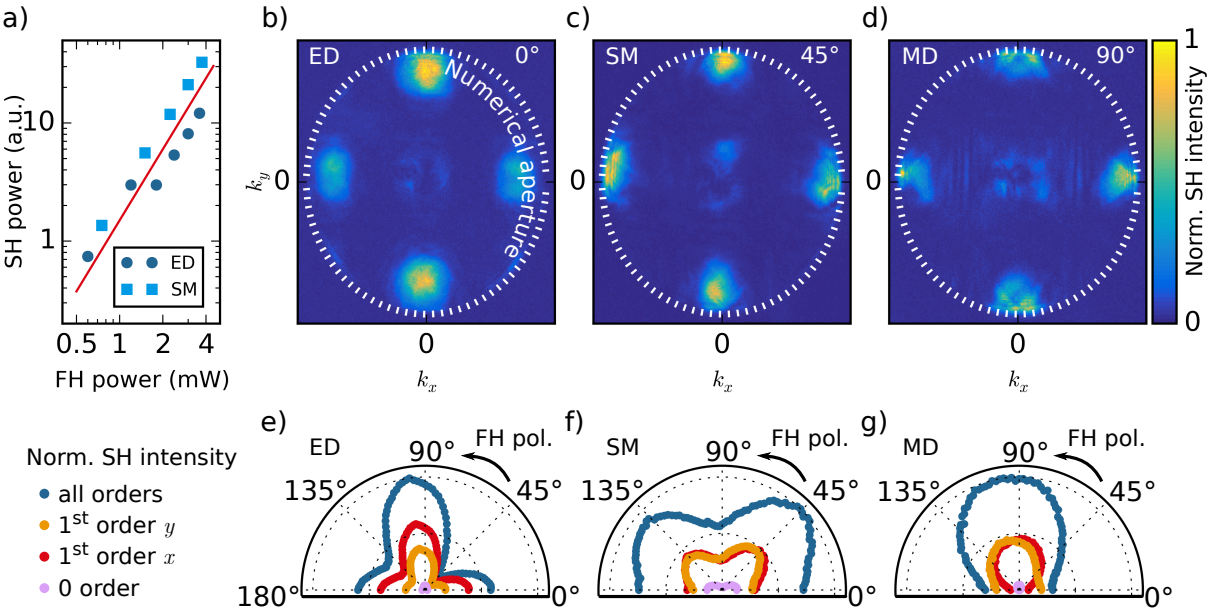

Figure 5.4.: (a) SH power dependent on FH power. (b)-(d) BFP images of the SH intensity at (b) the ED resonance and 0° FH polarization, (c) SM resonance at 45° and (d) MD resonance at 90°. (e)-(f) Measured SH intensity dependent on FH polarization at (e) the ED, (f) the SM and (g) the MD resonance.

SH field. Correspondingly, this section deals with the observed SH signals, in particular discussing the SH diffraction including SH radiation normal to the metasurface plane.

The SH response observed from the GaAs metasurface is indeed of second-order power dependence. In Fig. 5.4(a), the measured SH intensity versus the FH power is shown in a double-logarithmic plot presenting a linear behavior of the slope around 2, which is confirmed by the red line representing a quadratic function. This behavior is proof for a squared power dependence which matches with a SHG process.

Since SH emission normal to the surface under normal incidence FH excitation is forbidden, the observed SH signal has to come from larger emission angles. A useful visualization of this characteristic is BFP imaging, a special projection method described in Section 4.3. It shows the angular spectrum of the SH radiation, representing the different propagation angles of the SH emission and thus the diffraction orders resulting from SH diffraction as described in Section 2.3. The NA of 0.75, which is used in this experiment, is just large enough to collect the theoretically propagating diffraction orders, i.e. zero and first orders, in the SH wavelength range from 445 nm to 515 nm at the given period of 755 nm under normal incidence (compare with Eq. 2.14).

Fig. 5.4(b) shows the diffraction orders of the SH signal excited by an FH at the ED resonance with the FH polarization parallel to the x-axis, which represents the FH

polarization angle $\alpha = 0°$ following the coordinate system in Fig. 5.1(d). While the SH at zero order diffraction is very small, nearly vanishing, strong SH signals are observed at the first diffraction orders.

The vanishing signal at the zero diffraction order for the ED resonance is also observed from single AlGaAs nano-disks by Carletti *et al.*[??], showing that SH emission normal to the substrate plane is absent. This feature results from the symmetry of the nano-disks and the structure of the nonlinear susceptibility tensor $\hat{\chi}^{(2)}$ of AlGaAs, which is identical to that of GaAs. The FH excitation polarized in the x- or y-direction, enhances fields polarized along the two different in-plane crystal axes of GaAs (or AlGaAs), leading to SHG which is mostly polarized along the z-direction and thus does not propagate normal to the substrate plane.

The BFP images of the SH intensity excited at the two other resonances, SM and MD, are shown in Figs. 5.4(c) and (d). They provide a similar picture of a vanishing zero diffraction order and strong first diffraction orders. The latter are positioned closer to the limiting NA-circle shown in white due to their larger wavelengths. The respective FH excitation polarizations for the shown BFP images are chosen at the angles $\alpha = 45°$ and $\alpha = 90°$, respectively. This is due to the deviating FH polarization dependencies of the SH power with respect to the ED resonance.

In Fig. 5.4(e), the polar projection of the SH intensity of the ED resonance is shown depending on the FH polarization angle. Over the measured 180°, it shows 3 maxima of which two are equivalent, i.e. at 0° and at 180°, and two minima at polarization angles describing the excitation in the directions parallel to the GaAs crystal axes. This dependence follows nicely the characteristic of the $\hat{\chi}^{(2)}$-tensor and the resulting nonlinear polarization $\vec{P}^{(2)}$ shown in Eq. 3.9, since the electric field of the electric dipole inside the disk is oriented in the same direction as the excitation polarization.

In contrast, the electric field profiles of the SM and MD resonance show a more complicated mix of polarizations at different positions in the disk. This leads to different FH polarization dependencies of the SH, since the SH generated by the fields is differently supported or suppressed by the different field components than in the case of an ED resonance. Fig. 5.4(f) shows the opposite behavior for the SM resonance with respect to the ED resonance. The maxima are observed at the FH polarization parallel to the GaAs crystal axes. The MD resonance however shows only one maximum over the measured range of 180° at $\alpha = 90°$. This result does not match with the theoretically symmetric design of the metasurface. However, already the linear reflection measurements showed

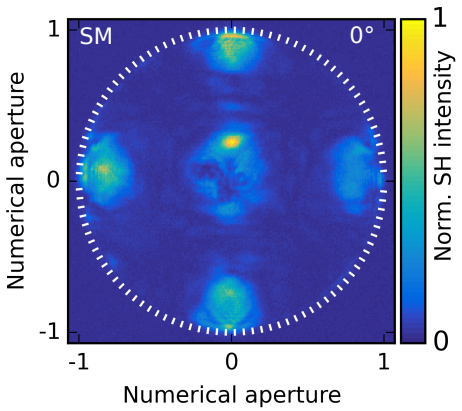

Figure 5.5.: BFP image of the SH intensity at the SM resonance and 0° FH polarization.

a deviation from the theoretical expectations. This might stem from slight tilts in the fabrication of the pillar structures, changing the symmetry and thus the support of the SHG at different FH polarizations.

Nevertheless, the z-components of the electric field distribution of the MD resonance shown in Fig. 5.3(i) did not support emission normal to the metasurface plane although they would create a local SH field polarized in x and y-direction. This might result from the fact that these z-polarized fields are directing in both positive and negative z-directions very close to each other. The radiation from the respectively generated x- and y-polarized SH fields might cancel each other out.

The experiments show clear SH emission out of the surface plane. A feature, unstructured GaAs thin films with the (100)-cut surface do not offer.

The reason for an observable SH signal propagating away from the metasurface's plane is a combination of diffraction and the specific field distribution of the Mie-type resonances leading to a specific field distribution of the nonlinear polarization. However, it seems that due to the structure of the second-order nonlinear susceptibility $\hat{\chi}^{(2)}$, only SH emission in the higher diffraction orders is possible, but not in the zero order, i.e. normal to the metasurface plane.

As explained in the Section 2.3, the diffraction orders are bound to an envelope described by the Fourier transform of the shape of the transmission window of one unit cell of the grating. This is the same here. The part of the SH field that is bound to the different diffraction orders depends on the Fourier transform of the field of the SHG generated in one unit-cell of the metasurface. If the SH field in the single nano-disk system vanishes in the direction normal to the disk plane, there can only be a vanishing zero diffraction order for the radiation of the whole metasurface.

However, a non-vanishing SH signal in the zero order is observed in our metasurface at excitation at the SM resonance with the FH polarization parallel to the x-axis, shown in the BFP image of Fig. 5.5. The stronger signal is not well shaped and was not expected, neither in the design nor in the numerical simulations. Similar to the appearance of the SM resonance, as it would be forbidden in the design, this observation might result from some artifacts in the fabricated structure due to the high-NA excitation. Numerical investigations into oblique incidence or oblique pillars could not confirm this observation. Nevertheless, it is also visible in the polarization dependence shown in Fig. 5.4(f). Another possibility might be slight deviations from the round disk shape. A similar system was investigated by Vabishchevich *et al*[?] , where they look at a rectangular bar which has an extension on one corner resulting in asymmetrically deranged field distributions for the resonances. This deviation might cause special nonlinear polarization distributions supporting SH emission normal to the surface. They do not show BFP-images, but they use a microscope objective with a NA of 0.26, which limits drastically the collection angle. Correspondingly, their observed SH signal is probably only consisting of the zero diffraction order where they observe a high enhancement.

A different idea to generate SH emission in the zero diffraction order is to use a different crystal cut, i.e. a different orientation of the crystal axes with respect to the surface[? ?] . Another approach is using a special modulation of the Mie-type resonances by diffraction in both FH and SH to observe close to zero order emission[?] .

The study reported here showed the possibility to form the generated SH field in GaAs to propagate outside of the surface plane of the nonlinear material despite its $\hat{\chi}^{(2)}$-tensor due to the appropriate nano-structuring of the surface. At the time of the publication it was the first time this behavior was proven for a second-order nonlinear metasurface of the GaAs material class. However, further investigations in this material system were not performed in the extend of this work.

Since the SH emission normal to the surface, which lack in this kind of GaAs metasurfaces, is a beneficial feature for future nonlinear metasurface applications, the next chapters deal with nanostructured surfaces using a recently found second-order nonlinear material. TMD monolayers attracted the attention of using its second-order nonlinearity with a promising $\hat{\chi}^{(2)}$-tensor for normal to the surface SH emission. As shown in Eq. 3.2 in Section 3.1.2, SH fields polarized in x- and y-direction can be generated in the two-dimensional MoS_2 monolayer, as all the other TMD monolayers, by normal incidence FH

excitation which leads to SH emission in z-direction, i.e. normal to the monolayer plane. By patterning it as reported in the next Chapter 6 and hybridizing it with a linear multi-resonant Si metasurface as reported in Chapter 7, a possibly easier access for second-order nonlinear metasurfaces in applications is investigated.

6. Second-harmonic diffraction from patterned MoS_2 monolayer

6.1. MoS_2 monolayer grating

Newly found intrinsically second-order nonlinear materials are two-dimensional (2D) transition metal dichalcogenide (TMD) monolayers. These materials have a second-order nonlinear susceptibility $\hat{\chi}^{(2)}$ tensor structure which enables normal SH emission at normal incidence FH excitation due to their in-plane components (see Section 3.1.2). This provides an advantage with respect to GaAs to be used in second-order nonlinear metasurfaces. Additionally, the fabrication process via exfoliation or nowadays high-quality CVD growth might be another advantage over GaAs and $LiNbO_3$ thin-films and structures. It is even possible to transfer these monolayers on top of nearly any substrate, which enables second-order nonlinear surfaces wherever it might be needed.

To use 2D materials in nonlinear photonic applications, some issues have to be investigated next to fabrication and transfer: Can additional functionality be created next to the SHG by spatial manipulation of these monolayers? Can this functionality be exploited without sacrificing conversion efficiency? How can the SH signal be enhanced without reaching the material's damage threshold, i.e. enhancement of the conversion efficiency?

In a first attempt to answer these questions, this chapter deals with patterned MoS_2 monolayers enabling SH diffraction as a supplemental functionality. Additionally, to shed light on the SH enhancement possibilities, the next chapter discusses hybrid systems, reporting on multi-resonant Si metasurfaces covered by MoS_2 monolayers.

The content of this chapter was published before in[?] by this work's author and collaborators as well as on conferences beforehand[? ?]. At the same time, Dasgupta *et al*[?] published their similar work on patterned WS_2 monolayers instead of MoS_2 monolayers.

In the first section of this chapter, the patterned MoS_2 monolayer is described, in particular the removal of material to create a grating, and its quality. The observed SH signal, concentrating on the SH diffraction, is discussed in the second section. The last section in this chapter deals with a more elaborate structure, a fork-like grating including a topological dislocation generating a SH vortex beam in the first diffraction order.

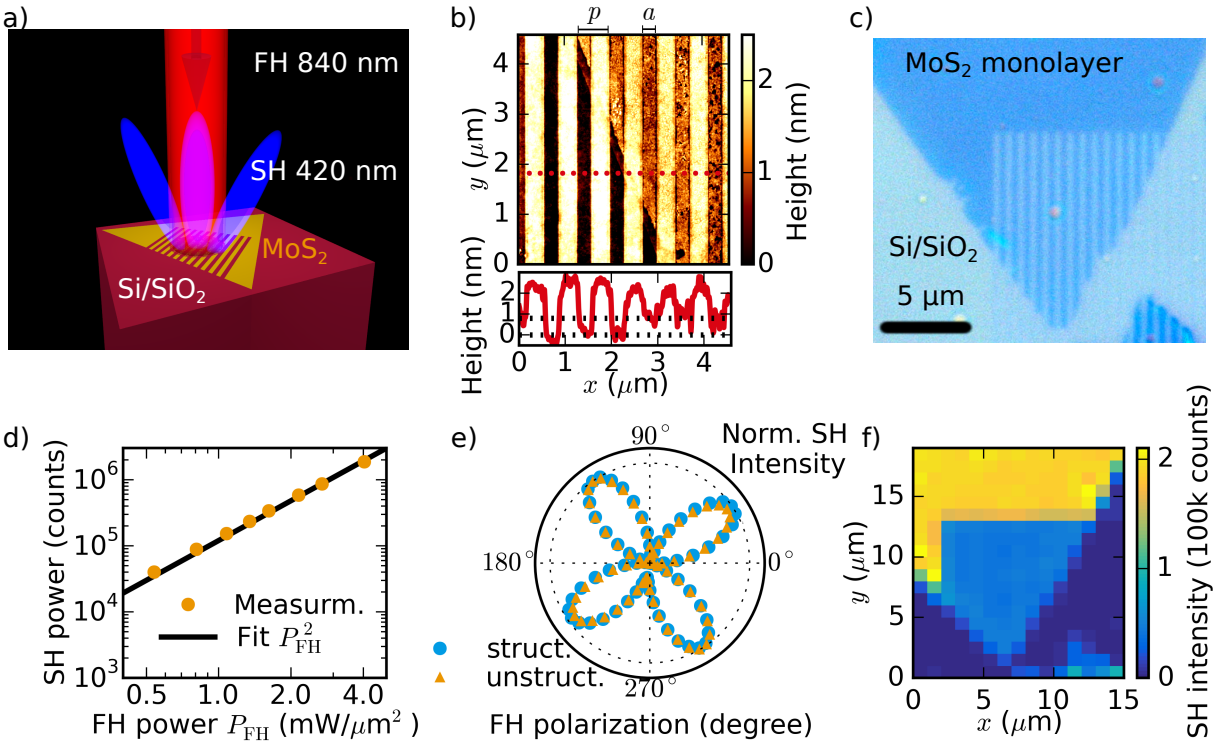

Figure 6.1.: a) 3D sketch of SH diffraction in patterned MoS_2 monolayer. b) AFM image of the grating patterned into the MoS_2 monolayer. c) Optical microscope image of the grating patterned into the MoS_2 monolayer. d) Double-logarithmic plot of the SH power dependent on the FH power. e) Polar plot of the SH intensity dependent on the FH polarization. f) SH intensity map plotted for the patterned MoS_2 monolayer.

The ultrathin MoS_2 monolayers are CVD grown on top of a silicon substrate with a 300 nm SiO_2 thermal oxide layer by the group of Andrey Turchanin, Institute of Physical Chemistry, Friedrich Schiller University Jena, Germany. These monolayers are patterned by FIB milling (FEI Helios NanoLab G3 UC) as described in Section 3.1.4, with a careful treatment using accelerated ions of an energy of 30 keV and an ion current of 1.1 pA. This helped to focus the beam to a very small spot and thereby enabling a high resolution. To realize a high quality pattern, the beam is scanned across the flake for 20 times, resulting in a dose of 11 ions/nm^2. Note, that the FIB milling and the AFM measurements were performed by Michael Steinert and Rajeshkumar Mupparapu from the same research group as this work's author, Nano & Quantum Optics at the Institute of Applied Physics, Friedrich Schiller University Jena, Germany.

By this process, elaborate designs for spatial patterns can be realized. As a first simple example, one-dimensional gratings of different period (625 nm, 675 nm and 725 nm) were fabricated to observe SH diffraction from this ultra-thin material as depicted in the illustration in Fig. 6.1(a). The periods are chosen to lie well below the FH wavelength of 840 nm, so the FH does not get diffracted, but to be large enough to enable the collection

of the first diffraction order of the SH with a microscope objective of numerical aperture NA=0.85.

The AFM image in Fig. 6.1(b) shows the height map of the realized one-dimensional grating designed with a period $p = 725$ nm, which is measured to be $p = 713$ nm ± 13 nm. The plot below shows the height profile of the red dotted line in the AFM image. The higher regions, here depicted by the brighter yellow and white colors, are the ion-beam treated regions where the MoS_2 monolayer is removed. The height increase can be associated with an amorphization of the solid SiO_2 layer due to Ga-ion implantation[?] . The two dotted lines in the height profile indicate the height difference between unexposed substrate and unexposed MoS_2 monolayer which is around 1 nm, matching with the ultra-thin thickness of a MoS_2 monolayer. The duty-cycle $dc = a/p$, i.e. the ratio of the unstructured stripe width a divided by the period p as depicted in Fig. 6.1(b), is measured as $dc = 0.40 \pm 0.02$ differing from the designed $dc_{\text{designed}} = 0.50$. The reason might be that the Ga-ions scatter inside the substrate, reaching back to the surface and kicking further atoms away. This increases the damaged surface area compared to the area exposed by the beam.

Despite the unintentionally increased removal or damage of the monolayer, enough intact crystalline MoS_2 monolayer is left to observe SH and the respective diffraction as described and discussed in the next section.

6.2. Second-harmonic diffraction

The SH response from the structured MoS_2 monolayer flake shown in the microscope image of Fig. 6.1(c), presenting the grating pattern, is measured with the home-built SH microscope as described in Chapter 4. The used FH wavelength of 840 nm matches with the C-absorption peak (or C exciton) of the MoS_2 monolayer at the corresponding SH wavelength of 420 nm, which exhibits the strongest SHG due to an excitonic resonance as described in Section 3.1.2. The FH spot size on the sample is controlled via an aperture in front of the beam splitter, which decreases the filling of the focusing microscope objective aperture, decreasing the effective NA and thus increases the spot size. The collected SH signal is obeying the quadratic dependence of the SH power on the FH power as confirmed in the measurement shown in Fig. 6.1(d) presenting both quantities in a double

logarithmic plot. The measured SH signals (orange dots) follow the black line which represents a quadratic function of the FH power.

The characteristic dependence on the FH polarization is shown in Fig. 6.1(e). The SH is measured at a fixed polarization while the FH polarization is changed as described in Section 3.1.2 confirming the four-fold pattern characteristic for the second-order nonlinear susceptibility $\hat{\chi}^{(2)}$ of a MoS_2 monolayer. The essential information lies in the confirmation of the dependence for both unstructured and structured areas of the MoS_2 monolayer flake. This verifies that the crystal structure of the MoS_2 monolayer in the leftover stripes of the structured areas is still intact and not deformed.

Fig. 6.1(f) shows an intensity map of the SHG excited by a FH spot of 1 μm diameter scanned across the MoS_2 monolayer flake shown in Fig. 6.1(c). The unstructured area of the MoS_2 monolayer provides a strong SH intensity, while the patterned area emits a weaker but not zero signal. Due to the spot size of the FH excitation, which is larger than the width of the leftover MoS_2 monolayer stripes, the latter are not resolved. The conversion efficiency in the unstructured area is around $\frac{I_{\mathrm{SH}}}{I_{\mathrm{FH}}} \approx 4 \cdot 10^{-10}$ at a FH average power of 2 mW, and thus comparable to similar experiments on MoS_2 monolayer crystals[?] .

The ratio of the SH power emitted from the structured and the unstructured area is 0.23 ± 0.03, which does not agree with the duty cycle of $dc = 0.4$ measured from the AFM image, as the emitted SH power should linearly depend on the area of the nonlinear material. A possible explanation of the reduced SH lies in the collection of the SH. The small excitation spot excites only one stripe of the MoS_2 monolayer stripes, which width is smaller than the SH wavelength. Thus, the SH is radiated into a large range of angles, of which just a certain part is collected by the limited NA of the microscope objective.

The observation of SH diffraction from the MoS_2 monolayer gratings is performed with a larger spot diameter of $\approx 7\,\mu$m FWHM to excite several stripes and thus periods of the grating. Fig. 6.2(a) shows the microscope image of a grating with period $p = 675$ nm. The respective SH signal representing the spatial distribution is provided in Fig. 6.2(b), here as a single shot camera sensor image. Several high intensity stripes are visible corresponding to the MoS_2 monolayer stripes. The white intensity profile on the bottom of the plot shows the intensity at the white dashed line representing the periodic arrangement of the MoS_2 monolayer grating.

The spatial distribution represents a finite periodic arrangement of coherent SH sources which exhibits diffraction. Due to the choice of the period, the zero and first diffraction

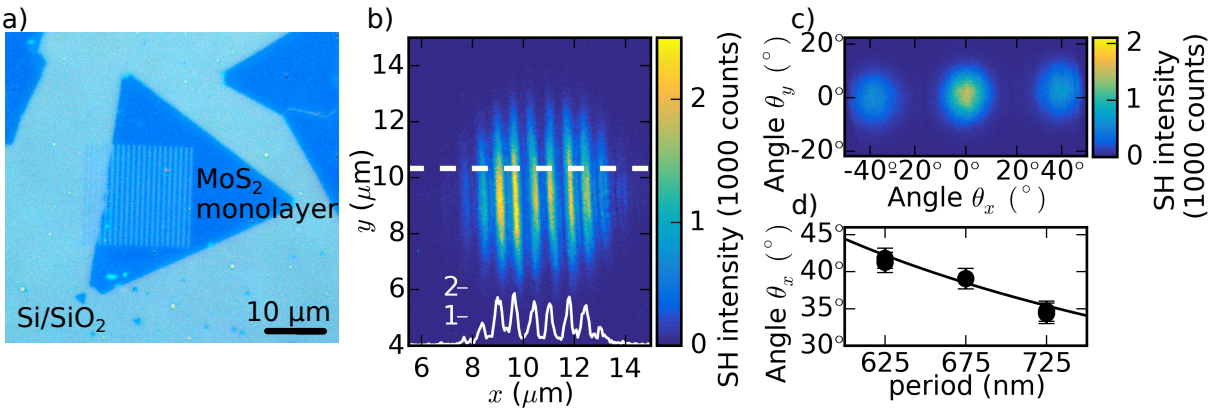

Figure 6.2.: a) Optical microscope image of investigated sample. b) Spatial distribution of the SH intensity. c) BFP image of SH intensity. d) Propagation angle of the first diffraction order versus the grating period, experiment depicted by dots with error-bars, theoretical value shown by solid line.

orders can be collected with the used microscope objective with NA=0.85. Fig. 6.2(c) shows the angular distribution of the SH field, measured via BFP imaging as described in Section 4.3. Note that the measured intensity is corrected for the apodization error from the microscope objective[?] by multiplication of the factor $\cos(\theta)$ in both x- and y-direction resulting in $I_{\text{corrected}} = I_{\text{measured}} \cos(\theta_x) \cos(\theta_y)$. Three maxima are observed, one at the center being the zero diffraction order, and two in the direction in which the grating is periodic, here x, i.e. the first diffraction orders. The propagation angle of the latter with respect to the normal is $\theta_x = 39°$ and agrees well with the theoretical prediction for this grating period and SH wavelength, see Eq. 2.14. This is confirmed for the other grating periods and plotted in Fig. 6.2(d) with the angle θ_x versus the period. The solid line represents the theoretical expectation.

Analyzing the SH intensities in the zero and first diffraction orders, a ratio $R = 1.72 \pm 0.12$ is found. Following the diffraction theory of a periodic but finite multiple-slit experiment as described in Section 2.3, R is dependent on the duty cycle dc. Comparing with the theory, the experimentally found ratio R matches with a duty cycle of $dc = 0.30 \pm 0.02$. In comparison with the measured dc from the AFM image in Fig. 6.1(b), it is lower, similar to the result of the estimation from the SH intensity map in Fig. 6.1(f). This mismatch might follow from damaged edges of the leftover MoS_2 monolayer stripes. They might be loaded with defects occuring from lateral scattering of particles in the substrate, reducing the nonlinearity. Accordingly, the width of the MoS_2 monolayer stripes that actually contribute to the SHG is narrower than expected from the AFM measurement. To circumvent this problem, the writing procedure has to be changed, e.g. with even lower ion doses but more passes of the ion beam, optimized shapes of the focused

ion beam, or a different ion material replacing the gallium.

The observation of SH diffraction in patterned MoS_2 monolayers even if it is the simple concepts of one-dimensional gratings, paves the path toward additional functionality of second-order nonlinear 2D materials used for nanostructured surfaces. To prove a more fascinating scheme, the next section deals with a hologram generating SH vortex beams.

6.3. Second-harmonic vortex-beam

Realizing more elaborate patterns, nonlinear computer generated holograms representing words or symbols are possible, as in Dasgupta *et al*[?] , showing the potential of beam shaping. Especially the generation of beams with particular shape and phase distribution is a crucial feature of metasurfaces. This section deals with a nonlinear hologram from MoS_2 monolayer implementing SH vortex beams by linearly polarized Gaussian FH excitation.

Fig. 6.3(a) presents the black-and-white image of the designed structure used for the FIB milling. The one-dimensional grating is deranged by an additional semi-infinite stripe. All other stripes bend around the topological dislocation at the tip of the semi-infinite stripe. This fork-like structure is defined by the spatially varying transmittance function[? ?]

$$t(x,y) = \frac{1}{2}\left(1 + \text{sign}\left(\cos\left(\frac{2\pi x}{p}\right) + l\arctan\left(\frac{x}{y}\right)\right)\right) \ , \tag{6.1}$$

with the period p and the topological charge l. Such a dislocation acts as the center for a special type of interference, generating a vortex beam, i.e. a beam with vanishing

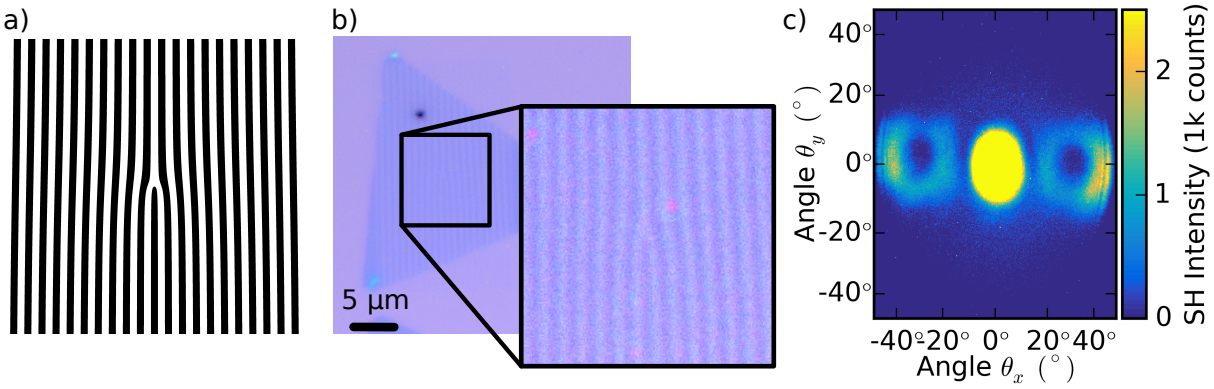

Figure 6.3.: a) Design image of the fork-like grating structure. b) Microscope image with zoomed region of the realized pattern. c) BFP image of the SH intensity showing the vortex beams in the first diffraction orders.

intensity at the center. Generating such vortex beams by nonlinear frequency generation from such fork-like structures was shown before for SHG using poled lithium tantalate[?] and for third-harmonic generation from a gold grating[?] .

As before, the fork-like structure is directly written into the MoS_2 monolayer by FIB milling. Fig. 6.3(b) shows the realized structure ($p = 725$ nm and $l = 1$) in a microscope image with a contrast enhanced zoomed-in section visualizing the dislocation.

That a vortex beam was generated in the SH field could be observed in the angular spectrum plotted in Fig. 6.3(c). The SH signal from the zero order is over-saturated, due to the long exposure time needed to actually observe the SH signal in the first diffraction order. The latter shows a ring of SH intensity and a zero-intensity center. This confirms the generation of a vortex beam in the first diffraction order by SHG from a patterned MoS_2 monolayer.

This study together with Ref.[?] show the possibility to use ultrathin TMD monolayers for nonlinear computer generated holograms by directly patterning the structures into the 2D material. In terms of possible patterns, there are two major limitations.

One is the size of the monolayers which in exfoliation typically is in the range of microns, in CVD growth typically tens, maybe hundreds of microns for single crystals, also called flakes. It is possible to grow extended monolayer thin-films, which are already commercially available, but they consist of many crystals grown together offering grain boundaries, i.e. defects, as well as a mix of SHG from differently orientated areas on the thin film.

The second limitation for patterns is the FIB used in the fabrication. It typically has a certain resolution depending on the ion material, energy and current, ranging in the area of 5 nm for the machine used here. The other point is again the size of the pattern and with that the writing time. Especially considering a high quality pattern using a low dose but many passes can take hours. In that case, drifts in the machine by scanning over the sample have to be considered, too.

Very complex holograms typically need large areas to introduce certain periodicities including very versatile unit-cells. This can either be challenging due to the fabrication limits as explained before, but also by the optics using large excitation beams but also large NA collecting lenses.

However, the most crucial optical limitation is the SH power. The smaller the structures in an elaborate hologram, the less SH signal is generated. Especially if the ratio

between remaining and removed monolayer material is too small, the most creatively designed hologram will not be observable. The second-order nonlinear susceptibility of TMD monolayers is strong, but the conversion efficiency is low due to the very small interaction volume.

Unfortunately, it is not possible to design structures in the monolayers which support Mie-type resonances. This is again a problem of their ultrathin thickness, providing not enough space for confinement of light which could be excited by optical waves. The TMDs belong to the high-index materials. Like silicon, MoS_2 has a refractive index of above 3 in the visible spectrum. Nevertheless, even this high index cannot increase enough the optical thickness of the monolayer to enable confinement.

However, recently it was possible to generate Mie-type resonances in structures of few-layer TMD monolayers[?] . Additionally, it was shown that artificial stacking of intentionally likewise oriented monolayers keeps the broken inversion symmetry[?] , which then would allow for thicker second-order nonlinear TMD films, which might enable the design of resonant nanostructures without losing the nonlinearity. Nevertheless, this is not possible for monolayers. Another technique for enhancing the SHG in TMD monolayers is of need if they are supposed to provide their nonlinearity in applications as integrated circuits or entangled-photon sources.

One possibility is not to pattern the 2D material itself, but the surrounding material, creating hybrid systems of resonant photonic nano-structures covered by a TMD monolayer. The next chapter reports experiments with such hybridized systems of resonant Si metasurfaces covered by MoS_2 monolayers.

7. Second-harmonic enhancement in hybrid nonlinear metasurface

7.1. Combining 2D materials with photonic structures

Nonlinear photonic metasurfaces which are supposed to generate light, typically lack conversion efficiency due to the inherently small nonlinear susceptibilities and in the case of nanostructures due to the small interaction volume. When it comes to the point of practicability in applications, enhancement of the conversion efficiency is needed. This particularly applies to second-order nonlinear metasurfaces including TMD monolayers. They have a comparably strong second-order nonlinear susceptibility, but only with respect to their ultrathin thickness. Typical enhancement strategies like nano-structuring of these 2D materials to create resonant cavities fail. However, they can be coupled to other photonic structures, creating hybrid nonlinear metasurfaces. Due to the ultrathin dimensionality of these monolayers, the hybrid system can still be compact and light-weight for integrated systems and portable devices. Due to advancing transfer technologies, the realization is possible. Here, especially flat topologies of the photonic structures increase the accessibility for the plane 2D material.

In this chapter, a hybrid nonlinear metasurface consisting of a MoS_2 monolayer covering a multi-resonant Si metasurface is discussed. The content reported in this chapter has been recently published by this work's author and collaborators[?] . The first section shortly introduces the idea of hybridization with its purpose and its advantages. The second section describes in detail the multi-resonant Si metasurface used here as the linearly behaving photonic structure to which the monolayer is coupled. The second-harmonic response and especially the enhancement are discussed in the third section, followed by the reason for the observed and typically counter-intuitive difference between the different investigated resonances in the last section providing guidelines for the use of hybrid nonlinear metasurfaces including 2D materials.

Hybridization of two or more systems means the combination of these systems to couple their properties, typically to overcome disadvantages of one system with the advantages

of the other, and to add new features to otherwise less interesting systems.

In this work's context, the term hybrid system stands for a nonlinear photonic metasurface consisting of a linear Si metasurface covered by the nonlinear MoS_2 monolayer. In contrast to intrinsically nonlinear metasurfaces made from GaAs as in Chapter 5 or $LiNbO_3$[?] , the fabrication technology of Si structures is highly investigated, massively used, customizable, precise and comparably more available. Second-order nonlinear TMD monolayers are transferable on target substrates and structures. It is therefore possible to place monolayers on or next to photonic structures. It is also possible to place nano-particles or other structures on top of monolayers. This idea of hybrid structure thus enables second-order nonlinear processes in structures without intrinsic second-order nonlinear susceptibility.

This hybrid system of TMD monolayers on Si metasurfaces suggested here is especially useful since the flat topology of the Si metasurfaces fits with the planar 2D materials. Correspondingly the transfer is not bound to difficult adjustments. The nicely tunable Mie-type and collective resonances of Si metasurfaces can be used to achieve field enhancement at the FH to enhance the SHG.

Similar hybrid systems with TMD monolayers have been successfully implemented for the investigation of excitons and the enhancement of photoluminescence[? ? ? ? ? ? ? ? ?] . SH enhancement, however, has been shown for different systems[? ? ? ? ? ?] , but typically lacked different features, like scalability and practicability of the photonic structure platform for applications as well as actual enhancement.

The hybrid system used here exploits the scalability, homogeneity and reproducability of CVD-grown MoS_2 monolayers for the second-order nonlinearity and the also scalable and well investigated platform of Si photonics for the creation of resonances to enhance the excitation fields for the SHG. The later reported SH enhancement is not as high as in references[? ? ?] but the used platform is scalable and less complicated in usage. The SH enhancement does however outperform the values shown in the references[? ? ?] . The detailed analysis of the experiments and numerics shows that with better resonance design even larger SH enhancement might be possible.

Fig. 7.1(a) shows a visualization of the hybrid system generating SH by FH excitation. The Si metasurface has a resonance at the FH wavelength and creates field enhancement which induces a stronger nonlinear polarization into the MoS_2 monolayer which then generates enhanced SH. Due to the periodic arrangement, SH diffraction can occur, which is stylistically shown by the SH radiation under oblique angle.

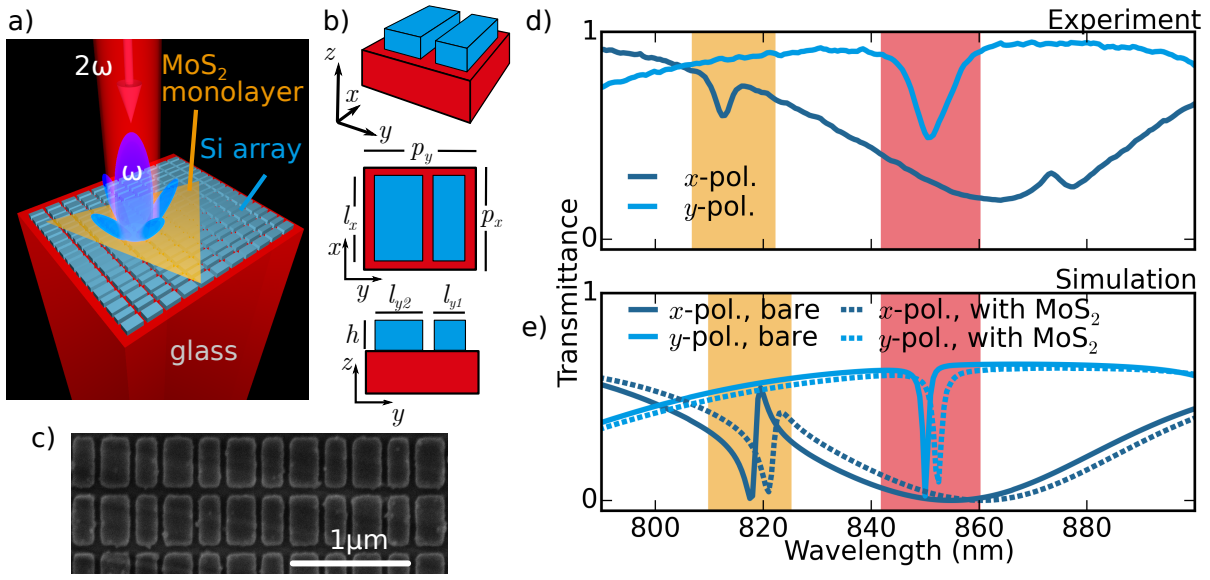

Figure 7.1.: a) 3D sketch of SHG in the hybrid system. b) Sketch of the unit cell of the Si metasurface in oblique, top and side view. c) AFM image of the fabricated Si metasurface. d) Linear transmittance measurement for x and y polarized excitation. e) Numerically simulated linear transmittance for x and y polarized excitation.

The best usage of hybrid systems is possible if each sub-system is well known. The ability to generate SH and other properties of TMD monolayers are well understood although still more investigations are in progress. One respective study is shown in the previous chapter. The properties of the used Si metasurface are described and interpreted in detail in the next section.

7.2. Multi-resonant Si metasurface

By structuring silicon thin-films and let them interact with electromagnetic waves, the field of *silicon photonics* was born. Its impact in photonics and optics was and still is large[? ? ?] . The advanced structuring due to the developments in electronic chips brought big advantages for the use in photonics. The high refractive index of the material enabled the confinement of light inside of the structures leading to waveguides supporting all kinds of modes and nanostructures allowing for Mie-type resonances. These possibilities were already exploited in many linear and third-order nonlinear metasurfaces and resonance designs have been established in many formats. This advantage is used here to create field enhancement overlapping with the later covering 2D material to enhance the generation of SH emission.

The aim of overlapping fields with the 2D material arises from the SHG process as it is described in Section 2.2. Since the second-order nonlinear material is the monolayer, the nonlinear polarization is only induced there which means the SH field is also only generated there. Accordingly, a very strong field enhancement in a photonic structure far away from the nonlinear material does not increase the SHG. Thus the investigated resonances in the Si metasurface used here are conceptually designed to overlap with the 2D material.

Another aim is a strong resonance, i.e. a strong field enhancement. This is achieved by using collective resonances in the metasurface as described in Section 2.1.2. Stronger field enhancement combined with the before mentioned overlap to the 2D material leads to a larger induced nonlinearity and thus to an enhanced SH.

The multi-resonant Si metasurface used here consists of a periodic arrangement of an asymmetric double-bar meta-atom which is depicted in Fig. 7.1(b) having two differently wide Si bars with the lengths $l_x = 395$, $l_{y1} = 165$ nm, $l_{y2} = 225$ nm, the height $h = 135\ nm$ and the periods $p_x = 470$ nm, $p_y = 520$ nm. The SEM image in Fig. 7.1(c) shows the realized Si metasurface, which was fabricated by electron-beam lithography from a 140 nm thick hydrogenated amorphous Si film on a 1 mm thick glass slide (BK-7). The procedure uses a structured mask based on 200 nm thick ZEP520 positive resist patterned by electron beam lithography (Raith 150 electron-beam writer) which then is covered by 35 nm Al film, which turns into a hard mask using lift-off in a ZEP remover. Following, the Si was etched using CHF_3/SF_6 plasma etching (Oxford system 100 ICP-RIE). Residual Al was removed by an Al wet etchant. Note, that the meta-atom was designed by Kirill Koshelev, and the fabrication was performed by Duk-Yong Choi, both from Australian National University Canberra, Australia.

This asymmetric unit-cell in its periodic arrangement enables the coupling between broad localized resonances to spectrally narrow resonances coming from a collective excitation of many resonators in the metasurface[? ?] . The measured transmittance spectra of the fabricated metasurfaces without MoS_2 monolayer for the two polarizations x (dark blue) and y (light blue) is presented in Fig. 7.1(d), obtained using a self-built transmission microscope utilizing a Köhler illumination scheme with assistance from Tobias Bucher from the same research group as the author at Institute of Applied Physics, Jena, Germany. The illumination is realized by a halogene lamp and the spectrum is taken by a spectrometer (Horiba iHR320 with Synapse 1024x256 CCD) with a 600 lines per mm grating resulting in a 0.4 nm resolution. Both spectra are referenced to the transmission

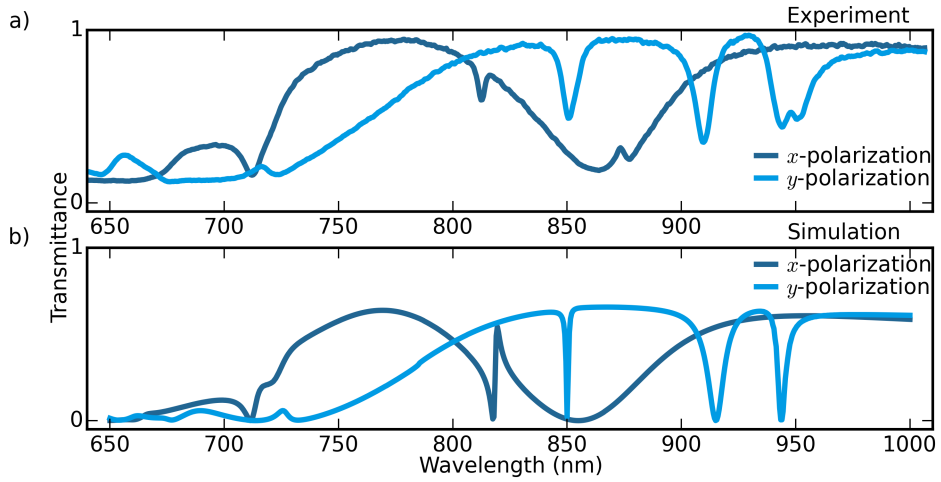

Figure 7.2.: a) Linear transmittance measurement for x and y polarized excitation. b) Numerically simulated linear transmittance for x and y polarized excitation.

of the glass substrate without Si film. In x-polarization, a sharp resonance is found close to 820 nm (orange shading) having a high Q-factor of approximately 250. A second resonance could be observed for y-polarization at a wavelength of 850 nm (red shading) having a Q-factor of 100. These two resonances match with the corresponding FH wavelength associated with the excitonic resonance enhancement of the SHG at the C-transition of the MoS_2 monolayer.

The high Q-factor makes both resonances promising candidates for the use in the hybrid nonlinear metasurface. Numerical simulations of the bare metasurface provide some more information onto the two resonances. To generate the spectra shown in Fig. 7.1(e), a series of independent simulations is conducted each using a monochromatic plane wave excitation with changing wavelengths. The whole field scattered and confined by the meta-atom with periodic boundaries is calculated by using the before mentioned FEM solver of JCMwave[? ?] and material values for amorphous Si given by the fabricating collaborators at Australian National University Canberra, Australia. Then the transmission is taken for each wavelength. The resulting spectra in Fig. 7.1(e) match well with the measured ones in Fig. 7.1(d). The resonance around 820 nm for x-polarization shows an asymmetric line shape which can be associated to a Fano-type resonance. It will further be referred to as the Fano resonance. The other resonance found for y-polarization exhibits a Q-factor of 850, which is larger than in the experiment which can be attributed to inhomogeneous broadening of the measured resonance due to small fabrication imperfections perturbing the periodicity of the metasurface. Typically, Mie-type resonances are not significantly affected by such imperfections due to their broader linewidth, i.e. their lower Q-factor.

By adding a MoS_2 monolayer, modeled in the simulation by the material properties

given in[?] , the resonances slightly shift to longer wavelengths, as can be seen by the dashed lines shown in Fig. 7.1(e). Furthermore, the resonances are broadened, leading to a Q-factor of about 550 for the collective resonance.

The spectra shown up to now do only show a small range of wavelengths which are reasonable to investigate for the SH enhancement. However, the Si metasurface exhibits more resonances and features. In Fig. 7.2(a), the transmission spectrum is shown from 650 nm to 1000 nm for both excitation polarizations in x- and y-direction. The respective numerical simulations presented in Fig. 7.2(b) match with the measurement in many details. Not only the resonances relevant for the SH enhancement are well matched, but also many other resonances and features. This agreement leads to the assumption that the numerical simulations are quite close to the actual physics happening in the real structures which allows to use other results from the simulations, e.g. the field distributions at the resonances, for further discussions and explanations.

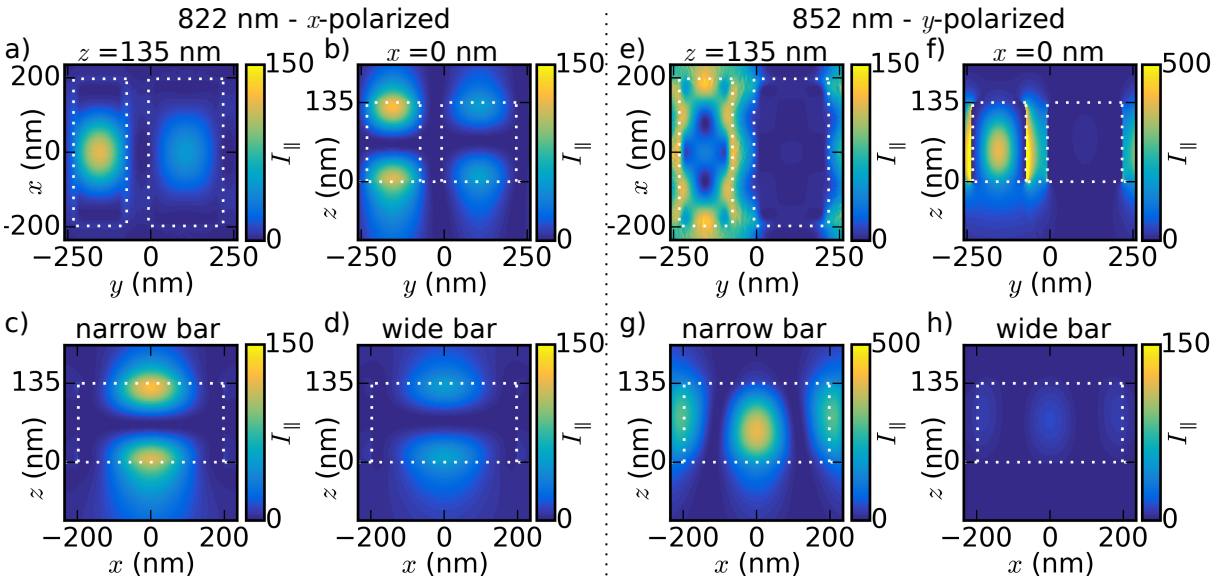

Figure 7.3.: Numerically simulated linear fields (intensity, normalized to an exciting plane wave with amplitude 1) for (a-d) 822 nm with x-polarized light and (e-h) 852 nm with y-polarized light. (a),(e) Top view on x, y-plane at $z = 135\,nm$. (b),(f) Side view on y, z-plane at $x = 0$. (c),(g) Side view on x, z-plane at the center of the narrow bar with respect to y. (d),(h) Side view on x, z-plane at the center of the wide bar with respect to y.

As mentioned before, the field distributions which arise at the resonances are important to study with respect to the overlap with the 2D material. The corresponding field distributions in the Si meta-atoms including a covering MoS_2 monolayer at the resonance wavelengths are shown in Figs. 7.3(a-d) and (e-h). Regarding the SH response of MoS_2 monolayer, only the field components parallel to the plane of the 2D mate-

rial contribute, thus the intensity plotted consists only of these parallel components: $I_{\parallel}(x,y,z) = |E_x(x,y,z)|^2 + |E_y(x,y,z)|^2$. The top left figures in each quadruple ((a) and (e)) represent the x,y-plane directly on top of the Si bars, where the monolayer lies, while the top right figures ((b) and (f)) show the y,z-plane at $x = 0$ which means the center through the bars. Additionally, the bottom images provide the x,z-plane through the center of the narrow (left, (c) and (g)) and the wide (right, (d) and (h)) bar.

The strong field of the Fano resonance is concentrated at the top and bottom of the narrower bar, located in its center along the x-direction at $x = 0$. A much weaker similarly distributed field is located in the wider bar. A large part of the field is overlapping with the 2D material, in particular directly above the narrower Si bar.

The second collective resonance also concentrates inside the narrower bar, but as one strong maximum in its center. The important difference to the Fano resonance however is that significant parts of the field are located in the gaps to the other bars, even reaching over the bars. This creates an overlap with the 2D material aside the Si interface, i.e. in the area, where the monolayer is suspended in air.

These different locations of strong field concentrations is what separates both resonances from each other. The quantity $I_{\parallel}^{\mathrm{MoS_2}} = \int \mathrm{d}x\mathrm{d}y\; I_{\parallel}(x,y,z = 135\,\mathrm{nm})$ represents the total field overlapping with the MoS_2 monolayer. The maxima of $I_{\parallel}$ in the plane of the 2D material at $z = 135$ nm are comparable for both resonances. However, $I_{\parallel}^{\mathrm{MoS_2}}$ for the regions where the MoS_2 monolayer is suspended in air, is only 11% of the total field in the investigated plane for the Fano resonance, while for the second collective resonance this ratio results in 50%. To put these values into perspective, only 37% of the area of the monolayer is suspended in air, whereas 63% have an interface with the Si bars.

This difference can play an important role since the area where the field overlaps with the monolayer is where the nonlinear polarization is induced. But whether this nonlinear polarization and thus the generated SH field are at the Si interface or where the monolayer is suspended in air leads to different scattering, absorption and thus radiation of the SH.

Since the SHG process depends on the exciting linear field, the resonant field distributions in terms of localized strength, polarization and location play an important role. The two investigated resonances show different but both high Q-factors, both are mostly linearly polarized in the direction of their excitation, but they have a very different area of overlap with the 2D material. The respective SH response of the hybrid nonlinear metasurface is investigated in the next section, focusing on the different SH enhancement results from

both resonances.

7.3. Resonant enhancement of second-harmonic generation

The combination of the before described multi-resonant Si metasurface with the covering MoS_2 monolayer as an example of an application-friendly hybrid nonlinear metasurface for second-order nonlinear processes is described in the next section with respect to the SH response focusing on its standard SHG properties like polarization dependence, but especially on enhancement. The latter is the purpose of this chapter to overcome the inherently small nonlinear susceptibilities of nonlinear materials, here in the case of metasurfaces in terms of resonances achieved by nanostructures.

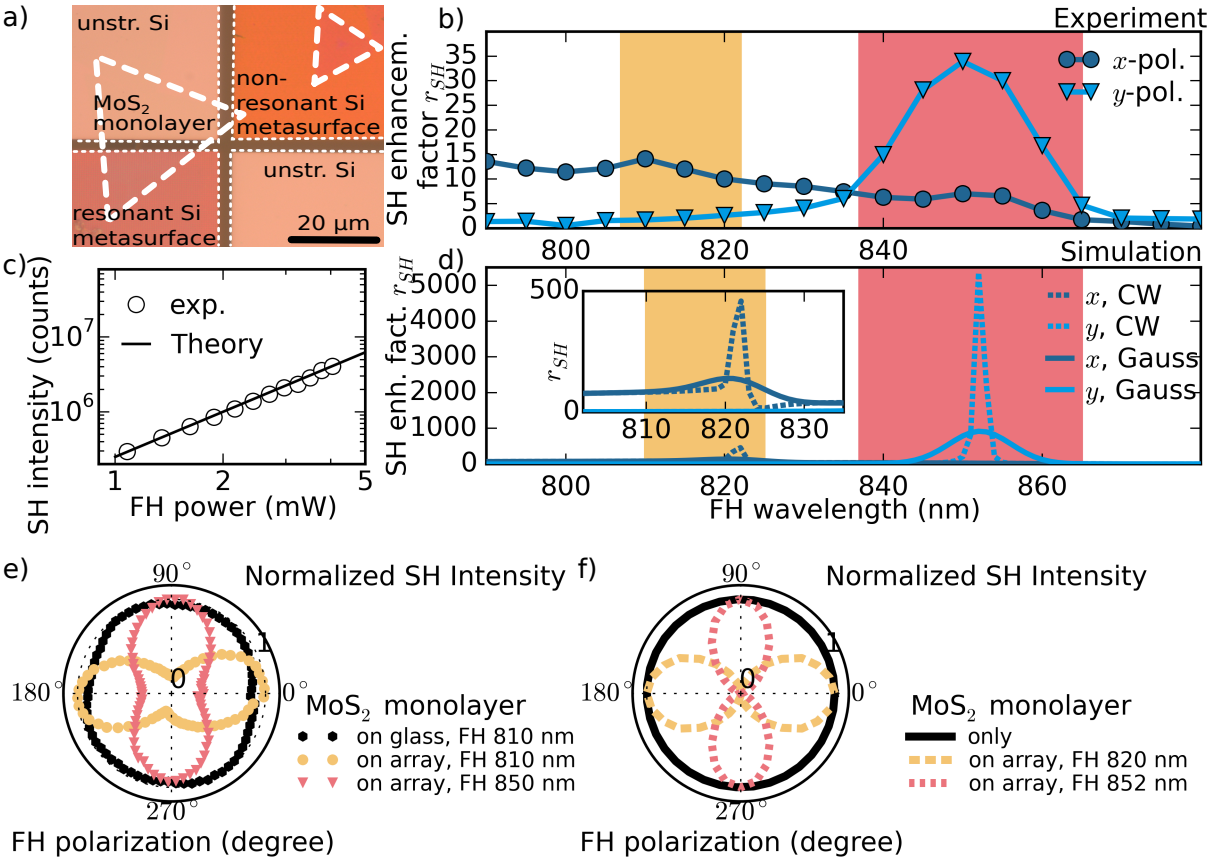

Figure 7.4.: a) Optical microscope image of hybrid nonlinear metasurface. b) SH enhancement factor r_{SH} dependent on the FH wavelength for FH polarization in x- and y-direction. c) SH power dependent on FH power. d) Numerically simulated SH intensity represented by the SH enhancement factor r_{SH} dependent on the FH wavelength. e) Normalized, measured SH intensity dependent on FH polarization. f) Numerically simulated and analytically calculated SH intensity dependent on FH polarization.

The investigated sample, i.e. the completed hybrid nonlinear metasurface including the

transferred MoS_2 monolayer, can be seen in the microscope image in Fig. 7.4(a). The lower left reddish patch is the resonant Si metasurface described in the section before. On the top left and bottom right, two patches of unstructured Si film with the same height as the metasurface are located. In the top right, another Si metasurface with different geometric parameters is placed having no resonances in the investigated area, and thus is called non-resonant Si metasurface. The white dotted lines show the edges of the Si patches. In between, the glass substrate is visible. The CVD-grown MoS_2 monolayer, which are provided by the group of Andrey Turchanin, Institute of Physical Chemistry in Jena, Germany, are just vaguely visible, thus they are framed by the white dashed lines.

The SH response from the hybrid system is measured with the self-built SH microscope described in Chapter 4. Here, the microscope objective with NA=0.85 is used to collect both propagating first and zero diffraction orders of the generated SH. However, small parts of the first diffraction orders might be cut due to the limited NA. This reduces the measured SH power, but it does not influence the following discussion and conclusions.

Fig. 7.4(b) shows the measured spectral dependence of the SH enhancement factor

$$r_{\mathrm{SH}} = \frac{I_{\mathrm{SH,on\text{-}metasurface}}}{I_{\mathrm{SH,on\text{-}glass}}} \ , \tag{7.1}$$

i.e. the ratio between the SH signal from the hybrid system and from a MoS_2 monolayer on the glass substrate. This normalized value eliminates effects from the spectral dispersion of the 2D material's nonlinearity. Also, the comparison with a glass substrate reduces false enhancement interpretations stemming from absorptive reference substrates. Additionally, glass substrates are an easily available substrate and were used in the first SHG experiments on bare TMD monolayers[? ?] , which enables strength comparison. Thus, the enhancement factor defined here represents a useful value to estimate the observed SH enhancement and put it in respect with other works.

The mentioned spectra in Fig. 7.4(b) show a maximum for the y-polarized FH excitation around 850 nm, which corresponds to the second collective resonance (red shading). The enhancement reaches a value of $r_{\mathrm{SH}} = 35$. The larger spectral width of the enhanced SH signal compared to the width of the linear resonance feature is due to the spectral bandwidth of the used FH pulses of 9 nm FWHM and the focused excitation with a diameter of 8 μm FWHM.

In contrast, the Fano resonance in x-polarization (orange shading), exhibits only a small SH enhancement around 810 nm, but no characteristic peak. The measured total

SH conversion efficiency of hybrid structure investigated here is $1.2 \cdot 10^{-9}$ for the Fano resonance and $4.5 \cdot 10^{-9}$ for the second resonance for FH average powers on the sample of 1.85 mW and 1.6 mW, respectively. The characteristic quadratic dependence of the SH power on the fundamental power is confirmed as plotted in Fig. 7.4(c) by comparing measured SH intensity counts (dots) with a quadratic function (solid line).

Fig. 7.4(d) shows the spectra of the SH enhancement factor resulting from numerical simulations using the undepleted pump approximation. The FEM solver used here allows only for monochromatic continuous wave (CW) excitation which is plotted in the graph by the dashed lines. To introduce a SH intensity $I_{\mathrm{SH,Gauss}}$ which is more relatable to the experiment with pulsed, but especially spectrally broader excitation, the convolution of the CW simulations with the theoretical Gaussian excitation pulse of the experiment with the FWHM of $\Delta\lambda = 9$ nm is taken via the formula

$$I_{\mathrm{SH,Gauss}}(\lambda) = \sum_{\lambda_n} I_{\mathrm{SH,CW}}(\lambda_n) \cdot \exp\left(\frac{-(\lambda-\lambda_n)^2}{\frac{\Delta\lambda^2}{2\sqrt{\ln(2)}}}\right) . \tag{7.2}$$

Note that this equation does not represent an actual physical model to determine the transition from CW to pulsed excitation. This is not possible. The here given term only represents the summation over intensities of different wavelength with a weight profile of a Gaussian function. Due to the discrete wavelength steps of the simulation it is a sum rather than the convolution integral. The enhancement factor using $I_{\mathrm{SH,Gauss}}$ is plotted in Fig. 7.4(d) by solid lines.

Taking these two regimes, i.e. CW and Gauss, a large enhancement factor r_{SH} of up to 5000 (CW) is found for the SHG excited at the second collective resonance (red shading), which reduces in the pulsed regime to 1000 (Gauss). At the same time, the CW simulations at the Fano resonance (orange shading) result in an enhancement factor r_{SH} of less than 500. In the case of the $I_{\mathrm{SH,Gauss}}$ the resonant shape in the spectrum is washed out, as visible in the zoomed inset. This fits very well with the observation in the experiment where no explicit resonance behavior could be seen around the Fano resonance.

The enhanced SH background before the Fano resonance, which is observed in the experiments, is confirmed in the simulations and might be associated with the broad resonance feature found around the Fano resonance as can be seen in the linear transmission measurements in Fig. 7.1.

The value of $r_{\mathrm{SH}} = 1000$ for the second collective resonance is large in comparison with

the experiment. However, the large value results from simulations assuming a perfectly shaped and infinitely periodic metasurface. Additionally, the convolution with a Gaussian function to include the pulsed excitation is not a quantitative model. Nevertheless, a part of the difference between the experiment and the simulation can be explained by the already broadened linear resonance in the real metasurface with respect to the linear resonance in the simulation due to fabrication imperfections in the individual nanostructures.

Fig. 7.4(e) shows the experimentally obtained dependence of the generated SH signal on the FH polarization. While the SH from the MoS_2 monolayer on the bare glass substrate (black dots) shows a close to constant behavior over the whole range of FH polarization angles, the SH intensity excited at the Fano resonance (orange dots) and at the second collective resonance (red triangles) have clear maxima in x- (0°) and y- (90°) direction, respectively. This behavior confirms that the SH resonances only exist for these polarizations where the linear resonances appear. Note, that each set is normalized to its maximum value.

These results are confirmed by numerical simulations shown in Fig. 7.4(f). As described in Section 3.1.2, the overall SH signal of a MoS_2 monolayer which is not perturbed by any photonic structure, is constant (see the black line). That both SH signals excited at the Fano and second collective resonance show a strong dependence on the FH polarization matching with the polarization of the original linear resonances, confirms again that there is resonant coupling between the SHG from the MoS_2 monolayer and the linear resonances of the Si metasurface.

The SH response of a periodic arrangement, as in the case of the hybrid nonlinear metasurface presented here, typically can exhibit SH diffraction. As already seen in the GaAs metasurface of Chapter 5 and the patterned MoS_2 monolayers from Chapter 6, SH diffraction stems from the periodic arrangement of sources which emit light at the SH wavelength and thus underlies the laws of diffraction.

While the patterned MoS_2 monolayer was manipulated to explicitly show SH diffraction, resulting in vortex beams in the first diffraction order, the hybrid system described in this chapter is mainly considered in terms of SH enhancement, which was a missing feature in the patterned 2D materials. However, also the hybrid system exhibits SH diffraction which is very different for the two investigated resonances.

Fig. 7.5(a) shows the SH intensity of the hybrid nonlinear metasurface in real space

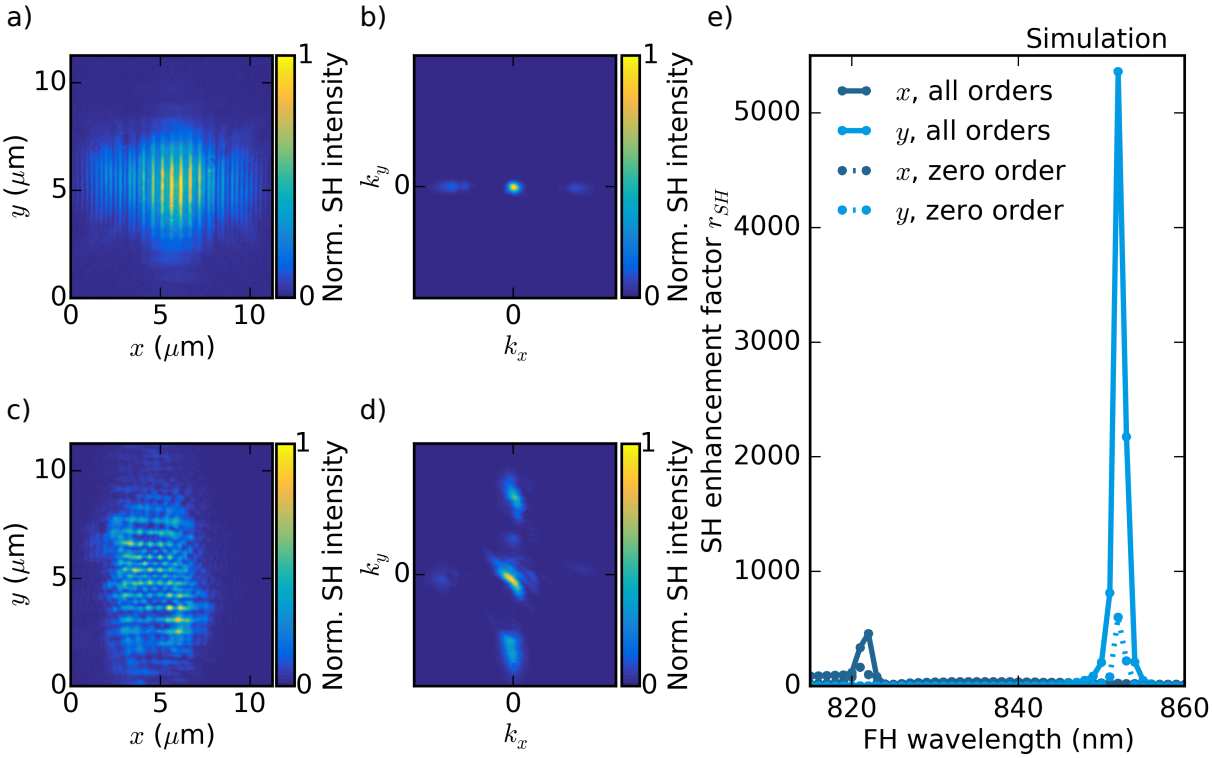

Figure 7.5.: (a-d) SH intensity from hybrid system by FH excitation at 810 nm ((a) and (b)) and at 850 nm ((c) and (d)) observed in real space ((a) and (c)) and in angular space by BFP imaging ((b) and (d)). (e) SH enhancement factor spectrum for only zero diffraction order and for all diffraction orders together.

excited at the Fano resonance with a large excitation spot of a diameter of around 8 μm FWHM. Although the structure is periodic in both x- and y-direction, the SH intensity looks like a one-dimensional line grating source. This behavior is confirmed by the BFP imaging technique performed throughout this thesis to observe the angular spectrum of the SH intensity, which is plotted in Fig. 7.5(b). Here, only the first diffraction orders in x-direction show a significant SH intensity, while in y- direction no first diffraction orders are detected. In contrast, the SH intensities excited at the second collective resonance show the expected real space distribution with small SH spots arranged periodically in both directions (see Fig. 7.5(c)) and the SH diffraction with SH signal in the first diffraction orders in both x- and y-direction (see Fig. 7.5(d)).

The reason for the observation of a one-dimensional instead of a two-dimensional grating when exciting at the Fano resonance might be that the SH field is not locally seperated by nodes in y-direction, but rather continuous across the unit-cell. Another possibility is that the field is actually located at both bars in a similar strength resulting in a period smaller than the wavelength which forbids a propagating first and higher diffraction orders.

The contribution of the first diffraction orders on the overall SH emission is very large. In Fig. 7.5(e), the SH spectrum is separated into the overall SH enhancement factor and

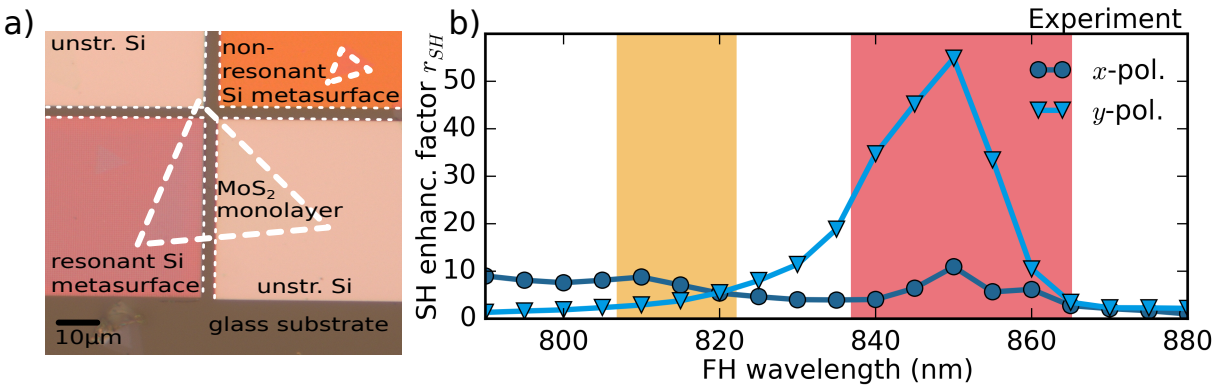

Figure 7.6.: a) Microscope image of similar hybrid nonlinear metasurface. MoS_2 monolayers framed by white dashed lines. Si patches framed by white dotted lines. b) SH enhancement factor r_{SH} dependent on the FH wavelength.

the part which is only resulting from the zero order alone. This issue might be important for future applications trying to harvest most SH emission in the zero diffraction order.

However, it seems possible to not only enhance the SHG, but additionally manipulate the SH diffraction. Of course, more elaborate schemes have to be considered if actual beam shaping and SH enhancement are supposed to work in the similar hybrid nonlinear metasurface.

Note that the SH response from this hybrid nonlinear metasurface is nicely reproduced in a sample with very similar geometry parameters, which is shown in the microscope image of Fig. 7.6(a). The according SH spectra are shown in Fig. 7.6(b). Again the enhancement factor r_{SH} is plotted versus the excitation wavelength. The sprectra show an even stronger enhancement of 55 for the second collective resonance (red shading) than in the main sample. However, in depth analysis of the respective SH properties were not possible, because the sample got destroyed before.

Concluding the SH response of the hybrid nonlinear metasurface, a strong SH enhancement is observed for the second collective resonance while the Fano resonance does not show a pronounced resonant behavior in the SH spectra. Although the latter might stem from the fact that the FH excitation is quite broad, the difference in SH enhancements for the two resonances is significant. The more strange is the fact that not the second collective resonance, but the Fano resonance has the higher Q-factor. The reason for this counter-intuitive result is discussed in the next section.

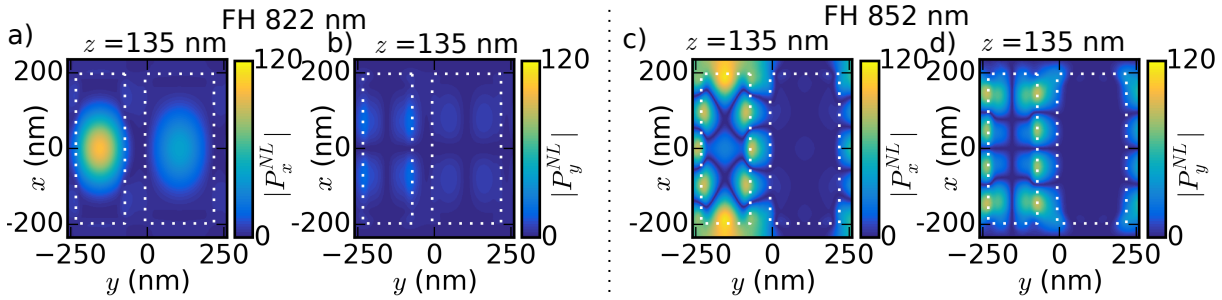

Figure 7.7.: Nonlinear polarization distribution induced by the numerically simulated FH field distributions at the wavelength 822 nm (a,b) and 852 nm (c,d), representing the absolute value of the x-component (a,c) and the y-component (b,d) in the plane of the 2D material.

7.4. Discussion on counter-intuitive Q-factor dependence of second-harmonic enhancement

The difference of the SH enhancement factor for the two resonances, i.e. 15 for the Fano resonance and 35 for the second collective resonance, opposes to the commonly expected enhancement followed by the difference in Q-factor, which was 250 for the Fano resonance and 100 for the second collective resonance. This arises from the complexity of nonlinear processes in nanoresonators such as SHG. The excitation beam creates the local FH field, which induces a nonlinear polarization in the nonlinear material, here the MoS_2 monolayer. This nonlinear polarization is driving a localized field at the SH frequency, which might couple to the far field where it can be observed. In each of these steps, the nanoresonators influence the coupling of the fields and thus the overall efficiency of the SHG. Comparing the two resonances investigated here, the main qualitative difference is how the field in the plane of the 2D material is distributed, i.e. mostly on top of the Si bars, as in the case of the Fano resonance, or where the monolayer is suspended in air, as in the case of the second collective resonance.

The first step in understanding the enhancement behavior is the induced nonlinear polarization. Due to the small conversion efficiency, the undepleted pump approximation can be taken which simplifies the FH, the SH and the nonlinear polarization as time-independent fields. Thus, the nonlinear polarization can be simply calculated by taking the FH fields in the nonlinear material, i.e. in the MoS_2 monolayer, which have already been shown in Fig. 7.3(a,e), and by using Eq. 3.2. The result is shown in Fig. 7.7. While Figs. 7.7(a,b) result from the FH excitation at the Fano resonance, Figs. 7.7(c,d) are connected to the second collective resonance. Since complex fields are used in the simu-

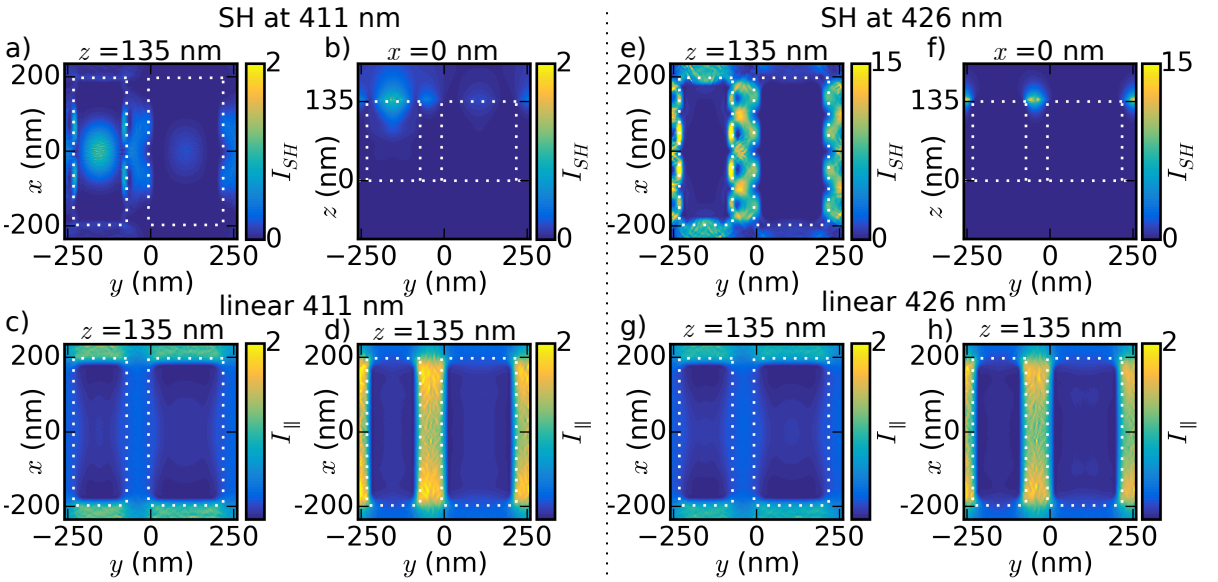

Figure 7.8.: Numerically simulated SH field distributions at the wavelength 411 nm (a-d) and 426 nm (e-h), representing the SH intensity fields (a,b,e,f) and linear intensity fields (c,d,g,h). (a,c,d) and (e,g,h) show the x, y-plane where the monolayer lies at $z = 135$ nm, while (b) and (f) show the y, z-plane through the center of the Si bars at $x = 0$ nm. (a) and (b) were excited by x-polarized FH, while (e) and (f) were excited by y-polarized FH. The linear simulations result from x- (c,g) and y- (d,h) polarized plane waves.

lation, which cannot be shown in this simple 2D plot, the absolute value of the nonlinear polarization for the two different components in x (a,c) and y (b,d), respectively, are depicted.

Since both FH fields at the Fano resonance and at the second collective resonance are mainly polarized in x or y, respectively, as their excitation, the nonlinear polarization is mainly concentrated in the x-component. Only minor contributions are found in the y-component. The major difference is, as mentioned above describing the FH fields, that the location of the nonlinear polarization at the Fano resonance is mainly at the interface of the Si bars while a large part of the nonlinear polarization at the second collective resonance is located where the monolayer is suspended in air.

From this nonlinear polarization, the SH fields are generated following $E_x^{SH} \sim P_x^{NL}$ and $E_y^{SH} \sim P_y^{NL}$. This field is then scattered due to the Si nanostructures. The simulated results are shown in Figs. 7.8(a,b,e,f).

Figs. 7.8(a,b) present the numerically simulated SH field distribution in the case of FH excitation at the Fano resonance. The SH intensity is plotted in the x, y-plane at $z = 135$ nm (a), which is the plane of the MoS_2 monolayer, as well as in the y, z-plane through the center of both bars at $x = 0$ nm (b). Since the actual spectral dispersion of the nonlinear susceptibility is not known, the intensity values are normalized arbitrarily

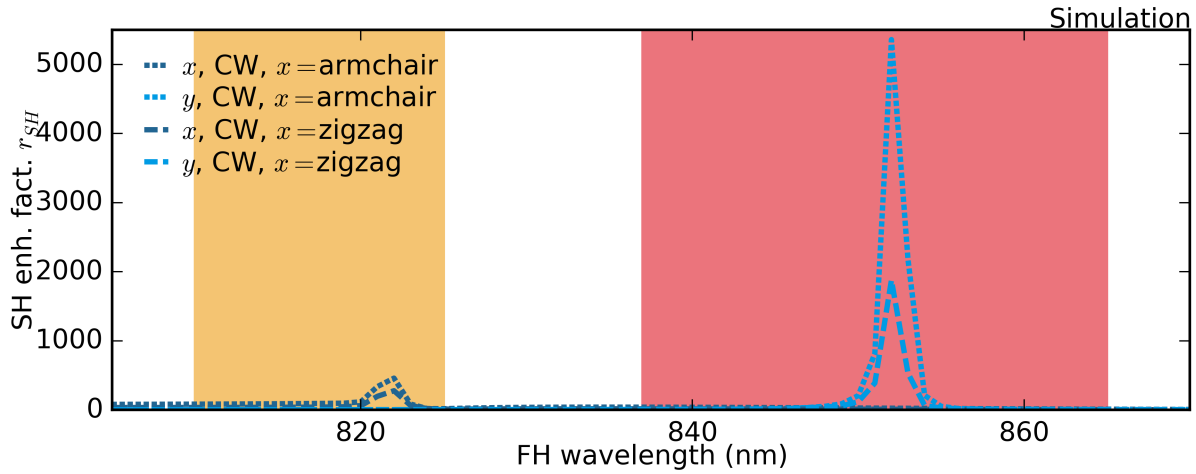

Figure 7.9.: SH enhancement factor plotted versus FH wavelength for MoS_2 monolayer crystal orientation with armchair direction parallel to x (dotted) and the zigzag direction parallel to x (dashed).

to simplify the visualization, but enabling comparison between the different resonances. The strongest intensity is found central on top of the Si bar, as expected from the FH field distribution of this resonance shown in Fig. 7.3(a-d) and the nonlinear polarization shown in Figs. 7.7(a,b). Despite the less pronounced linear field in the gap between the Si bars, the SH field generated there is comparably strong to the field on the Si bar interface. This suppression at the Si interface might stem from the high absorption of light at the SH wavelength in Si. In comparison, Figs. 7.8(c,d) show the linear fields at the SH wavelength excited by x- and y-polarized light, confirming the suppression on the Si bars, and the support of light between the bars.

In contrast to the Fano resonance, the second collective resonance finds a strong overlap of its linear field and thus the nonlinear polarization with the area where the MoS_2 monolayer is suspended in air. Accordingly, the generated SH field is less suppressed by the material absorption of Si and eventually enhanced, as can be seen in Figs. 7.8(e,f). The SH field is mostly located in the gaps between the Si bars with local field intensities about ten times larger than for the Fano resonance. The obtained intensities already confirm the different SHG enhancement factors obtained in the far-field simulations shown in Fig. 7.4(d).

Note that the orientation of the MoS_2 monolayer crystal does play a role (see Fig.7.9). In the simulations reported before, the orientation is taken to be with the armchair direction being parallel to the x-axis. This arrangement is close to the actual case in the experiment. It predominantly induces a nonlinear polarization in x-direction, independent whether caused by a mostly x- or y-polarized FH field. By rotation of the orientation by (2n+1)

times 30° with n being an integer number, mainly x- or y-polarized FH fields induce a nonlinear polarization in y-direction. That means the fields shown in Figs. 7.7(a-d) for the x-component are then the y-component and vice versa.

For the hybrid nonlinear metasurface reported here, this leads to a different SH enhancement factor. Fig. 7.9 shows the SH spectra, plotting again the SH enhancement factor versus the FH wavelength, for x- and y-polarized FH excitation. The dotted lines represent the already shown case for x being parallel to the armchair direction of the MoS_2 monolayer crystal structure. The counterpart is plotted in dashed lines for the zigzag direction being parallel to x. At the Fano resonance (orange shading), the SH enhancement factor decreases for the zigzag orientation to hardly 300 versus the 500 mentioned above for the armchair orientation. At the second collective resonance (red shading), this decrease is even larger, showing a SH enhancement factor of not even 2000 for the zigzag orientation against the value of more than 5000 for the armchair orientation.

The reason for this difference might lie in the different overlaps of the induced nonlinear polarization and the thus generated SH fields with the mainly supported mode of the structure at that SH wavelength which are shown in Figs. 7.8(c),(d),(g) and (h). At these SH wavelengths, x-polarized light is mainly supported being located in the gap between the metasurface bars in x-direction, while y-polarized light is supported being located in the gaps in y-direction.

Concluding from the discussion of the field distributions, it is beneficial for nonlinear interactions to achieve FH field enhancement in the air gap between the Si nanobars, which is attributed to the losses of Si at the SH wavelength. This is a general effect and not specific for the particular geometry investigated here. Correspondingly, next the SHG efficiency from MoS_2 monolayers is compared for different substrates, such as the already described resonant Si metasurface, a non-resonant Si metasurface, and an unstructured Si thin film as depicted in Fig. 7.4(a), as well as the bare glass substrate.

In Fig. 7.10(a), a SH intensity map for x-polarized FH excitation is plotted. It is obtained by scanning over the area and integrating over the whole SH camera image for each position on the map. It demonstrates the strong SH response from the MoS_2 monolayer on top of the resonant Si metasurface. The measurement is taken at a FH wavelength of 810 nm and with an excitation spot of around 8 μm FWHM. There is no SH signal visible from where the MoS_2 monolayer lies on the unstructured Si film, but there is an observable very weak signal if the exposure time is increased. It is around 400

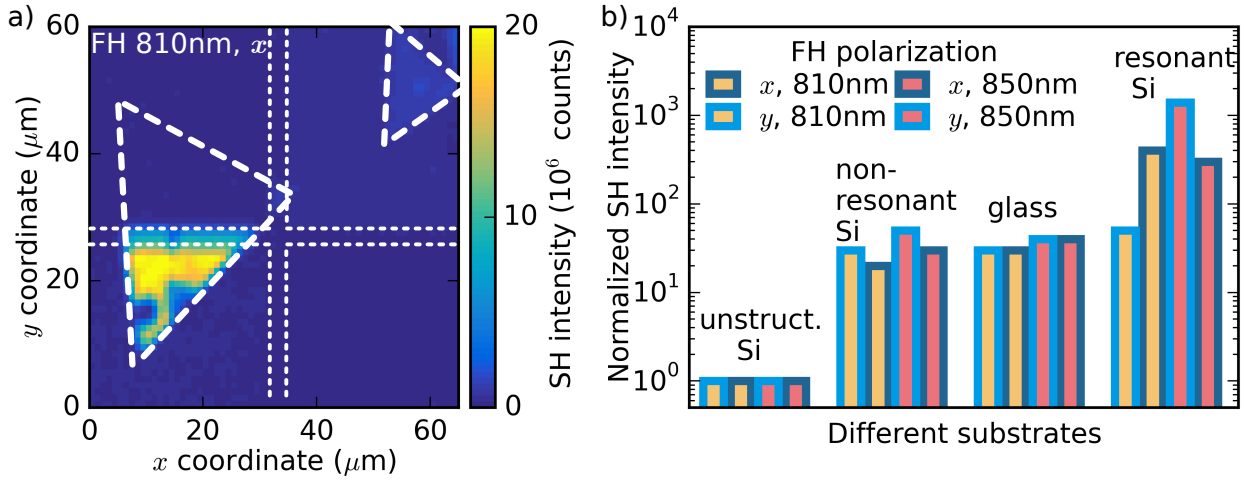

Figure 7.10.: (a) SH intensity map of the area shown in Fig. 7.4(a) for x-polarized FH at 810 nm wavelength. (b) SH intensities of MoS_2 monolayer atop the different substrates for different FH polarizations and different FH wavelengths, normalized to the SH intensity from MoS_2 monolayer on unstructured Si.

times smaller than the value observed from the MoS_2 monolayer covering the resonant Si metasurface. Additionally, a weak signal is measured where another MoS_2 monolayer is atop the non-resonant Si metasurface.

Note, that in Fig. 7.10(a) a very small region is shown where the monolayer is atop the glass substrate. However, this is not where SH measurements are taken for the SH enhancement factor r_{SH}, because here it is actually suspended far above it. The actually reported values for measurements on the glass substrate are using a separate MoS_2 monolayer crystal not shown here. This ensured that the MoS_2 monolayer lied directly on the glass and the 8 μm-wide focus excited a spatially homogeneous region.

To clearly compare the SH strengths for the different patches, the different SH intensities from MoS_2 monolayers on top of the different substrates are compared in Fig. 7.10(b) for the two orthogonal FH polarizations, i.e. x in dark blue and y in light blue, and for both the Fano and the second collective resonance wavelengths, in orange and red, respectively. Such a comparison, even between different MoS_2 monolayers, is possible due to the very homogeneous properties of the CVD-grown crystals. The shown SH intensities are referenced to the measured value on top of the Si thin film, which is the smallest. The SH response from the non-resonant Si metasurface exceeds those of the unstructured Si thin film by a factor of 30 to 50, similarly to the SH signal from the MoS_2 monolayer on the glass substrate. Nonlinear numerical simulations of the SHG from MoS_2 monolayers on Si and on glass substrates show a two orders of magnitude larger SH response for the system with glass which confirms the corresponding measurements.

To conclude, these results from the patch comparison shows that direct contact between

the MoS_2 monolayer and the Si significantly decreases the SHG efficiency, due to strong material absorption of the Si at the SH wavelength. In the case of the non-resonant metasurface, the MoS_2 monolayer is partly suspended in air and thus shows less suppressed SHG with respect to the unstructured Si substrate. The glass substrate does not provide areas of suspended MoS_2 monolayer, but it is transparent at the SH wavelength, which results in larger SHG than in the case of the unstructured Si substrate.

Comparing the SH values for the non-resonant and the resonant Si metasurface, the eminent impact of the resonances for the SH enhancement in hybrid nonlinear metasurfaces is confirmed. This fact is also proven in the case of the resonant Si metasurface at the Fano resonance at the non-resonant FH excitation polarization y. In the case of the non-resonant FH excitation in x polarization at the second collective resonance still the background SH enhancement possibly stemming from the broad resonance in x at the FH plays a role which is shown in Fig 7.4(b) and was discussed before. Thus it might also be *resonant* SH enhancement.

The essential result found from the investigation of this hybrid nonlinear metasurface is the importance of the gaps between the metasurface blocks. There, the nonlinear 2D material can be suspended in air and thus produce more SH than at the interface with the absorbing Si blocks. The guideline for the design of resonances should therefore be to take care of field distributions with local field enhancement in the gaps.

This result can be generalized for the process of SHG in all nonlinear photonic metasurfaces. When resonances are used at the FH wavelength range, their local fields should not only strongly overlap with the nonlinear material, the generated SH field should fit with the metasurface characteristics. As in this study, absorption at the SH wavelength can play an essential role, but if the latter is not as crucial, radiative and non-radiative eigenmodes at the SH wavelength can be key.

8. Conclusion and outlook

8.1. Conclusion

In this thesis, different possibilities of second-order nonlinear metasurfaces are investigated and discussed concentrating on the nonlinear process of SHG.

At first, a metasurface made from the intrinsically second-order nonlinear material GaAs is realized. The structures enable resonances at the FH excitation to enhance the SHG as well as SH diffraction. The latter is crucial in this case since a GaAs thin film with the typical (100)-cut surface does not provide out of plane SH emission by normal incidence FH excitation. Here, the periodic arrangement and the local field enhancement in the meta-atoms helped to observe SH emission in the first diffraction orders, which is observed for the first time in a metasurface of this material class by BFP-imaging.

Additionally, a case of non-zero SH emission in the zero diffraction order is shown, resulting from an effect which could not be fully explained based on the obtained data.

However, the lack of SH emission normal to the surface plane due to the less fortunate second-order nonlinear susceptibility tensor of the GaAs material class has to be overcome for the use of second-order nonlinear photonic metasurface in applications.

In this work, a solution is found by introducing the recently found 2D materials called TMD monolayers which have an intrinsic second-order nonlinear susceptibility with a tensorial structure enabling normal SH emission at normal incidence FH excitation.

By patterning MoS_2 monolayers via FIB milling for the first time, it iss possible to shape the spatial SH response. In particular, SH diffraction from patterned one-dimensional gratings is observed matching with the diffraction theory. Taking this as the fundamental principle, it is possible to realize ultra-thin nonlinear diffractive optical elements for SH beam shaping. As a first example, a vortex beam in the first diffraction order is generated by milling a grating featuring a topological dislocation into the MoS_2 monolayer.

However, the patterning of the MoS_2 monolayer decreases the SH emission due to the removal of material. The already small SH signal due to the ultrathin thickness has to be enhanced to be useful for applications. Thus, a scheme of hybridizing the nonlinear monolayer with a linearly resonant metasurface is implemented in this work. Due to strong

collective resonances in the used Si metasurface, it is possible to observe enhanced SHG. Additionally, the hybrid system is chosen to use the scalable and advanced platform of Si photonics and the scalable, reproducably high-quality CVD-grown MoS_2 monolayer to lead a path toward functionalized large surface application as well as to possibly integrate this hybrid system into optoelectronic chips.

However, the crucial result here is not the sheer number of enhancement, but the guidelines on how to design the linear metasurface to achieve stronger SH enhancement. In particular it is advisable to use resonances providing a local field enhancement overlapping with the nonlinear 2D material away from the Si interfaces and where it is suspended in air. There the absorption of the Si at the SH wavelength cannot suppress the SH emission.

In general, this work emphasizes the complicated role of every step in the SHG process. While the FH excitation already sets the base for an efficient frequency conversion, it is the nonlinear susceptibility tensor which transforms the FH field into the nonlinear polarization. It is therefore crucial how the local FH field is distributed over the nanostructured surface to create a strong nonlinear polarization and thus to generate a strong local SH field. However, again the nanostructured environment of the SH field has an impact on its support and mainly its coupling to the far field, i.e. the radiation properties.

8.2. Outlook

One of the possible directions from here is the further increasing control of SH radiation by SH diffraction. Not only further schemes to generate normal to the surface plane SH emission from metasurfaces using the GaAs material class are interesting. SH beam shaping with computer generated holograms in all kind of nonlinear materials is thrilling. This additional functionality for a surface can also be used for communication and data analysis schemes.

Whether this is possible with metasurfaces with intrinsic second-order nonlinearity or in hybrid systems will be a matter of fabrication possibilities. The hybrid system shown here is highly accessible in todays fabrication technology, but its advances in beam shaping designs is rather low until now. To combine the enhancement and the diffraction pattern might be difficult. Intrinsically nonlinear materials might not need the additional enhancement 2D materials seek, which makes the realization of diffraction patterns easier.

Applications like light sources using SHG or the somehow inverse process of SPDC for entangled photon sources via metasurfaces are still suppressed due to the low conversion

efficiency. Even stronger enhancement mechanisms have to be found. This can be the simultaneous existence of resonances at the FH and the SH, sharper resonances like the here introduced Fano resonance due to asymmetric meta-atoms, or even specially shaped FH excitation beams.

Otherwise, the access to new materials with stronger second-order nonlinearity are key. The perovskites led by $LiNbO_3$ have a strong intrinsic second-order nonlinearity and their fabrication technology gets more advanced everyday. The first realized second-order nonlinear metasurface made from $LiNbO_3$[?] shows a path both for SH emitting metasurfaces and compact quantum entangled photon sources.

The chiral properties of TMD monolayers are already under investigation from several perspectives leading in different directions.

A rather elaborate idea on this behalf is to use the particular tensorial structure of TMD monolayers to create a metasurface which generates circularly polarized SH light by linearly polarized FH excitation. For this, hybrid systems could be utilized, where the linear metasurface locally generates circularly polarized FH light which then is converted to circularly polarized SH light by the TMD monolayers. However, the realization of large enough circularly polarized FH fields without disturbing non-circularly polarized fields in the surrounding is rather difficult.

Nevertheless, the particular properties of the 2D materials especially in terms of chirality are worth to look into.

Abstract

Compact optical and photonic devices have found their way into applications due to their many facets and possibilities to use light. Especially nanostructured surfaces, which drastically manipulate light on a very small spatial scale, also called metasurfaces, were investigated for that purpose over the last decades. However, research on nonlinear properties in such systems is still in a mainly fundamental stage.

Here, different schemes and materials are used to develop second-order nonlinear nanostructured surfaces which support strong second-harmonic generation under controlled radiation.

At the beginning, a gallium arsenide metasurface is investigated whose intrinsic second-order nonlinearity is used to generate second-harmonic light propagating out of the metasurface plane. This is achieved by the periodic design using Mie-type resonances which results in second-harmonic diffraction into the first diffraction order, since the second-harmonic emission normal to the metasurface plane is forbidden for the crystal orientation due to the second-order nonlinear susceptibility tensor. Nevertheless, due to an effect which cannot fully be explained by the obtained data, second-harmonic generation into the zero diffraction order for a symmetry forbidden resonance in the metasurface is observed.

To overcome the issue of no second-harmonic emission normal to the surface, which would be beneficial for applications, the recently found molybdenum disulfide monolayers are investigated. They are ultrathin and thus called two-dimensional materials. Their intrinsic second-order nonlinear susceptibility provides the ability to emit the generated second-harmonic light normal to the surface plane when excited at normal incidence.

Here, for the first time (simultaneously with[?]) such monolayers are patterned with high resolution by focused-ion-beam milling, creating one-dimensional gratings, to observe the diffracted second-harmonic generation. The measured second-harmonic response is observed in the zero and first diffraction orders as expected from diffraction theory. However, in a more elaborate design the grating is manipulated by a topological dislocation to generate second-harmonic vortex beams in the first diffraction order which is successfully implemented and observed. Thus the application preferred ability of the monolayers for nonlinear beam shaping is accessible.

Unfortunately, due to the ultrathin thickness of the material, the conversion efficiencies of the patterned two-dimensional materials are relatively low and thus not feasible for applications. To enhance the second-harmonic generation, a hybrid system of a multi-resonant silicon linear metasurface coupled to a molybdenum disulfide monolayer is investigated using high-quality collective resonances. By measuring and simulating the linear and second-order nonlinear properties, enhanced second-harmonic generation is observed and guidelines on how the resonances should be designed to achieve this result are developed. Following these, it is not only important to have an overlap of the resonant local fundamental field with the nonlinear two-dimensional material, but also to locate this field in the areas where the two-dimensional material is suspended in air.

The here found results help by the development of compact or large-area nonlinear functionalized surfaces for second-order frequency generation, but the results can also be applied for higher-order nonlinear processes. However, the understanding of second-harmonic generation in such systems is opening a path to the likewise second-order nonlinear process of spontaneous parametric down-conversion which enables entangled-photon pair emission for quantum optical applications.

Zusammenfassung

Kompakte optische und photonische Baugruppen und Geräte sind aus Anwendungen aufgrund ihrer Vielseitigkeit in der Nutzung von Licht nicht mehr wegzudenken. Insbesondere nanostrukturierte Oberflächen, auch Metasurface genannt, welche die Eigenschaften des Lichts auf sehr kleinem Raum enorm verändern, wurden für diesen Zweck über die letzten Jahrzehnte untersucht. Allerdings gehören die nichtlinearen Eigenschaften solcher Systeme noch größtenteils zur Grundlagenforschung.

In dieser Arbeit werden verschiedene Ansätze und Materialien verwendet, um nanostrukturierte Oberflächen mit Nichtlinearitäten zweiter Ordnung zu entwickeln, welche starke Frequenzverdopplung unter kontrollierter Abstrahlung vorweisen können.

Zu Beginn wird eine Galliumarsenid-Metasurface untersucht, dessen intrinsische Nichtlinearität zweiter Ordnung genutzt wird, um Licht der zweiten Harmonischen so zu erzeugen, dass es sich aus der Metasurface-Ebene heraus ausbreitet. Mie-artige Resonanzen unterstützende periodisch angeordnete Zylinder führen zur Beugung der erzeugten zweiten Harmonischen, welche dann in die erste Beugungsordnung koppeln, da die Abstrahlung senkrecht zur Metasurface-Ebene für die vorliegende Krystallorietierung aufgrund des nichtlinearen Suszeptibilitätstensors zweiter Ordnung verboten ist. Nichtsdestotrotz wird für eine durch die Symmetrie eigentlich verbotene Resonanz die Erzeugung der zweiten Harmonischen in der nullten Beugungsordnung beobachtet. Der Effekt kann allerdings nicht durch die vorhanden Daten vollständig erklärt werden.

Für Anwendungen wäre eine Abstrahlung der zweiten Harmonischen senkrecht zur Oberfläche bevorzugt. Deshalb werden fortführend die kürzlich entdeckten Molybdändisulfid-Monolagen untersucht. Diese sind ultradünn und werden entsprechend auch als zweidimensionales Material bezeichnet. Ihre intrinsische nichtlineare Suszeptibilität zweiter Ordnung bietet die Möglichkeit die zweite Harmonische senkrecht zur Oberfläche bei senkrechter Eingangsstrahlung zu emittieren.

In dieser Arbeit werden zum ersten Mal (gleichzeitig mit [?]) solche Molybdändisulfid-Monolagen durch hochaufgelöstes fokussiertes Ionenstrahlfräsen zu eindimensionalen Gittern strukturiert um die Beugung der zweiten Harmonischen zu beobachten. Die Messung bestätigt das durch die Theorie erwartete Abstrahlen in die nullte und erste Beugungsordnung. Eine deutlich kompliziertere Struktur jedoch, welche das Gitter durch eine topo-

logische Singularität verzerrt, erzeugt Vortex-Strahlenbündel der erzeugten zweiten Harmonischen in der ersten Beugungsordnung, was erfolgreich verwirklicht und beobachtet wird. Das für Anwendungen erwünschte Modellieren von nichtlinearen Strahlenbündeln ist entsprechend mit den Monolagen möglich.

Leider sind die Konversionseffizienzen der strukturierten zweidimensionalen Materialien durch die sehr geringe Dicke des Materials sehr klein, was für Anwendungen nicht praktikabel ist. Um die Frequenzverdopplung zu verstärken, wird ein Hybridsystem untersucht, welches aus einer vielfach resonanten linearen Silizium-Metasurface mit hoch qualitativen Kollektivresonanzen gekoppelt mit einer Molybdändisulfid-Monolage besteht. Beim Messen und Simulieren der linearen und nichtlinearen Eigenschaften zweiter Ordnung wird eine Verstärkung der Frequenzverdopplung beobachtet und Richtlinien entwickelt, wie Resonanzen für solch eine Verstärkung gestaltet werden sollten. Diesen folgend, ist es nicht nur wichtig, dass das resonant verstärkte lokale Feld mit dem nichtlinearen Material überlappt, sondern am besten an Stellen, wo die Monolage in der Luft hängt.

Die hier gefundenen Ergebnisse helfen bei der Entwicklung von kompakten, aber auch großflächigen nichtlinearen funktionalisierten Oberflächen zur Frequenzerzeugung zweiter Ordnung. Die Ergebnisse können aber auch auf nichtlineare Prozesse höherer Ordnung angewendet werden. Darüber hinaus öffnet das Verständnis über die Frequenzverdopplung in solchen Systemen Wege für den ebenso der zweiten Ordnung zugeordneten nichtlinearen Prozess der parametrischen Fluoreszenz, welcher die Emission verschränkter Photonenpaare für quantum-optische Anwendungen ermöglicht.

List of publications

Peer-reviewed journal papers

A Franz J. F. Löchner, Anna N. Fedotova, Sheng Liu, Gordon A. Keeler, Gregory M. Peake, Sina Saravi, Maxim R. Shcherbakov, Sven Burger, Andrey A. Fedyanin, Igal Brener, Thomas Pertsch, Frank Setzpfandt, and Isabelle Staude. Polarization-dependent second harmonic diffraction from resonant GaAs metasurfaces. *ACS Photonics*, 5(5):1786–1793, 2018.

B Tobias Bucher, Aleksandr Vaskin, Rajeshkumar Mupparapu, Franz J. F. Löchner, Antony George, Katie E. Chong, Stefan Fasold, Christof Neumann, Duk-Yong Choi, Falk Eilenberger, Frank Setzpfandt, Yuri S. Kivshar, Thomas Pertsch, Andrey Turchanin, and Isabelle Staude. Tailoring photoluminescence from MoS_2 monolayers by Mie-resonant metasurfaces. *ACS Photonics*, 6(4):1002–1009, 2019.

C Franz J. F. Löchner, Rajeshkumar Mupparapu, Michael Steinert, Antony George, Zian Tang, Andrey Turchanin, Thomas Pertsch, Isabelle Staude, and Frank Setzpfandt. Controlling second-harmonic diffraction by nano-patterning MoS_2 monolayers. *Optics Express*, 27(24):35475, nov 2019.

D Badrudin Jakob Stanicki, Mohammadreza Younesi, Franz J. F. Löchner, Hitesh Thakur, Wei-Kun Chang, Reinhard Geiss, Frank Setzpfandt, Yen-Hung Chen, and Thomas Pertsch. Surface domain engineering in lithium niobate. *OSA Continuum*, 3(2):345, feb 2020.

E A. V. Pakhomov, F. J. F. Löchner, L. Zschiedrich, S. Saravi, M. Hammerschmidt, S. Burger, T. Pertsch, and F. Setzpfandt. Far-field polarization signatures of surface optical nonlinearity in noncentrosymmetric semiconductors. *Scientific Reports*, 10(1):10545, jun 2020.

F Anna Fedotova, Mohammadreza Younesi, Jürgen Sautter, Aleksandr Vaskin, Franz J. F. Löchner, Michael Steinert, Reinhard Geiss, Thomas Pertsch, Isabelle Staude, and Frank Setzpfandt. Second-harmonic generation in resonant nonlinear metasurfaces based on lithium niobate. *Nano Letters*, 20(12):8608–8614, nov 2020.

G Franz J. F. Löchner, Antony George, Kirill Koshelev, Tobias Bucher, Emad Najafidehaghani, Anna Fedotova, Duk-Yong Choi, Thomas Pertsch, Isabelle Staude, Yuri Kivshar, Andrey Turchanin, and Frank Setzpfandt. Hybrid dielectric metasurfaces for enhancing second-harmonic generation in chemical vapor deposition grown MoS_2 monolayers. *ACS Photonics*, 8(1):218–227, dec 2020

Conference talks

H Franz J. F. Löchner, Stefan Fasold, Antony George, Paul D. Harrison, Christoph Menzel, Andrey Turchanin, Isabelle Staude, Falk Eilenberger, Frank Setzpfandt, and Thomas Pertsch. Second-harmonic generation in MoS_2 monolayers coupled to resonant nanoantennas. *DPG-Frühjahrstagung*, Regensburg, Germany, 2016.

I Falk Eilenberger, Franz J. F. Löchner, Stefan Fasold, Antony George, Paul D. Harrison, Tobias Bucher, Christoph Menzel, Frank Setzpfandt, Isabelle Staude, Andrey Turchanin, and Thomas Pertsch. Enhancement of light-matter interaction in MoS_2 monolayers by resonant nanoparticles. *2016 Progress in Electromagnetic Research Symposium (PIERS)*, IEEE, 2016.

J Franz J. F. Löchner, Anna Fedotova, Sheng Liu, Sina Saravi, Thomas Pertsch, Igal Brener, Frank Setzpfandt, and Isabelle Staude. Polarization dependence of second-harmonic generation in GaAs metasurfaces. *Conference on Lasers and Electro-Optics Europe & European Quantum Electronics Conference (CLEO/Europe-EQEC)*, OSA, 2017.

K Badrudin Jakob Stanicki, Reinhard Geiss, Ljiljana Djurdjevic, Franz J. F. Löchner, Wei-Kun Chang, Yen-Hung Chen, Frank Setzpfandt, and Thomas Pertsch. Surface domain engineering in bulk and thin film lithium niobate: A systematic experimental study. *Conference on Lasers and Electro-Optics Europe & European Quantum Electronics Conference (CLEO/Europe-EQEC)*, OSA, 2017.

L Rajeshkumar Mupparapu, Michael Steinert, Antony George, Franz Löchner, Zian Tang, Tobias Bucher, Frank Setzpfandt, Andrey Turchanin, Thomas Pertsch, and Isabelle Staude. Nano-patterning of MoS_2 monolayers with focused ion beam. *DPG-Frühjahrstagung*, Regensburg, Germany, 2019.

M Franz J. F. Löchner, Rajeshkumar Mupparapu, Michael Steinert, Antony George, Andrey Turchanin, Thomas Pertsch, Isabelle Staude, and Frank Setzpfandt. Second-harmonic diffraction from periodically structured MoS_2 monolayer. *In Conference on Lasers and Electro-Optics*. OSA, 2019.

N Franz J. F. Löchner, Rajeshkumar Mupparapu, Michael Steinert, Antony George, Andrey Turchanin, Thomas Pertsch, Isabelle Staude, and Frank Setzpfandt. Nanostructured MoS_2 monolayers for spatial control of second-harmonic generation. *In 2019 Conference on Lasers and Electro-Optics Europe and European Quantum Electronics Conference*, OSA, 2019.

O Heiko Knopf, Nils Lundt, Tobias Bucher, Rajeshkumar Mupparapu, Franz Löchner, Antony George, Christof Neumann, Stefan Fasold, Evgeny Sedov, Max Waldherr, Martin Klaas, Sefaating Tongay, Sebastian Klembt, Katie Chong, Duk-Yong Choi, Takashi Taniguchi, Kenji Watanabe, Ulrike Schulz, Alexey Kavokin, Sven Höfling, Andrey Turchanin, Thomas Pertsch, Christian Schneider, Frank Setzpfandt, Isabelle Staude, and Falk Eilenberger. Semiconducting 2D-Materials: nano-sandbox for fundamental physics and new platform for optical coatings, light emission and quantum light sources. *Optical Interference Coatings Conference (OIC)*, OSA, 2019.

P H. Knopf, A. Kuppadakkath, F. Rickelt, U. Schulz, N. Lundt, F. Löchner, T. Bucher, R. Mupparapu, A. George, C. Schneider, I. Staude, F. Setzpfandt, S.-Y. Lim, T. Pertsch, A. Turchanin, F. Schwierz, and F. Eilenberger. Halbleitende 2D-Materialen: Neue Werkstoffe für optische Schichten, Quantenlichtquellen und Fluoreszenzmikroskopie. *17. Thüringer Werkstofftag*, TU Ilmenau, Germany (2019)

Q Franz J. F. Löchner, Antony George, Kirill Koshelev, Tobias Bucher, Emad Najafidehaghani, Anna Fedotova, Duk Yong Choi, Thomas Pertsch, Isabelle Staude, Yuri Kivshar, Andrey Turchanin, and Frank Setzpfandt. MoS_2 monolayer coupled to a multi-resonant dielectric metasurface exhibiting enhanced second-harmonic generation. *OSA Advanced Photonics Congress*, Montreal, OSA, 2020.

Conference posters

R Franz J. F. Löchner, Rajeshkumar Mupparapu, Michael Steinert, Antony George, Zian Tang, Andrey Turchanin, Thomas Pertsch, Isabelle Staude, and Frank Setzpfandt. Second-harmonic diffraction and vortex beam from patterned MoS2 monolayer flakes. *Photonics Online Meetup*, jan 2020.

A. Appendix

Derivation of $\hat{\chi}^{(2)}$ of MoS_2 monolayer

The crystal structure of the two-dimensional MoS_2 monolayer belongs to the point group D_{3h}. Considering the material in the x, y-plane, it has a hexagonal lattice in this plane with two different atoms. The rotational symmetry is thus given by an angle of 120°. To the mirror symmetry with respect to the x, y-plane it has an additional mirror symmetry with respect to the x, z-plane, if the x-axis is in the armchair direction of the hexagonal lattice.

All three symmetries can be expressed by the following linear transformation matrices:

$$\hat{T}^{\mathrm{rot}} = \begin{pmatrix} \cos(120°) & -\sin(120°) & 0 \\ \sin(120°) & \cos(120°) & 0 \\ 0 & 0 & 1 \end{pmatrix} = \begin{pmatrix} -1/2 & -1/2\sqrt{3} & 0 \\ 1/2\sqrt{3} & -1/2 & 0 \\ 0 & 0 & 1 \end{pmatrix} , \quad \text{rotation by } 120° \tag{A.1}$$

$$\hat{T}^{\mathrm{mirXZ}} = \begin{pmatrix} 1 & 0 & 0 \\ 0 & -1 & 0 \\ 0 & 0 & 1 \end{pmatrix} , \; \hat{T}^{\mathrm{mirXY}} = \begin{pmatrix} 1 & 0 & 0 \\ 0 & 1 & 0 \\ 0 & 0 & -1 \end{pmatrix} , \text{ reflection by } x, z\text{- or } x, y\text{-plane.} \tag{A.2}$$

Following the transformation of a three dimensional tensor, we obtain for the mirror symmetry with respect to the x, z-plane:

$$\chi^{(2)'}_{rst} = \sum_{jkl} T^{\mathrm{mirXZ}}_{rj} T^{\mathrm{mirXZ}}_{sk} T^{\mathrm{mirXZ}}_{tl} \chi^{(2)}_{jkl} \, . \tag{A.3}$$

Since all components of $\hat{T}^{\mathrm{mirXZ}}$ vanish except for the diagonal ones, the equation results in $\chi^{(2)'}_{rst} = \pm\chi^{(2)}_{rst}$ with a $-$-sign when one or three times a y appears in the indices r, s, and t, otherwise there is a $+$-sign. Since a symmetry is discussed, $\hat{\chi}^{(2)'}$ ahs to be equal to $\hat{\chi}^{(2)}$. Accordingly, all components with one or three times y in the indices vanish.

Similarly, the mirror symmetry with respect to the x, y-plane can be handled, only with the result, that components with one or three times z in the indices vanish.

Only the components $\chi^{(2)}_{xxx}$, $\chi^{(2)}_{xyy}$, $\chi^{(2)}_{yxy}$, $\chi^{(2)}_{yyx}$, $\chi^{(2)}_{xzz}$, $\chi^{(2)}_{zxz}$ and $\chi^{(2)}_{zzx}$ are left. The rotation of the $\hat{\chi^{(2)}}$-tensor by 120° is described by the following equation:

$$\chi^{(2)'}_{rst} = \sum_{jkl} T^{\mathrm{rot}}_{rj} T^{\mathrm{rot}}_{sk} T^{\mathrm{rot}}_{tl} \chi^{(2)}_{jkl} \, . \tag{A.4}$$

Since the tensor $\hat{T}^{\mathrm{rot}}$ has some more components aside the diagonal, the sum gets a bit more complicated. First, the component $\chi^{(2)}_{xzz}$ is considered.

$$\chi^{(2)'}_{xzz} = -\frac{1}{2}\chi^{(2)}_{xzz} - \frac{1}{2}\sqrt{3}\chi^{(2)}_{yzz} + \chi^{(2)}_{zzz} \ . \tag{A.5}$$

Since the components $\chi^{(2)}_{yzz}$ and $\chi^{(2)}_{zzz}$ have been already shown to vanish due to the other symmetries, $\chi^{(2)'}_{xzz} = -\frac{1}{2}\chi^{(2)}_{xzz}$ which means $\chi^{(2)}_{xzz} = -\frac{1}{2}\chi^{(2)}_{xzz}$. Accordingly, the component $\chi^{(2)}_{xzz}$ and in the same way $\chi^{(2)}_{zxz}$ and $\chi^{(2)}_{zzx}$ vanish.

For the last four components, Eq. A.4 provides a system of coupled linear equations:

$$\chi^{(2)}_{xxx} = -\frac{1}{8}\chi^{(2)}_{xxx} - \frac{3}{8}(\chi^{(2)}_{xyy} + \chi^{(2)}_{yxy} + \chi^{(2)}_{yyx}) \ . \tag{A.6}$$

$$\chi^{(2)}_{xyy} = -\frac{1}{8}\chi^{(2)}_{xyy} + \frac{3}{8}(-\chi^{(2)}_{xxx} + \chi^{(2)}_{yxy} + \chi^{(2)}_{yyx}) \ . \tag{A.7}$$

$$\chi^{(2)}_{yxy} = -\frac{1}{8}\chi^{(2)}_{yxy} + \frac{3}{8}(-\chi^{(2)}_{xxx} + \chi^{(2)}_{xyy} + \chi^{(2)}_{yyx}) \ . \tag{A.8}$$

$$\chi^{(2)}_{yyx} = -\frac{1}{8}\chi^{(2)}_{yyx} + \frac{3}{8}(-\chi^{(2)}_{xxx} + \chi^{(2)}_{xyy} + \chi^{(2)}_{yxy}) \ . \tag{A.9}$$

Here, the equality of $\hat{\chi}^{(2)'}$ and $\hat{\chi}^{(2)}$ due to the symmetry is already included. The solution of the system results in $\chi^{(2)}_{xxx} - \chi^{(2)}_{xyy} = -\chi^{(2)}_{yxy} = -\chi^{(2)}_{yyx}$.

Derivation of the fundamental-harmonic polarization dependence of the overall second-harmonic intensity

The overall SH intensity $I^{\mathrm{SH}} = |E^{\mathrm{SH}}_x|^2 + |E^{\mathrm{SH}}_y|^2$ is not dependent on the FH polarization or crystal orientation rotation. For the derivation, the nonlinear polarization from Eq. 3.4 is used with the rotated crystal by angle θ and the rotating FH polarization modeled as $E_x = E_0\cos(\phi)$ and $E_y = E_0\sin(\phi)$:

$$\begin{aligned}
I^{\mathrm{SH}} &= |E^{\mathrm{SH}}_x|^2 + |E^{SH}_y|^2 \sim |P^{(2)}_x|^2 + |P^{(2)}_y|^2 \\
&\sim |\chi^{(2)}_0 \left[\cos(3\theta)\left(E_x^2 - E_y^2\right) + 2\sin(3\theta)E_xE_y\right]|^2 \\
&\quad + |\chi^{(2)}_0 \left[\sin(3\theta)\left(E_x^2 - E_y^2\right) - 2\cos(3\theta)E_xE_y\right]|^2 \\
&\sim \left[\cos(3\theta)\left(\cos^2(\phi) - \sin^2(\phi)\right) + 2\sin(3\theta)\cos(\phi)\sin(\phi)\right]^2 \\
&\quad + \left[\sin(3\theta)\left(\cos^2(\phi) - \sin^2(\phi)\right) - 2\cos(3\theta)\cos(\phi)\sin(\phi)\right]^2 \\
&\sim \left[\cos(3\theta)cos(2\phi) + sin(3\theta)\sin(2\phi)\right]^2 + \left[\sin(3\theta)\cos(2\phi) - \cos(3\theta)\sin(2\phi)\right]^2 \\
&\sim \cos^2(3\theta)cos^2(2\phi) + sin^2(3\theta)\sin^2(2\phi) + 2\cos(3\theta)\sin(3\theta)\cos(2\phi)\sin(2\phi) \\
&\quad + \sin^2(3\theta)\cos^2(2\phi) + \cos^2(3\theta)\sin^2(2\phi) - 2\sin(3\theta)\cos(3\theta)\cos(2\phi)\sin(2\phi) \\
&\sim \cos^2(3\theta)\left(\cos^2(2\phi) + \sin^2(2\phi)\right) + \sin^2(3\theta)\left(\cos^2(2\phi) + \sin^2(2\phi)\right) \\
&\sim \cos^2(3\theta) + \sin^2(3\theta) \\
&\sim 1 \ .
\end{aligned} \tag{A.10}$$

Analytical proof of the retardation compensation

For this theoretical proof, Jones formalism is used with E_{0x} and E_{0y} as the incident electric fields in x- and y-polarization, and z being the propagation direction. Then any propagation through any medium/geometry can be described via an ABCD-matrix as follows:

$$\begin{pmatrix} E_x \\ E_y \end{pmatrix} = \begin{pmatrix} A & B \\ C & D \end{pmatrix} \begin{pmatrix} E_{0x} \\ E_{0y} \end{pmatrix} \ . \tag{A.11}$$

The arbitrary phase retarder in this formalism has the following appearance:

$$\begin{pmatrix} e^{i\eta/2}\cos^2(\alpha) + e^{-i\eta/2}\sin^2(\alpha) & (e^{i\eta/2} - e^{-i\eta/2})e^{-i\phi}cos(\alpha)\sin(\alpha) \\ (e^{i\eta/2} - e^{-i\eta/2})e^{i\phi}cos(\alpha)\sin(\alpha) & e^{i\eta/2}\sin^2(\alpha) + e^{-i\eta/2}\cos^2(\alpha) \end{pmatrix} \ , \tag{A.12}$$

where η is the retardance, α is the angle to the fast axis from the x-axis, and ϕ is the circularity. $\phi = 0$ for linear retarders, $\phi = \pm\pi/2$ for circular retarders. All other values between $\pm\pi/2$ are associated with elliptical retarders.

Considering a system of two arbitrary but equal retarders with different angles of α and α' corresponding to the angle between the fast axis and the x-axis, two similar matrices are obtained, which here are called $M = \left(\begin{smallmatrix} A & B \\ C & D \end{smallmatrix}\right)$ and $M' = \left(\begin{smallmatrix} A' & B' \\ C' & D' \end{smallmatrix}\right)$.

The coupled system of both results in the final matrix $M_{\text{final}} = \left(\begin{smallmatrix} a & b \\ c & d \end{smallmatrix}\right) = \left(\begin{smallmatrix} AA'+BC' & AB'+BD' \\ CA'+DC' & CB'+DD' \end{smallmatrix}\right)$, where

$$\begin{aligned}
a &= e^{i\eta}\cos^2(\alpha)\cos^2(\alpha') + e^{-i\eta}\sin^2(\alpha)\sin^2(\alpha') + \cos^2(\alpha)\sin^2(\alpha') \\
&\quad + \sin^2(\alpha)\cos^2(\alpha') + (e^{i\eta/2} - e^{-i\eta/2})^2\cos(\alpha)\sin(\alpha)\cos(\alpha')\sin(\alpha') \\
b &= (e^{i\eta/2} - e^{-i\eta/2})e^{-i\phi}\big(\cos(\alpha')\sin(\alpha')(e^{i\eta/2}\cos^2(\alpha) + \\
&\quad + e^{-i\eta/2}\sin^2(\alpha)) + \cos(\alpha)\sin(\alpha)(e^{i\eta/2}\sin^2(\alpha') + e^{-i\eta/2}\cos^2(\alpha'))\big) \\
c &= (e^{i\eta/2} - e^{-i\eta/2})e^{i\phi}\big(\cos(\alpha)\sin(\alpha)(e^{i\eta/2}\cos^2(\alpha') + \\
&\quad + e^{-i\eta/2}\sin^2(\alpha')) + \cos(\alpha')\sin(\alpha')(e^{i\eta/2}\sin^2(\alpha) + e^{-i\eta/2}\cos^2(\alpha))\big) \\
d &= e^{i\eta}\sin^2(\alpha)\sin^2(\alpha') + e^{-i\eta}\cos^2(\alpha)\cos^2(\alpha') + \sin^2(\alpha)\cos^2(\alpha') \\
&\quad + \cos^2(\alpha)\sin^2(\alpha') + (e^{i\eta/2} - e^{-i\eta/2})^2\cos(\alpha)\sin(\alpha)\cos(\alpha')\sin(\alpha') \ .
\end{aligned} \tag{A.13}$$

To realize compensation, the matrix M_{final} has to be a unity matrix of shape $\left(\begin{smallmatrix} 1 & 0 \\ 0 & 1 \end{smallmatrix}\right)$. Accordingly, the solution for α' depending on α has to fulfill $a = 1$, $b = 0$, $c = 0$ and $d = 0$.

The easier path is realizing b and c to vanish. Since η is arbitrary, the terms with $e^{i\eta/2}$ and $e^{-i\eta/2}$ are independent to each other and cannot generally cancel out the other one. Therefore, each $e^{\pm i\eta/2}$-term has to vanish on its own.

It follows:

$$\begin{aligned}
0 &= (\cos^2(\alpha)\cos(\alpha')\sin(\alpha') + \cos(\alpha)\sin(\alpha)\sin^2(\alpha')) \\
0 &= (\sin^2(\alpha)\cos(\alpha')\sin(\alpha') + \cos(\alpha)\sin(\alpha)\cos^2(\alpha')) \\
0 &= (\cos^2(\alpha')\cos(\alpha)\sin(\alpha) + \cos(\alpha')\sin(\alpha')\sin^2(\alpha)) \\
0 &= (\sin^2(\alpha')\cos(\alpha)\sin(\alpha) + \cos(\alpha')\sin(\alpha')\cos^2(\alpha))
\end{aligned} \tag{A.14}$$

The last two equations of the set are the same as the two above and just written for completeness. Since these equations have to hold for any α, the solution can only be made by choosing α' such that $\alpha' = \alpha \pm 90°$:

$$\begin{aligned}
& 0 = (\cos^2(\alpha)\cos(\alpha')\sin(\alpha') + \cos(\alpha)\sin(\alpha)\sin^2(\alpha')) \\
\Leftrightarrow\ & 0 = (e^{i\alpha} + e^{-i\alpha})^2(e^{i\alpha'} + e^{-i\alpha'})(e^{i\alpha'} - e^{-i\alpha'}) - (e^{i\alpha} + e^{-i\alpha})(e^{i\alpha} - e^{-i\alpha})(e^{i\alpha} - e^{-i\alpha})^2 \\
\Leftrightarrow\ & 0 = -e^{i(2\alpha-2\alpha')} + e^{-i(2\alpha-2\alpha')} + e^{i2\alpha'} - e^{-i2\alpha'} + e^{i2\alpha} - e^{-i2\alpha} \\
\Leftrightarrow\ & 0 = \sin(2(\alpha-\alpha')) + \sin(2\alpha') + \sin(2\alpha) \\
\Leftrightarrow\ & 0 = \sin(\alpha'-\alpha)\cos(\alpha'-\alpha) + \sin(\alpha'+\alpha)\cos(\alpha'-\alpha) \\
\Leftrightarrow\ & 0 = \cos(\alpha'-\alpha) \ \ \textbf{or} \ \ 0 = \sin(\alpha'-\alpha) + \sin(\alpha'+\alpha) \\
\Leftrightarrow\ & \alpha'-\alpha = \pm 90° \ \ \textbf{or} \ \ (\ \alpha' = 0° \ \textbf{and} \ \alpha = \pm 90°\ )\ .
\end{aligned} \tag{A.15}$$

With the solution $\alpha' = \alpha \pm 90°$, it follows $\sin(\alpha') = \sin(\alpha \pm 90°) = \pm\cos(\alpha)$ and $\cos(\alpha') = \cos(\alpha \pm 90°) = \mp\sin(\alpha)$, which results in $\cos^2(\alpha') = \sin^2(\alpha)$, $\sin^2(\alpha') = \cos^2(\alpha)$ and $\sin(\alpha')\cos(\alpha') = -\sin(\alpha)\cos(\alpha)$.

We can conclude: $A = D'$, $D = A'$, $B - B'$, $C = -C'$, followed by $a = AD - BC = d$. So, the final matrix is $M_{\text{final}} = a \cdot \left(\begin{smallmatrix} 1 & 0 \\ 0 & 1 \end{smallmatrix}\right)$, where a follows as:

$$\begin{aligned}
a &= e^{i\eta}\cos^2(\alpha)\cos^2(\alpha') + e^{-i\eta}\sin^2(\alpha)\sin^2(\alpha') + \cos^2(\alpha)\sin^2(\alpha') \\
&\quad + \sin^2(\alpha)\cos^2(\alpha') + (e^{i\eta/2} - e^{-i\eta/2})^2\cos(\alpha)\sin(\alpha)\cos(\alpha')\sin(\alpha') \\
&= e^{i\eta}\cos^2(\alpha)\sin^2(\alpha) + e^{-i\eta}\sin^2(\alpha)\cos^2(\alpha) + \cos^2(\alpha)\cos^2(\alpha) \\
&\quad + \sin^2(\alpha)\sin^2(\alpha) - (e^{i\eta/2} - e^{-i\eta/2})^2\cos(\alpha)\sin(\alpha)\cos(\alpha)\sin(\alpha) \\
&= (e^{i\eta} + e^{-i\eta})\sin^2(\alpha)\cos^2(\alpha) + \cos^4(\alpha) + \sin^4(\alpha) - (e^{i\eta/2} - e^{-i\eta/2})^2\cos^2(\alpha)\sin^2(\alpha) \\
&= (e^{i\eta} + e^{-i\eta} - (e^{i\eta/2} - e^{-i\eta/2})^2)\sin^2(\alpha)\cos^2(\alpha) + \cos^4(\alpha) + \sin^4(\alpha) \\
&= (e^{i\eta} + e^{-i\eta} - (e^{i\eta} + e^{-i\eta} - 2))\sin^2(\alpha)\cos^2(\alpha) + \cos^4(\alpha) + \sin^4(\alpha) \\
&= 2\sin^2(\alpha)\cos^2(\alpha) + \cos^4(\alpha) + \sin^4(\alpha) \\
&= (\sin^2(\alpha) + \cos^2(\alpha))^2 = 1\ .
\end{aligned} \tag{A.16}$$

Analytical error calculation introduced by beam splitter in the retardation compensation

The solution for the retardation compensation considers the transmission through the beam splitter, which the SH light has to transmit in the setup arrangement, as perfect. Unfortunately, even non-polarizing beam splitters have slightly different transmission coefficients for the two orthogonal linear polarization states TE and TM. In the following derivation, the transmission of the beam splitter in x is considered to be 1 and in y 1-ϵ. Considering a system of two arbitrary but equal retarders with different angles of α and α' corresponding to the angle between the fast axis and the x-axis as in subsection 4.2.1, two similar matrices are obtained, which are called $M = \left(\begin{smallmatrix} A & B \\ C & D \end{smallmatrix}\right)$ and $M' = \left(\begin{smallmatrix} A' & B' \\ C' & D' \end{smallmatrix}\right)$. Additionally, the BS has to be included with its matrix $M_{\mathrm{BS}} = \left(\begin{smallmatrix} 1 & 0 \\ 0 & 1-\epsilon \end{smallmatrix}\right)$.
The coupled system of retarder 1, then beam splitter and retarder 2 results in the final matrix $M_{\mathrm{final}} = \left(\begin{smallmatrix} a & b \\ c & d \end{smallmatrix}\right) = \left(\begin{smallmatrix} AA'+(1-\epsilon)BC' & AB'+(1-\epsilon)BD' \\ CA'+(1-\epsilon)DC' & CB'+(1-\epsilon)DD' \end{smallmatrix}\right)$, where

$$
\begin{aligned}
a &= e^{i\eta}\cos^2(\alpha)\cos^2(\alpha') + e^{-i\eta}\sin^2(\alpha)\sin^2(\alpha') + \cos^2(\alpha)\sin^2(\alpha') + \sin^2(\alpha)\cos^2(\alpha') \\
&\quad + (1-\epsilon)\ (e^{i\eta/2} - e^{-i\eta/2})^2\cos(\alpha)\sin(\alpha)\cos(\alpha')\sin(\alpha') \\
b &= (e^{i\eta/2} - e^{-i\eta/2})e^{-i\phi}\Big(\cos(\alpha')\sin(\alpha')(e^{i\eta/2}\cos^2(\alpha) + e^{-i\eta/2}\sin^2(\alpha)) \\
&\quad + \cos(\alpha)\sin(\alpha)\ (1-\epsilon)\ (e^{i\eta/2}\sin^2(\alpha') + e^{-i\eta/2}\cos^2(\alpha'))\Big) \\
c &= (e^{i\eta/2} - e^{-i\eta/2})e^{i\phi}\Big(\cos(\alpha)\sin(\alpha)(e^{i\eta/2}\cos^2(\alpha') + e^{-i\eta/2}\sin^2(\alpha')) \\
&\quad + \cos(\alpha')\sin(\alpha')\ (1-\epsilon)\ (e^{i\eta/2}\sin^2(\alpha) + e^{-i\eta/2}\cos^2(\alpha))\Big) \\
d &= (1-\epsilon)\ \Big(\sin^2(\alpha)(e^{i\eta}\sin^2(\alpha') + \cos^2(\alpha')) + \cos^2(\alpha)(e^{-i\eta}\cos^2(\alpha') + \sin^2(\alpha'))\Big) \\
&\quad + (e^{i\eta/2} - e^{-i\eta/2})^2\cos(\alpha)\sin(\alpha)\cos(\alpha')\sin(\alpha')\ .
\end{aligned}
\tag{A.17}
$$

With the solution from subsection 4.2.1 $\alpha' = \alpha \pm 90°$, the transmission values a and d result in

$$
\begin{aligned}
a &= 1 + \epsilon\ (e^{i\eta/2} - e^{-i\eta/2})^2\cos^2(\alpha)\sin^2(\alpha) \\
&= 1 - \epsilon\ 4\sin^2(\eta/2)\sin^2(\alpha)\cos^2(\alpha) = 1 - \epsilon\ \sin^2(\eta/2)\sin^2(2\alpha) \\
d &= 1 - \epsilon\Big(\left[e^{i\eta} + e^{-i\eta}\right]\sin^2\alpha\cos^2(\alpha) + \sin^4(\alpha) + \cos^4(\alpha)\Big) \\
&= 1 - \epsilon\Big(2\cos(\eta)\sin^2\alpha\cos^2(\alpha) + \sin^4(\alpha) + \cos^4(\alpha)\Big) \\
&= 1 - \epsilon\Big(2(1 - 2\sin^2(\eta/2))\sin^2\alpha\cos^2(\alpha) + \sin^4(\alpha) + \cos^4(\alpha)\Big) \\
&= 1 - \epsilon\Big(1 - 4\sin^2(\eta/2)sin^2(\alpha)\cos^2(\alpha)\Big) \\
&= 1 - \epsilon\Big(1 - \sin^2(\eta/2)\sin^2(2\alpha)\Big)\ .
\end{aligned}
\tag{A.18}
$$

These results show that the original transmission of the beam splitter of 1 and 1-ϵ is slightly changed depending on the retardance η and the angle α, but just by maximally the value of ϵ.

The additional terms for the off-diagonal elements b and c are non-vanishing:

$$\begin{aligned} b &= -\epsilon \ (e^{i\eta/2} - e^{-i\eta/2}) \cos(\alpha) \sin(\alpha) (e^{i\eta/2} \sin^2(\alpha') + e^{-i\eta/2} \cos^2(\alpha')) \\ &= -\epsilon \ \Big(\big[e^{i\eta} - 1\big] \cos^3(\alpha) \sin(\alpha) + \big[1 - e^{-i\eta}\big] \sin^3(\alpha) \cos(\alpha) \Big) \quad \text{and} \\ c &= -\epsilon \ (e^{i\eta/2} - e^{-i\eta/2}) \cos(\alpha') \sin(\alpha') (e^{i\eta/2} \sin^2(\alpha) + e^{-i\eta/2} \cos^2(\alpha)) \\ &= -\epsilon \ \Big(\big[e^{i\eta} - 1\big] \sin^3(\alpha) \cos(\alpha) + \big[1 - e^{-i\eta}\big] \cos^3(\alpha) \sin(\alpha) \Big) \quad . \end{aligned} \tag{A.19}$$

Both values b and c are complex and have an absolute value in the order of ϵ.

B. List of abbreviations

2D	two-dimensional
AFM	atomic force microscope
AlGaAs	aluminum gallium arsenide
AlGaO	aluminum gallium oxide
BFP	back-focal plane
BS	beam splitter
CCD	charge coupled device
CVD	chemical vapor deposition
CW	continuous wave
DFG	difference frequency generation
ED	electric dipole
EMCCD	electron-multiplying charge coupled device
FH	fundamental harmonic
FEM	finite element method
FIB	focused ion beam
FWHM	full width at half maximum
Ga	gallium
GaAs	gallium arsenide
HWP	half-wave plate
ICP	inductively coupled plasma
KOH	potassium hydroxide
$LiNbO_3$	lithium niobate
MD	magnetic dipole
MoO_3	molybdenum trioxide
MoS_2	molybdenum disulfide
$MoSe_2$	molybdenum diselenide
NA	numerical aperture
Nd:YAG	neodymium-doped yttrium aluminum garnet
PDMS	polydimethylsiloxane
PL	photoluminescence
PMMA	poly(methyl methacrylate)
Q-factor	quality factor
QGM	quasi-guided mode
S_2	sulfur
SEM	scanning electron microscope
SFG	sum frequency generation
SH	second harmonic
SHG	second-harmonic generation
Si	silicon
SLR	surface lattice resonance
SM	symmetry forbidden
SPDC	spontaneous parametric down-conversion
TE	transverse electric
THG	third-harmonic generation
TM	transverse magnetic
TMD	transition metal dichalcogenide
WS_2	tungsten disulfide
WSe_2	tungsten diselenide

C. Curriculum Vitae

Only available in the reviewer's version.

D. Acknowledgement

Over the years of research, and even before, many people contributed, whether scientifically or otherwise. With these lines I want to say thank you to everybody who helped me in any way, even if not specifically mentioned, to accomplish this work.

First of all, I want to thank Prof. Dr. Thomas Pertsch for giving me the opportunity to work in his research group and in his laboratories, where he established a very friendly working atmosphere I particularly love to work in. His intelligence, knowledge and experience can lift any work to higher spheres.

Enormous gratitude have to be expressed to Dr. Frank Setzpfandt. He spent his time for me, from the beginning until the end, supervising me from the overall strategy toward the daily struggle details.

Additionally, I want to thank Prof. Dr. Isabelle Staude for her supervision giving me the opportunity to deal with the dielectric metasurfaces and the 2D materials. Here, especially the collaboration with Prof. Dr. Andrey Turchanin and his Post-Doc Dr. Antony George have to be mentioned. They provided the 2D materials in great quality and short time, and they always offered meaningful discussions.

Moreover, fruitful collaborations with Dr. Igal Brener and his group as well as with Prof. Dr. Yuri Kivshar have to be acknowledged.

Many thanks for a great working atmosphere, for helpful discussions and for many great hours have to be expressed toward the Nano & Quantum Optics group. Highlighting some, but not degrading others, I want to mention some colleagues in particular.

Thanks Anna, for being my first student and later co-working doctoral candidate. I always enjoyed helping as well as I appreciate receiving help.

Thanks Najmeh for the happy smiles during dark and bright hours. Thanks Jan and Thomas for the shared San José experience. Thanks Tobias for being in the same two-dimensional boat and helping me to survive the cruise. Thanks Sina for many insights into the *Fundamentals of Modern Optics*. And thanks to Falk for the general happiness, creativity, optimism and faith in the joy of science.

Many thanks to Julia and Daniel for always being there and solving any administrative or technical problem, but particularly for including me into the weekly breakfast round and keeping it alive over the years.

Big thanks go to the DoKDoK organizers over the years, for making such an effort. It is again Jan, who I have to thank for forcing me into this, and then Andreas for the shared activities.

I came to Jena by joining the IRTG 2101 to work on my thesis. With regards to content, I felt rather outcast since everybody worked on waveguides while I worked on nanostructures and 2D materials. However, I want to thank the GRK and all its preparing and conducting people. In particular the coordinators, Dorit Schmidt for accompanying us into this collaboration, to Canada and later in a different role; and of course Anna Späthe for taking over the job and pulling every string to help us and the professors in keeping this thing alive.

In the end, the biggest achievement of the GRK in my eyes was the friendly and respectful community of its members. In particular, some members of the first generation developed to some kind of core of the GRK became my most important friends here in Jena during the PhD time and now all around Germany. Thanks Christoph, Max and Georg and your partners Nina, Fine and Brenda for all the great times!

Finally, I want to thank my family, in particular my parents and grand-parents for taking so good care of me and their other loved ones, so that I always found a warm and secure place when needed and enough appreciation for knowledge, thoughts and discussions, which might have led me to engage in the world of science.

My beloved sister! I thank her endlessly for being always a step further, but never looking down on me, rather nurturing me with her experience, her solutions against obstacles and her warm heart.

I want to thank my parents in law for taking me in as a son, teaching me the real life beyond the academic and elite bubble, giving me the possibility to decelerate and find happiness in the most peculiar place women and men created for their stomach and their soul – the garden.

Susi, my love, you give my life a happiness I cannot express, a loveliness I cannot repay and a warmth no physics could ever measure. Thank you for sticking to me throughout this process. Thank you for bringing our little girl into this life and filling it with the same warmth, love and happiness you share with me. Your and her smile helped me through many difficult phases.

E. Ehrenwörtliche Erklärung

Ich erkläre hiermit ehrenwörtlich, dass ich die vorliegende Arbeit selbständig, ohne unzulässige Hilfe Dritter und ohne Benutzung anderer als der angegebenen Hilfsmittel und Literatur angefertigt habe. Die aus anderen Quellen direkt oder indirekt übernommenen Daten und Konzepte sind unter Angabe der Quelle gekennzeichnet.

Bei der Auswahl und Auswertung folgenden Materials haben mir die nachstehend aufgeführten Personen in der jeweils beschriebenen Weise unentgeltlich geholfen:

1. Die untersuchte GaAs-Probe wurde durch die Forschungsgruppe um Igal Brener, Sandia National Laboratories, Albuqueque, New Mexico, USA, insbesondere durch die Arbeit von Sheng Liu hergestellt.
2. Experimentelle Untersuchungen an der GaAs-Probe wurden unter meiner Anleitung von Anna Fedotova durchgeführt.
3. Die CVD-Wachstumsprozedur der MoS_2-Monolagen wurde durch die Arbeitsgruppe um Prof. Andrey Turchanin vom Institut für Physikalische Chemie der Friedrich-Schiller-Universität Jena, insbesondere durch Anleitung von Antony George durchgeführt. Der Transfer der Monolagen auf Substrate und Strukturen wurde ebenfalls durch diese Gruppe realisiert, unter Mithilfe von Tobias Bucher aus der Forschungsgruppe Nano & Quantum Optics vom Institut für Angewandte Physik der Friedrich-Schiller-Universität Jena.
4. Die Prozesse des FIB-Fräsens an MoS_2-Monolagen und deren Charakterisierung durch Rasterkraftmikroskopie (AFM - atomic force microscopy) wurde durch Michael Steinert unter Mithilfe von Rajesh Mupparapu, beide Arbeitsgruppe Nano & Quantum Optics am Institut für Angewandte Physik der Friedrich-Schiller-Universität Jena, durchgeführt.
5. Das Design der Siliziumstrukturen für das Hybridsystem wurde durch Kirill Koshelev, sowohl dem Department of Physics and Engineering, ITMO University, St. Petersburg, Russland, als auch dem Nonlinear Physics Centre der Australian National University, Canberra, Australien, zugehörig, entworfen.
6. Die Siliziumstrukturen für das Hybridsystem wurden von Duk-Yong Choi, vom Laser Physics Centre an der Australian National University, Canberra, Australiien, gefertigt.
7. Die Transmissionmessungen an den Siliziumstrukturen des Hybridsystems wurden durch Tobias Bucher durchgeführt.
8. Sven Burger, Mitarbeiter der Firma JCMwave sowie dem Zuse-Institut Berlin zugehörig, half bei der Benutzung des FEM solvers eben dieser Firma JCMwave.

Weitere Personen waren an der inhaltlich-materiellen Erstellung der vorliegenden Arbeit nicht beteiligt. Insbesondere habe ich hierfür nicht die entgeltliche Hilfe von Vermittlungs- bzw. Beratungsdiensten (Promotionsberater oder andere Personen) in Anspruch genommen. Niemand hat von mir unmittelbar oder mittelbar geldwerte Leistungen für Arbeiten erhalten, die im Zusammenhang mit dem Inhalt der vorgelegten Dissertation stehen.

Die Arbeit wurde bisher weder im In- noch im Ausland in gleicher oder ähnlicher Form einer anderen Prüfungsbehörde vorgelegt.

Die geltende Promotionsordnung der Physikalisch-Astronomischen Fakultät ist mir bekannt.

Ich versichere ehrenwörtlich, dass ich nach bestem Wissen die reine Wahrheit gesagt und nichts verschwiegen habe.

Jena, den 3. Februar 2021

Unterschrift d. Verfassers